Plasmon-enhanced Raman Scattering of Carbon Nanosystems

Im Fachbereich Physik der
Freien Universität Berlin
eingereichte

Dissertation
zur Erlangung des Grades eines Dr. rer. nat.

von

Sören Tobias Waßerroth

Berlin, im August 2019

1. Gutachter: Prof. Dr. Stephanie Reich
2. Gutachter: Prof. Dr. Martin Wolf

Tag der Einreichung: 06. August 2019
Tag der Disputation: 21. Oktober 2019

Selbstständigkeitserklärung

Hiermit versichere ich, dass ich alle verwendeten Hilfsmittel und Hilfen angegeben und die vorliegende Arbeit auf dieser Grundlage selbstständig verfasst habe. Diese Arbeit ist nicht schon einmal in einem früheren Promotionsverfahren eingereicht worden.

Sören Wasserroth

Kurzfassung

Oberflächenverstärkte Ramanstreuung ist eine leistungsfähige Methode, um Ramanintensitäten um mehrere Größenordnungen zu verstärken. Das plasmonische Nahfeld von metallischen Nanopartikeln oder rauen Metaloberflächen verstärkt sowohl das eingehende als auch das gestreute Licht des Ramanprozesses.

Zuerst beschreibe ich die Interaktion zwischen Graphen und einem Gold Nanodimer. Graphen hat keine intrinsische Resonanz und ist daher eine exzellente Probe, um die plasmonischen Eigenschaften von Dimeren mit Ramanstreuung zu untersuchen. Mithilfe von wellenlängenabhängigen Ramanmessungen habe ich die plasmonische Nahfeldresonanz des Dimers bestimmt und mit Dunkelfeldspektroskopie verglichen.

In dem zweiten Teil nutze ich Kohlenstoffnanoröhren (CNTs) als Ramanprobe, die eine intrinsische Resonanz besitzen. Ich habe die (7,5) Chiralität genutzt, da ihre intrinsische Resonanz mit der Plasmonresonanz des Dimers übereinstimmt. Polarisationsabhängige Ramanmessungen zeigten ein Maximum entlang der CNT und ein zweites entlang der Dimerachse. Wellenlängenabhängige Ramanmessungen ergaben eine schmalere Resonanz, wenn die CNT plasmonisch verstärkt wird im Vergleich zu einer Referenzmessung.

Der dritte Teil untersucht den Einfluss des plasmonischen Nahfelds an Sexithiophenmolekülen eingeschlossen in Kohlenstoffnanoröhren. In der oberflächenverstärkten Ramanstreuung hat der Einschluss von Molekülen die Auswirkung, dass keine chemische Verstärkung auftritt. Ich untersuchte die eingeschlossenen Moleküle innerhalb des Golddimers und eine Referenz ohne plasmonische Verstärkung. Ich bestimmte die intrinsische Resonanz der Referenzprobe und den Einfluss des Plasmons auf die Moleküle im Dimer. Maximale Verstärkung ergab sich zwischen intrinsischer und plasmonischer Resonanz.

Im letzten Teil zeige ich ein Anwendungsbeispiel für oberflächenverstärkte Ramanstreuung. Ich benutze ein kommerziell verfügbares SERS Substrat, um Ramanstreuexperimente mit einer LED als Anregungsquelle durchzuführen. Vier verschiedene Ramanproben konnten zweifelsfrei unterschieden werden. Die Verwendung eines SERS Substrats mit LED Anregung öffnet neue Möglichkeiten für tragbare Ramangeräte.

Abstract

Surface-enhanced Raman scattering (SERS) is a powerful technique to enhance the Raman intensity by several orders of magnitude. In SERS, the plasmonic near field of metal nanoparticles or rough metal surfaces enhances the incoming and scattered light of the Raman process.

The first presented experimental results investigate the interaction of graphene suspended over gold nanodimers. Graphene has a constant Raman cross section in the visible spectrum and is therefore an excellent candidate to investigate the plasmonic resonance of gold dimers by Raman scattering. With wavelength-dependent Raman spectroscopy I was able to determine the plasmonic near-field resonance and compare it with the far-field resonance measured by dark-field measurements.

In the second part I changed the Raman reporter to a resonant system, carbon nanotubes. I chose chirality enriched (7,5) nanotubes because their intrinsic resonance matches the resonance of the localized surface plasmon of the dimer. Polarization-dependent Raman measurements showed two maxima, one along the nanotube axis, and one along the dimer axis. Wavelength-dependent Raman measurements showed a narrower resonance if the nanotubes were plasmonically enhanced.

The third part presents SERS measurements on sexithiophene molecules encapsulated in a CNT. The encapsulation has the major advantage that the molecules are protected from the environment. For SERS that means that no chemical enhancement is expected. I investigated the encapsulated molecules inside of a gold nanodimer gap and a reference without plasmonic enhancement. I was able to determine the intrinsic resonance of the encapsulated molecules and investigate the influence of the plasmonic near field.

The last part gives an example for an application of SERS. I used a commercially available SERS substrate to perform Raman scattering experiments with an LED as excitation source. It was possible to unambiguously distinguish four different Raman reporters. The application of SERS substrates with LED excitation opens new possibilities for handheld Raman devices.

Contents

1 | Introduction

Inelastic light scattering was first observed in 1928 by C. Raman.[1] It has become a fundamental technique to study vibrations of crystals and molecules. However Raman scattering has the major disadvantage that its scattering cross section is very weak.[2] Special techniques are available to enhance the Raman intensity like resonant Raman scattering or surface enhanced Raman scattering (SERS).[3–6] While resonant Raman scattering exploits intrinsic properties of the investigated material, SERS requires an external plasmonic near field to enhance the Raman scattering process. In most SERS experiments a combination of both enhancement mechanisms will be present since most Raman reporters investigated by SERS exhibit intrinsic resonances.[6]

Resonant Raman scattering uses electronic and optical transitions in the investigated material. If the exciting or scattered light matches the electronic transition energy, Raman enhancement occurs which is on the order of 10^4.[4] This method is sensible to single groups of the analyte.

SERS in contrast requires external near fields to enhance the Raman process. Typical SERS substrates are rough metal surfaces or ensembles of metal nanoparticles.[6–10] SERS enhancement factors of up to 10^{10} were reported, achieving even single molecule detection.[11–14] SERS is a widely used technique with many applications in various fields like forensics, biosensing, and analytics.[15;16] Although SERS was discovered in the 1970s there is still a debate in the community about the underlying mechanism.[6–8;17] Different theories are proposed to explain the fundamentals. The most common approach is the electromagnetic mechanism.[18–20] It describes the plasmonic near field as an external influence that enhances the incoming and scattered light. To explain discrepancies between theory and experiments, an additional enhancement factor attributed to the interaction between the metal and the analyte is often considered, called chemical enhancement. Another approach is to incorporate the interaction between the plasmon and the Raman process in the microscopic picture of Raman scattering in a quantum mechanical way. The so-called higher-order Raman scattering theory includes the plasmon as a perturbation

in the scattering process.[21] Furthermore SERS was described in an optomechanical approach which uses the framework of cavity optomechanics describing the coupling between molecular vibrations and the plasmon.[22]

Different techniques are available to study plasmonic resonances. The plasmonic near field can be visualized by scanning near field microscopy or electron energy loss spectroscopy.[23–26] With dark-field scattering it is possible to measure the plasmonic resonance in the far field whereas wavelength-dependent Raman measurements enable a direct measurement of the resonance in the near field.

To study the fundamental scattering mechanism of SERS it is most intuitive to use a model system that has simple properties. Often dimers are used because of their geometry and well defined plasmonic hotspot. The near field of a dimer can easily be simulated. They can be reliably produced by electron beam lithography. To disentangle the influence of intrinsic and plasmonic resonance it is reasonable to use a Raman reporter without intrinsic resonance. The two dimensional semimetal graphene is an excellent candidate to study the plasmonic enhancement of a gold dimer.[27–29] The graphene gets pulled in the plasmonic hotspot due to adhesion forces. The induced strain is a good indicator that plasmonic enhancement is present. Graphene suspended on a gold dimer was studied by single-wavelength Raman measurements and plasmonic enhancement was confirmed.

Most reporters investigated by SERS are molecules that inhibit an intrinsic resonance. To get insight in the interplay of the plasmonic resonance with an intrinsic resonance of the analyte a different Raman reporter than graphene is required. The one dimensional allotrope of carbon nanomaterials, carbon nanotubes (CNTs) have an intrinsic resonance that is determined by the chirality.[30] Therefore it is possible to tune its resonance compared to the plasmonic resonance by choosing a specific chirality. By dielectrophoretic deposition it is possible to precisely place carbon nanotubes in a plasmonic hotspot.[31] The strong anisotropy of CNTs make them good candidates to investigate the interplay of the resonances.

Additionally to the plasmonic near-field enhancement, chemical enhancement might yield a secondary enhancement factor that is usually hard to gauge in SERS experiments since only the total enhancement is measured. In special cases it is possible to exclude the chemical enhancement. For example for molecules encapsulated in CNTs it was shown that they are protected from the chemical environment that excludes chemical enhancement as well in the context of SERS.[32] Therefore nanotubes are a good carrier for molecules to study only the near-field enhancement.

The first part of the thesis introduces the theoretical background of localized surface plasmons, Raman scattering, and carbon nanomaterials necessary to understand the

thesis. In Chapter 2 I give an introduction to plasmonics, especially to localized surface plasmons (LSPs). Plasmons describe the collective oscillation of electrons in metals excited by light. In LSPs the plasmon is confined to a small metal nanoparticle which enables a direct excitation by light.[33] Around the metal nanoparticle a strongly localized electromagnetic near field is created. I derive the LSP resonance within the electrostatic approximation for a spherical particle. Parameters like size, shape, and material of the metal particle tune the resonance over a broad spectral range.[34;35] Arrangements of nanoparticles, like dimers, can confine the plasmonic near field to so-called hot spots. In dimer hotspots the near fields of two nanoparticles couple via their dipoles and create a strong electromagnetic field in the interparticle gap depending on the gap size.[36] I will use dimers consisting of two gold discs or half spheroids for the SERS experiments.

In the third chapter I present the fundamentals of Raman scattering. First, I will introduce the macroscopic and microscopic picture of Raman scattering explaining the basic scattering mechanism. The concept of resonant Raman scattering resulting in incoming and outgoing resonances will be explained. In the last part of the chapter I focus on SERS. In the SERS community different approaches are considered to explain the enhancement mechanism. I introduce the electromagnetic (EM) enhancement mechanism and the higher-order Raman scattering (HORa) theory. The EM enhancement describes the plasmonic near field as an external effect enhancing the incoming and scattered light of the Raman process.[18–20] The HORa theory, in contrast, incorporates the interaction of the incoming and scattered light in the microscopic picture of the Raman scattering process.[21] Therefore it is a quantum mechanical treatment of SERS. In the end I comment on chemical enhancement that describes the chemical interaction of the metal with the Raman reporter and can lead to enhancement as well.[9]

Chapter 4 introduces the fundamental properties of carbon nanomaterials, namely graphene and carbon nanotubes (CNTs). These are used in this thesis as Raman reporters in the SERS experiments. I present the structure and the phonon dispersion of graphene. Then I focus on the Raman spectrum of graphene and the properties of the Raman modes depending on polarization, excitation wavelength, strain, and doping. Graphene is particularly interesting for SERS experiments because of its constant Raman cross section and polarization independent Raman modes.[37] In contrast to graphene, CNTs have intrinsic resonances that depend on their chirality.[30] In the second part of the chapter I discuss how to derive the chirality of a CNT and introduce the basic properties of CNTs. Again, emphasis is put on the discussion of the Raman spectrum of CNTs.

Chapter 5 is dedicated to the different Raman and dark-field experimental setups used to investigate the different samples. The experimental techniques to produce the samples

are shortly introduced as well. After this fundamental introduction to the methods and materials I will show and discuss the experimental results.

In Chapt. 6 I present the first results of the thesis on graphene suspended on top of gold nanodimer consisting of two gold discs. From Raman measurements and atomic force microscopy it is visible that the graphene is pulled into the interparticle gap of the dimer. The plasmonic hotspot is located in the gap and strong Raman enhancement was observed. With wavelength-dependent Raman measurements the plasmon resonance was determined. The strong localization of the hotspot was confirmed by Raman profiles in x-, y-, and z-direction. Polarization-dependent measurements showed the strong influence of the plasmonic near field on the Raman modes of graphene as well. Since graphene has a constant Raman cross section in the investigated wavelength range all changes in Raman intensity were appointed to the interaction with the plasmon. While the wavelength-dependent Raman measurements directly probe the near field of the dimer, I compare the plasmon resonance to the far-field response measured by dark-field scattering. A difference between the near- and far-field response is observed. Then I discuss wavelength-dependent Raman profiles of different dimers that show sharp plasmonic resonances. In the end of the chapter I show indications of plasmon activated defect modes in graphene.

Graphene is an excellent material to determine the plasmon resonance and compare different SERS substrates because of its constant Raman cross section however most Raman reporters investigated by SERS are materials with intrinsic resonances. It is therefore important to investigate the interplay of the plasmonic resonance with intrinsic resonances. As a first example I discuss single chirality CNTs in a gold dimer gap of two half spheroids in Chapt. 7. The (7,5) chirality was chosen because its resonance corresponds to the plasmon resonance of the gold dimer. Dielectrophoretic deposition enables a precise placement of nanotubes in the plasmonic hotspot. Polarization-dependent Raman measurements show two separated maxima in the direction of the nanotube and the plasmonic near field. The latter is oriented perpendicular to the nanotube axis were no Raman intensity is observed for single walled CNTs. Wavelength-dependent Raman measurements on the CNTs show a narrowing of the resonance when plasmonically enhanced.

The investigated (7,5) nanotubes are a good example of a resonant Raman reporter matching the resonance of the plasmon. As a third system, I investigate α-sexithiophene molecules encapsulated in CNTs (α-6T@CNT). The encapsulation of molecules provides the major advantage that the molecules are protected from the chemical environment.[32;38] In SERS that means that they are not exposed to chemical enhancement. Encapsulated

α-6T molecules form a head-to-tail structure in CNTs following the CNT axis therefore the orientation of the molecules in the plasmonic hotspot is accessible by characterization methods like AFM or SEM.[39;40] In Chapter **??**, I compare two bundles of α-6T@CNT: A reference without any plasmonic enhancement and a plasmonically enhanced bundle deposited in a gold dimer similar to the previously investigated ones of the (7,5) CNTs. I performed wavelength-dependent measurements to find the intrinsic resonance of the reference α-6T@CNT by resonant Raman scattering. On the plasmonically enhanced encapsulated α-6T the interplay of the intrinsic with the plasmonic resonance is investigated. When discussing SERS enhancement it is very important to compare the enhanced Raman reporter with a reference in the same chemical environment. Molecular and nanoparticle resonances are very susceptible to changes in the environment.

In the last part of the thesis (Chapt. 9) I show an application of the large enhancement factors of SERS. I use an LED as excitation source for the Raman setup. With sophisticated systems it was shown that LED excitation is in general applicable for Raman scattering.[41;42] LED excitation in combination with a commercial available SERS substrate are used in a very simple setup only consisting of a microscope and a spectrometer. I compare the LED excitation with laser excitation at the same wavelength. Four different Raman reporters (DTNB, R6G, p-NTP, and CNTs) could be unambiguously identified. The combination of LED excitation and SERS substrate offers a promising route for low-budget handheld Raman devices.

2 | Localized surface plasmons

Surface plasmons describe the excitation of electron oscillations at an interface of two materials with different dielectric functions. There are two different kinds of surface plasmons: surface plasmon polaritons that can propagate at the surface interface and localized surface plasmons (LSPs). LSPs describe the excitation of non-propagating electrons in a metallic nano particle coupled to an electric field. In this chapter I will derive the plasmonic near field of a gold nanosphere in the electrostatic approximation. I will introduce the Fröhlich condition which describes the plasmon resonance. In the end I will discuss the influence of the coupling of two particles on the plasmonic near field.

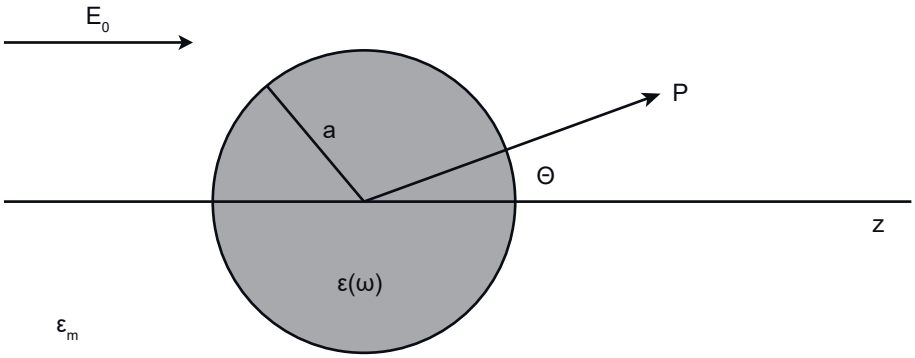

Figure 2.1 Sketch of a sphere with radius a and dielectric function $\varepsilon(\omega)$ in a medium with dielectric function ε_m exposed to an electrostatic field $\mathbf{E}$ aligned to the z-axis. The electric field and potential will be evaluated at point P with position $\mathbf{r}$ under the angle Θ. Figure adapted from Ref. [33].

To describe the LSP in the electrostatic approximation I make the following assumptions. A metallic particle with dielectric function $\varepsilon(\omega)$ (in the Drude model[43]) will be placed in an uniform electric field $\mathbf{E} = E_0\hat{z}$. The size of the particle is much smaller than the wavelength of light, to be more precise, smaller than 100 nm, thus the electric field of the incoming light wave is considered constant over the entire particle. To simplify the

calculations, the particle is assumed to be spherical with radius a and placed at the origin of the coordinate system. Figure 2.1 depicts a sketch of this setup.

To understand the response of the LSP it is necessary to solve the Laplace equation for the electrostatic potential $\nabla^2\Phi = 0$. The electric field is given by $\mathbf{E} = -\nabla\Phi$. Considering the azimuthal symmetry of this problem, the general solution is of the form:[44]

$$\Phi(r,\Theta) = \sum_{l=0}^{\infty}[A_l r^l + B_l r^{l+1}]P_l(\cos\Theta), \tag{2.1}$$

where $P_l(\cos\Theta)$ are the Legendre polynomials of order l. The coefficients A_l and B_l can be determined from the boundary conditions at $r = a$ and $r \to \infty$. Evaluating the conditions lead to:[44]

$$\Phi_{Out} = -E_0 r\cos\Theta + \frac{\varepsilon(\omega) - \varepsilon_m}{\varepsilon(\omega) + 2\varepsilon_m} E_0 a^3 \frac{\cos\Theta}{r^2}, \tag{2.2}$$

where the potential can be interpreted as a superposition of the applied field and a dipole field originating at the center of the sphere. The dipole field $\mathbf{p}$ is given as:

$$\mathbf{p} = 4\pi\varepsilon_0\varepsilon_m a^3 \frac{\varepsilon(\omega) - \varepsilon_m}{\varepsilon(\omega) + 2\varepsilon_m}\mathbf{E}_0. \tag{2.3}$$

The potential can be rewritten as:

$$\Phi_{Out} = -E_0 r\cos\Theta + \frac{\mathbf{p}\cdot\mathbf{r}}{4\pi\varepsilon_0\varepsilon_m r^3}. \tag{2.4}$$

Following the electrostatic approach for a subwavelength particle, the potential consists of the applied field and a dipole field. The polarizability α is introduced as part of the dipole field $\mathbf{p} = \varepsilon_0\varepsilon_m\alpha\mathbf{E}_0$:

$$\alpha = 4\pi a^3 \frac{\varepsilon(\omega) - \varepsilon_m}{\varepsilon(\omega + 2\varepsilon_m}. \tag{2.5}$$

Evaluating the electric field of a LSP outside of the particle $\mathbf{E}_{Out} = -\nabla\Phi_{Out}$ gives:

$$\mathbf{E}_{Out} = \mathbf{E}_0 + \frac{3\mathbf{n}(\mathbf{n}\cdot\mathbf{p}) - \mathbf{p}}{4\pi\varepsilon_0\varepsilon_m r^3}. \tag{2.6}$$

Evaluating the frequency dependence of the dielectric function $\varepsilon(\omega)$ leads to a resonance condition for the LSP [see Eq. (2.5)], called Fröhlich condition. A resonance develops at:

$$\mathrm{Re}[\varepsilon(\omega)] = -2\varepsilon_m \tag{2.7}$$

The dielectric function $\varepsilon(\omega)$ is described in the Drude model as:

$$\varepsilon(\omega) = 1 - \frac{\omega_p^2}{\omega^2 + \mathrm{i}\gamma\omega}, \tag{2.8}$$

where ω_p is the plasma frequency and γ the collision frequency.

In Fig. 2.2 the absolute value of the polarizability of a gold particle is plotted over the energy; a resonance occurs around 2.5 eV. The polarizability remains finite, because of the complex character of the dielectric function.

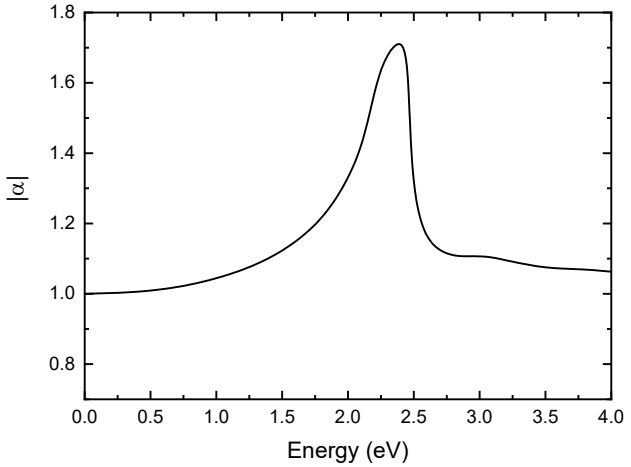

Figure 2.2 Fröhlich condition for a gold particle. Absolute value of the polarizability plotted over the energy. Values of the dielectric function are taken from Ref. [45]

.

The plasmon mode associated with the Fröhlich condition is the dipole surface plasmon. Considering the electrostatic approximation the solution of a ideal dipole is valid. In a more realistic picture retardation effects on the particle need to be taken into account. Considering a plane wave illumination of the form $\mathbf{E(r,t)} = \mathbf{E}_0 e^{-\mathrm{i}\omega t}$ incident on an oscillating dipole (like the metal nanosphere) different radiation zones are present. In the near-field the electrostatic approximation is valid showing the dipole form and the near field ($2\pi r/\lambda \ll 1$) decays with $\propto 1/r^3$. However in the far field ($2\pi r/\lambda \gg 1$) the dipole field shows a spherical form that decays with $\sim 1/r$.[33] Near fields are for example used to go below the wavelength resolution limit in optical near-field microscopy and imaging plasmonic modes.[33]

The localized surface plasmon resonance (LSPR) strongly depends on the shape, size, and material of the metallic nanoparticles.[34;35] It is possible to calculate different shapes of the particle by solving the Laplace equation, but the calculation gets more complex,

if the particle is not symmetric. If the particle is larger than 100 nm the electrostatic approximation is not valid anymore and the problem has to be treated electrodynamically as was introduced in the framework of Mie theory.[46] Mie theory allows to calculate higher-order plasmonic modes as well.

So far I have introduced the localized surface plasmon resonance of a single metal nanoparticle. For the later understanding of this work it is important to consider two particles in close vicinity to each other forming a dimer. If the two particles interact with each other, their plasmonic near fields can couple depending on the polarization of the incident light. For polarization perpendicular to the interparticle axis they act as single particles with individual near fields, see Fig. 2.3 (a). If the polarization of the exciting light matches the interparticle axis the near fields couple forming a plasmonic hotspot in the gap between the two particles, see Fig. 2.3 (b). The coupling of two particles can be described via dipole-dipole coupling or hybridization of the plasmonic modes.[33;47] Additional to the single particle parameters (shape, size, and material) the

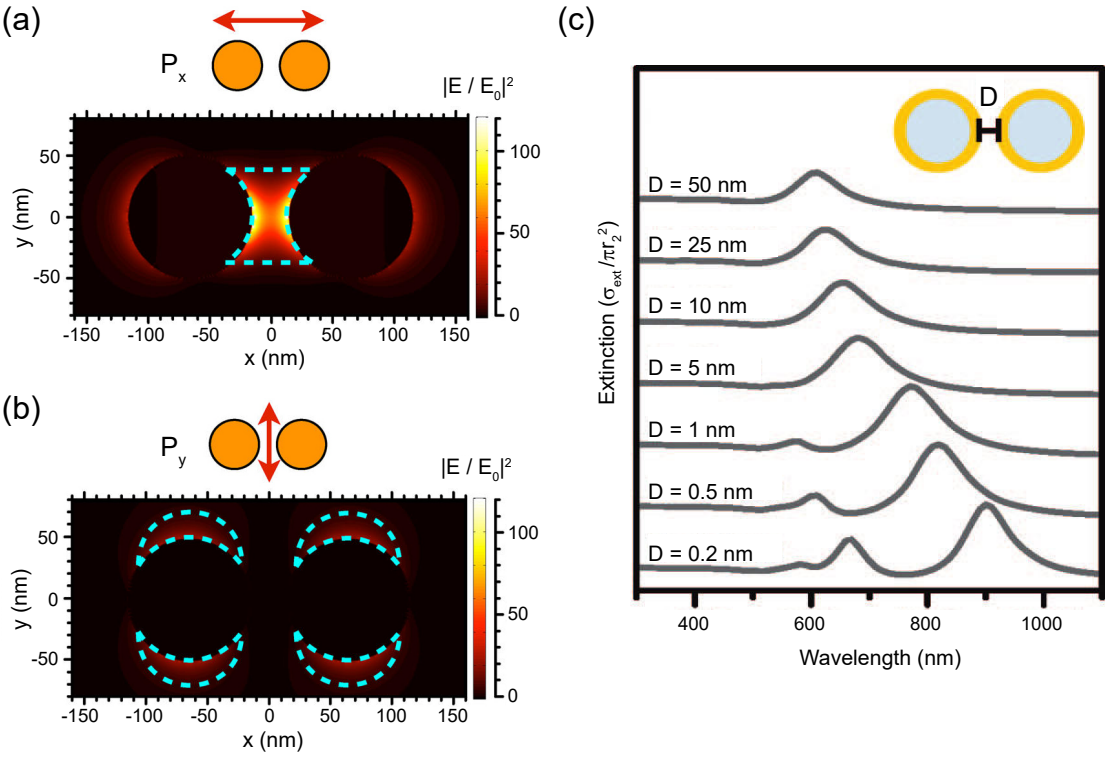

Figure 2.3 Simulated plasmonic near field of two gold discs forming a dimer with polarization **(a)** along and **(b)** perpendicular to the interparticle axis. **(c)** Simulated extinction spectra of nanoshell dimers with varying gapsize. **(a)** and **(b)** adapted from Ref. [27]; **(c)** adapted from Ref. [48].

plasmon resonance of coupled particles depends on the gap size, see Fig. 2.3 (c). With decreasing gap size the LSPR of the dimer red shifts.[36] The charge distribution in the neighboring particle leads to smaller repulsive forces in the plasma electrons.[49] At very small gap sizes below 1 nm tunneling effects have to be taken into account forming a charge transfer plasmon that is blue shifted.[48]

3 | Raman scattering

Inelastic light scattering was first observed by C. Raman in 1928.[1] This chapter addresses the fundamentals behind the Raman scattering process. First I will introduce the macroscopic and microscopic theory of Raman scattering. Then, I will discuss two mechanisms to enhance the Raman scattering process: Resonant Raman scattering and surface-enhanced Raman scattering.

3.1 Macroscopic theory

In the macroscopic theory an electromagnetic field $\mathbf{E}(\mathbf{r}, t)$ is assumed to be present in an infinite isotropic medium with electric susceptibility χ.[50] The field is described by a plane wave:

$$\mathbf{E}(\mathbf{r}, t) = \mathbf{E}_i(\mathbf{k}_i, \omega_i) \cos(\mathbf{k}_i \cdot \mathbf{r} - \omega_i t), \tag{3.1}$$

where $\mathbf{k}$ is the wave vector which gives the propagation direction, ω is the frequency of the wave, and $\mathbf{E}_i$ its initial amplitude.

The field induces a polarization $\mathbf{P}(\mathbf{r}, t)$ with the same frequency and wave vector as the incident field with the amplitude:

$$\mathbf{P}(\mathbf{k}_i, \omega_i) = \chi(\mathbf{k}_i, \omega_i)\mathbf{E}_i(\mathbf{k}_i, \omega_i) \tag{3.2}$$

A finite temperature leads to fluctuations in χ due to thermally excited atomic vibrations. Atomic vibrations in a crystal can be quantized into phonons where the displacement $\mathbf{Q}(\mathbf{r}, t)$ can be expressed as plane wave:

$$\mathbf{Q}(\mathbf{r}, t) = \mathbf{Q}_0(\mathbf{q}, \omega_0) \cos(\mathbf{q} \cdot \mathbf{r} - \omega_0 t), \tag{3.3}$$

with wave vector $\mathbf{q}$ and frequency ω_0. With the assumption that the characteristic

electron frequency that determines χ is much larger than ω_0, the susceptibility can be written as function of the atomic displacement. Normally the amplitude of these vibrations are small compared to the lattice constant, therefore χ can be expanded as a Taylor series in $\mathbf{Q}(\mathbf{r}, t)$:

$$\chi(\mathbf{k}_i, \omega_i, \mathbf{Q}) = \chi_0(\mathbf{k}_i, \omega_i) + \left(\frac{\partial \chi}{\partial \mathbf{Q}}\right)_0 \mathbf{Q}(\mathbf{r}, t) + \dots \ . \tag{3.4}$$

The first term describes the electric susceptibility of the medium without any fluctuations and the second term the oscillating susceptibility induced by the lattice wave $\mathbf{Q}(\mathbf{r}, t)$. Inserting Eq. (3.4) in (3.2) gives:

$$\mathbf{P}(\mathbf{r}, t, \mathbf{Q}) = \mathbf{P}_0(\mathbf{r}, t) + \mathbf{P}_{ind}(\mathbf{r}, t, \mathbf{Q}), \tag{3.5}$$

with

$$\mathbf{P}_0(\mathbf{r}, t) = \chi_0(\mathbf{k}_i, \omega_i)\mathbf{E}_i(\mathbf{k}_i, \omega_i)\cos(\mathbf{k}_i \cdot \mathbf{r} - \omega_i t), \tag{3.6}$$

$$\mathbf{P}_{ind}(\mathbf{r}, t, \mathbf{Q}) = \left(\frac{\partial \chi}{\partial \mathbf{Q}}\right)_0 \mathbf{Q}(\mathbf{r}, t)\mathbf{E}_i(\mathbf{k}_i, \omega_i)\cos(\mathbf{k}_i \cdot \mathbf{r} - \omega_i t), \tag{3.7}$$

where $\mathbf{P}_0(\mathbf{r}, t)$ is the polarization in phase with the incident field and $\mathbf{P}_{ind}(\mathbf{r}, t, \mathbf{Q})$ is the polarization induced by the phonon. Rewriting the induced polarization to determine its frequency and wave vector gives:

$$\begin{aligned}\mathbf{P}_{ind}(\mathbf{r}, t, \mathbf{Q}) = \frac{1}{2}\left(\frac{\partial \chi}{\partial \mathbf{Q}}\right)_0 \mathbf{Q}_0(\mathbf{q}, \omega_0)\mathbf{E}_i(\mathbf{k}_i, \omega_i) \\ \cdot (\cos((\mathbf{k}_i + \mathbf{q}) \cdot \mathbf{r} - (\omega_i + \omega_0)t) + \cos((\mathbf{k}_i - \mathbf{q}) \cdot \mathbf{r} - (\omega_i - \omega_0)t)).\end{aligned} \tag{3.8}$$

$\mathbf{P}_{ind}(\mathbf{r}, t, \mathbf{Q})$ consists of an Anti-Stokes shifted wave with wave vector $\mathbf{k}_{AS} = \mathbf{k}_i + \mathbf{q}$ and frequency $\omega_{AS} = \omega_i + \omega_0$ and a Stokes shifted wave with wave vector $\mathbf{k}_{St} = \mathbf{k}_i - \mathbf{q}$ and frequency $\omega_{St} = \omega_i - \omega_0$. The shift is called Raman shift and describes the frequency shift of the scattered light with respect to the incoming light. Equation (3.8) gives first order Raman scattering; the Taylor series can be further extended to get expressions for higher orders.

3.2 Microscopic theory

The Raman process can also be described quantum mechanically, called microscopical picture, which will be used to describe the coupling of the LSP to graphene, discussed in

Chapt. 2. The Stokes and Anti-Stokes process are schematically shown in Fig. 3.1.

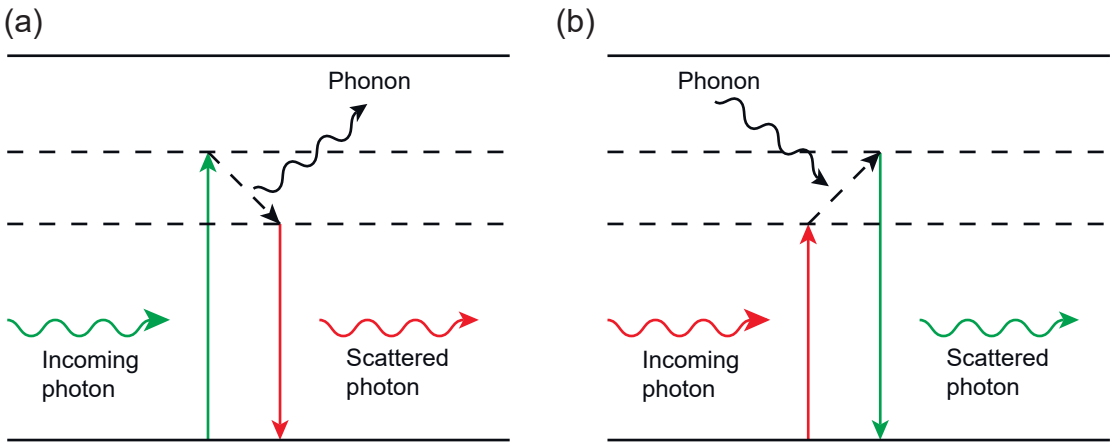

Figure 3.1 An incoming photon is absorbed and excites an electron. It interacts with the lattice by **(a)** creating (Stokes process) or **(b)** annihilating (Anti-Stokes process) a phonon emitting a photon. Solid lines represent real states while dashed lines are virtual states.

The incoming photon ω_i interacts with the electrons and creates an electron-hole pair. This pair is then scattered into another state by creating a phonon ω_{pn}. Finally, the electron-hole pair recombines and emits a photon ω_s. The energy of the scattered photon is equal to the energy difference of the incoming photon and the phonon: $\hbar\omega_s = \hbar\omega_i - \hbar\omega_{pn}$. In the Stokes process, the incoming light with frequency ω_i is scattered under creation of a phonon. The energy of the scattered light is $\hbar\omega_{St} = \hbar\omega_i - \hbar\omega_{pn}$. The Anti-Stokes process describes the scattering of light on an already existing phonon. The energy of the scattered light $\hbar\omega_{AS}$ is therefore higher than it was before the scattering process: $\hbar\omega_{AS} = \hbar\omega_i + \hbar\omega_{pn}$. This thesis will only address the Stokes process. When the energy of the incoming photon approaches the fundamental absorption edge, the Raman scattering efficiency is enhanced, which is called resonant Raman scattering (see below).

The quantum mechanical description is very helpful to calculate the transition probability. Therefore the scattering process is depicted in a Feynman diagram. Figure 3.2 shows the most probable Stokes process.

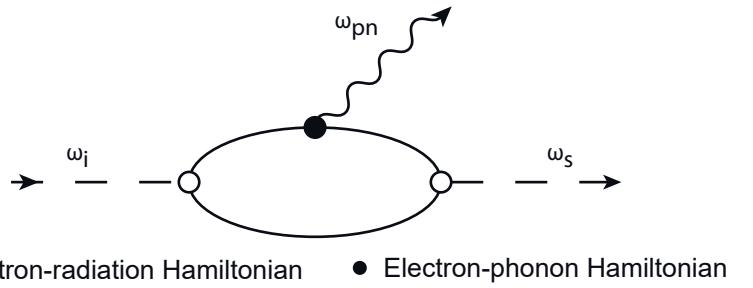

Figure 3.2 Feynman diagram for the most probable Stokes process. Dashed lines show photons; the curved line a phonon; circles are interaction Hamiltonians.

The transition probability of this process can be calculated using Fermi's golden rule:[50]

$$P_{Ra}(\omega_s) = \left(\frac{2\pi}{\hbar}\right) \left| \sum_{n,n'} \frac{\langle i|H_{pt-el}(\omega_s)|n'\rangle\langle n'|H_{pn-el}|n\rangle\langle n|H_{el-pt}(\omega_i)|i\rangle}{(\hbar\omega_s - \epsilon_{\mathbf{k}}^{\pi *\prime} - \mathrm{i}\frac{\gamma'_{el}}{2})(\hbar\omega_i - \epsilon_{\mathbf{k}}^{\pi *} - \mathrm{i}\frac{\gamma_{el}}{2})} \right|^2 \cdot\delta[\hbar\omega_i - \hbar\omega_{pn} - \hbar\omega_s], \tag{3.9}$$

with the different scattering matrix elements in the numerator, where $|i\rangle$ is the initial, $|n\rangle$ and $|n'\rangle$ are intermediate states. H is the Hamilton operator describing the interaction between different states, the damping constants are γ'_{el}, and γ_{el} and the energies of the virtual electronic states are $\epsilon_{\mathbf{k}}^{\pi *}$ and $\epsilon_{\mathbf{k}}^{\pi *\prime}$. The Raman process includes different time orders, leading to other scattering paths, where the sum is the total transition probability.[50]

Light provided by lasers in the visible regime is a common excitation source for the Raman process. With visible light, it is only possible to excite the Raman process at the Γ-point in the reciprocal lattice ($\mathbf{q}$=0), because the wave vector of the light is much smaller than the Brillouin zone. Two-phonon processes can also be excited for a pair of phonons with opposite wave vector ($\mathbf{q}$,$\mathbf{q}$').[51]

Resonant Raman scattering

If the energy of the incoming light or the scattered light matches an electronic interband transition, the Raman process shows a resonance behavior. Because of the two resonance conditions in Eq. (3.9), two resonances can occur: the incoming (for the incident light) and outgoing (for the scattered light) resonance. The energy difference between both matches exactly the phonon energy. By tuning the excitation energy and monitoring a specific Raman mode of the analyte, the electronic transitions can be determined

experimentally.

$$I(E_l) = \left| \frac{M}{(E_l - E_{res} - \omega_{pn} - i\gamma_{res})(E_l - E_{res} - i\gamma_{res})} \right|^2 , \tag{3.10}$$

where E_l is the excitation energy, E_{res} the resonance energy, and γ_{res} the width of the resonance. Because of the complex character of the width the intensities at the resonances remain finite. Equation (3.10) is used to fit resonant Raman profiles.

3.3 Surface-enhanced Raman scattering

Plasmonic near fields as described in Chapt. 2 can enhance the Raman scattering process. The effect was first observed in 1974 on molecules adsorbed on a silver electrode and later named surface-enhanced Raman scattering.[7;52;8] Different theories have been proposed explaining the mechanics of SERS. The fundamentals behind SERS are still under discussion.[17] I will introduce the electromagnetic enhancement theory and the higher-order Raman scattering mechanism incorporating the interaction of the Raman scattering process within the microscopic theory of Raman scattering introduced above. Furthermore, I will comment on the so-called chemical enhancement that describes the direct interaction between the metal and the Raman reporter.

Electromagnetic enhancement theory

The EM enhancement theory describes the interaction of the plasmonic near field with the incoming and scattered light in the Raman process. In the picture of the electromagnetic enhancement the plasmonic near field is treated as an external effect. The electromagnetic near field surrounding the metal nanoparticles enhances the incoming and scattered light. The scattering intensity of the Raman process scales linearly with the incoming light intensity $\mathbf{E}_0^2$.[53] The exciting light in the vicinity of the nanoparticle gets enhanced by the plasmonic near field $|\mathbf{E}_{out}|^2$ outside of the particle. In Chapt. 2 I derived the plasmonic near field outside of a spherical particle. The scattered light is enhanced by the plasmonic near field $|\mathbf{E}'_{out}|^2$ as well, but at the Stokes shifted frequency. The enhancement factor is calculated with

$$EF = \frac{|\mathbf{E}_{out}|^2 \cdot |\mathbf{E}_{out}{}'|^2}{\mathbf{E}_0^4}. \tag{3.11}$$

Assuming a small Stokes shift the exciting and scattered light have approximately the same frequency resulting in the $\mathbf{E}^4$ enhancement.[3]

In experiments it is more common to compare the plasmonically enhanced Raman intensity with a reference without plasmonic enhancement. To compare different nanoparticles and plasmonic systems the enhancement factor is calculated per enhanced molecule.

$$EF = \frac{I_{SERS} \cdot n_{SERS}}{I_{Raman} \cdot n_{Raman}}, \tag{3.12}$$

where n_{SERS} and n_{Raman} are the number of Raman reporters in the plasmonic near field and without plasmonic enhancement, respectively. In Eq. (3.12) there are two contributions to the enhancement factor, the reference without enhancement and the enhanced Raman intensity. In the reference Raman intensity I_{Raman} it is essential to carefully discuss the dielectric environment of the Raman reporter as well as possible intrinsic resonances of the Raman reporter.[5] The number of Raman reporters n_{Raman} is determined by the size of the laser focus and the concentration of molecules. The enhanced Raman intensity I_{SERS} is additionally dependent on the plasmon resonance that is wavelength dependent. The number of reporters in the plasmonic hotspot n_{SERS} depends on the size of the plasmonic near field and the orientation of the molecules compared to the near field. The size of the hotspot depends on the geometry of the plasmonic particles and can for example be deducted from finite difference time domain simulations.

Higher-order Raman scattering theory

In the HORa theory the interaction between the plasmon and the Raman process is treated quantum mechanically.[21] In form of Feynman diagrams it is possible to describe the combined process, as in the microscopical Raman description (see Chapt. 3.2). Applying Fermi's golden rule the scattering probabilities of the different scattering channels can be derived.

In the quantum mechanical framework it is important to consider quantum interference between different scattering channels. Incorporating the plasmonic interaction the HORa theory distinguishes between four scattering channels resulting in the same final state in which one phonon is created and one photon emitted: i) the common Raman process (no plasmonic interaction), ii) the plasmon only interacts with the incoming light, iii) the plasmon interacts only with the scattered light, and iv) the plasmon interacts with both the incoming and scattered photon. The total intensity is the sum of the four scattering channels because interference of these must be taken into account. The

transition probability of each scattering path can be calculated with:

$$T_{i\to f} = \frac{2\pi}{\hbar}\left|\sum_{\mathbf{k},\alpha} K_\alpha(\mathbf{k})\right|^2 \cdot \delta(\hbar\omega_i - \hbar\omega_s - \hbar\omega_{pn}), \tag{3.13}$$

where ω_i is the frequency of the incoming light, ω_s of the outgoing light, and ω_{pn} the phonon frequency. $K_\alpha(\mathbf{k})$ are the Raman matrix elements.

Case i

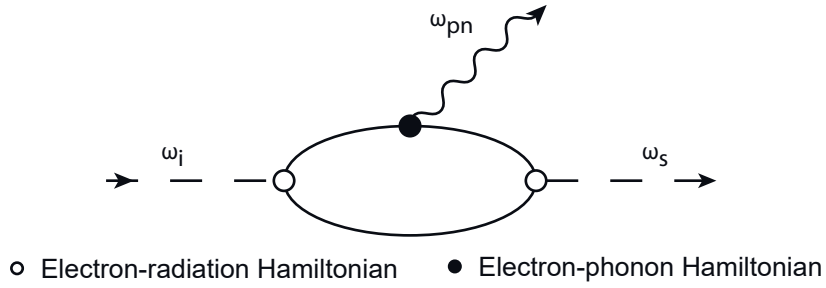

Figure 3.3 Microscopic Raman process as described in Chapt. 3.2.

The first process is the "ordinary" Raman scattering (Fig. 3.3) described in Chapt. 3.2 with:

$$K_{pn-pn} = \frac{M_{pt-el}M_{pn-el}M_{el-pt}}{(\hbar\omega_i - \hbar\omega_{pn} - \epsilon^{\pi^*\prime} - \mathrm{i}\frac{\gamma'_{el}}{2})(\hbar\omega_i - \epsilon^{\pi*} - \mathrm{i}\frac{\gamma_{el}}{2})}. \tag{3.14}$$

The matrix elements are:

$$M_{el-pt} = \langle k\pi^*, 0^{LSP}, 0^{pn}, 0^{pt}\,|H_{el-pt}|\,k\pi, 0^{LSP}, 0^{pn}, 1^{pt}_{\omega_i,\mathbf{q},\alpha}\rangle \tag{3.15}$$

$$M_{pn-el} = \langle k\pi^{*\prime}, 0^{LSP}, 1^{pn}_{\omega_{pn}}, 0^{pt}\,|H_{pn-el}|\,k\pi^*, 0^{LSP}, 0^{pn}, 0^{pt}\rangle \tag{3.16}$$

$$M_{pt-el} = \langle k\pi, 0^{LSP}, 1^{pn}_{\omega_{pn}}, 1^{pt}_{\omega_s,\mathbf{q}',\alpha'}\,|H_{pt-el}|\,k\pi^{*\prime}, 0^{LSP}, 1^{pn}_{\omega_{pn}}, 0^{pt}\rangle \tag{3.17}$$

Case ii

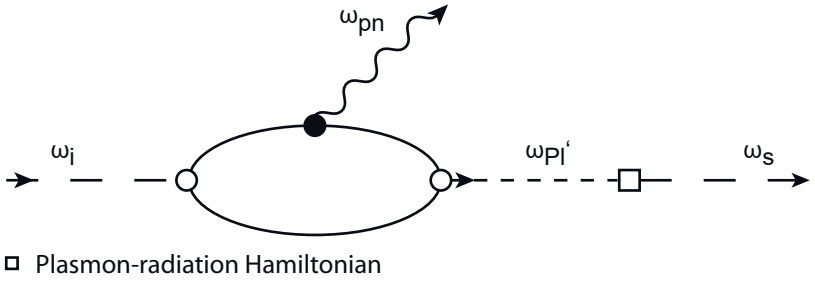

Figure 3.4 Microscopic picture of the interaction of the analyte with the near field of the LSP after phonon excitation.

The second case includes the interaction of the analyte with the LSP. First, the incoming light is Raman scattered at the analyte. The relaxation of the electron-hole pair induces a LSP which then emits the scattered light, depicted in Fig. 3.4.

The matrix element for this process is:

$$K_{pn-LSP} = \frac{M_{pt-LSP} M_{LSP-el} M_{pn-el} M_{el-pt}}{(\hbar\omega_i - \hbar\omega'_{LSP} - \hbar\omega_{pn} - \mathrm{i}\frac{\gamma'_{LSP}}{2})(\hbar\omega_i - \hbar\omega_{pn} - \epsilon^{\pi^{*\prime}} - \mathrm{i}\frac{\gamma'_{el}}{2})} \cdot \frac{1}{(\hbar\omega_i - \epsilon^{\pi*} - \mathrm{i}\frac{\gamma_{el}}{2})}, \tag{3.18}$$

with

$$M_{el-pt} = \langle k\pi^*, 0^{LSP}, 0^{pn}, 0^{pt} \left| H_{el-pt} \right| k\pi, 0^{LSP}, 0^{pn}, 1^{pt}_{\omega_i,\mathbf{q},\alpha} \rangle \tag{3.19}$$

$$M_{pn-el} = \langle k\pi^{*\prime}, 0^{LSP}, 1^{pn}_{\omega_{pn}}, 0^{pt} \left| H_{pn-el} \right| k\pi^*, 0^{LSP}, 0^{pn}, 0^{pt} \rangle \tag{3.20}$$

$$M_{LSP-el} = \langle k\pi, 1^{LSP}_{\omega'_{LSP},\mathbf{q}'_{LSP}}, 1^{pn}_{\omega_{pn}}, 0^{pt} \left| H_{LSP-el} \right| k\pi^{*\prime}, 0^{LSP}, 1^{pn}_{\omega_{pn}}, 0^{pt} \rangle \tag{3.21}$$

$$M_{pt-LSP} = \langle k\pi, 0^{LSP}, 1^{pn}_{\omega_{pn}}, 1^{pt}_{\omega_s,\mathbf{q}',\alpha'} \left| H_{LSP-el} \right| k\pi, 1^{LSP}_{\omega'_{LSP},\mathbf{q}'_{LSP}}, 1^{pn}_{\omega_{pn}}, 0^{pt} \rangle \tag{3.22}$$

Case iii

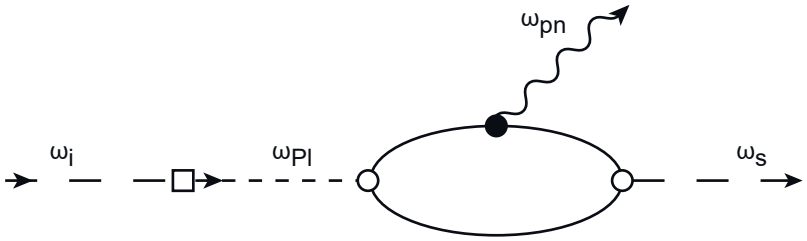

Figure 3.5 Microscopic picture of the interaction of the analyte with the near field of the LSP exciting the phonon excitation.

This process can also happen in reverse order, see Fig. 3.5, where the incoming light excites the LSP starting up the Raman scattering process with the following matrix element:

$$K_{LSP-pn} = \frac{M_{pt-el}M_{pn-el}M_{el-LSP}M_{LSP-pt}}{(\hbar\omega_i - \epsilon^{\pi^{*\prime}} - \hbar\omega_{pn} - \mathrm{i}\frac{\gamma'_{el}}{2})(\hbar\omega_i - \hbar\omega_{pn} - \epsilon^{\pi^*} - \mathrm{i}\frac{\gamma_{el}}{2})} \cdot \frac{1}{(\hbar\omega_i - \hbar\omega_{LSP} - \mathrm{i}\frac{\gamma_{LSP}}{2})}, \tag{3.23}$$

with

$$M_{LSP-pt} = \langle k\pi, 1^{LSP}_{\omega_{LSP},\mathbf{q}_{LSP}}, 0^{pn}, 0^{pt} \left| H_{LSP-pt} \right| k\pi, 0^{LSP}, 0^{pn}, 1^{pt}_{\omega_i,\mathbf{q},\alpha} \rangle \tag{3.24}$$

$$M_{el-LSP} = \langle k\pi^*, 0^{LSP}, 0^{pn}, 0^{pt} \left| H_{el-LSP} \right| k\pi, 1^{LSP}_{\omega_{LSP},\mathbf{q}_{LSP}}, 0^{pn}, 0^{pt} \rangle \tag{3.25}$$

$$M_{pn-el} = \langle k\pi^{*\prime}, 0^{LSP}, 1^{pn}_{\omega_{pn}}, 0^{pt} \left| H_{pn-el} \right| k\pi^*, 0^{LSP}, 0^{pn}, 0^{pt} \rangle \tag{3.26}$$

$$M_{pt-el} = \langle k\pi, 0^{LSP}, 1^{pn}_{\omega_{pn}}, 1^{pt}_{\omega_s,\mathbf{q}',\alpha'} \left| H_{pt-el} \right| k\pi^{*\prime}, 0^{LSP}, 1^{pn}_{\omega_{pn}}, 0^{pt} \rangle \tag{3.27}$$

Case iv

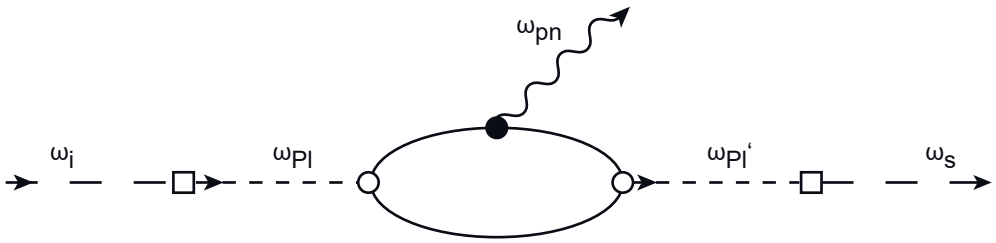

Figure 3.6 Microscopic picture of the interaction of the analyte with the near field of the LSP before and after phonon excitation.

The last possibility is that the Raman scattering is induced by a LSP and also induces

itself a LSP, shown in Fig. 3.6.

$$K_{LSP-LSP} = \frac{M_{pt-LSP}M_{LSP-el}M_{el-pn}M_{el-LSP}M_{LSP-pt}}{(\hbar\omega_i - \hbar\omega'_{LSP} - \hbar\omega_{pn} - \mathrm{i}\frac{\gamma'_{LSP}}{2})(\hbar\omega_i - \epsilon^{\pi^{*\prime}} - \hbar\omega_{pn} - \mathrm{i}\frac{\gamma'_{el}}{2})} \cdot \frac{1}{(\hbar\omega_i - \hbar\omega_{pn} - \epsilon^{\pi^*} - \mathrm{i}\frac{\gamma_{el}}{2})(\hbar\omega_i - \hbar\omega_{LSP} - \mathrm{i}\frac{\gamma_{LSP}}{2})}, \tag{3.28}$$

with

$$M_{LSP-pt} = \langle k\pi, 1^{LSP}_{\omega_{LSP},\mathbf{q}_{LSP}}, 0^{pn}, 0^{pt} \,|H_{LSP-pt}|\, k\pi, 0^{LSP}, 0^{pn}, 1^{pt}_{\omega_i,\mathbf{q},\alpha}\rangle \tag{3.29}$$

$$M_{el-LSP} = \langle k\pi^*, 0^{LSP}, 0^{pn}, 0^{pt} \,|H_{el-LSP}|\, k\pi, 1^{LSP}_{\omega_{LSP},\mathbf{q}_{LSP}}, 0^{pn}, 0^{pt}\rangle \tag{3.30}$$

$$M_{el-pn} = \langle k\pi^{*\prime}, 0^{LSP}, 1^{pn}_{\omega_{pn}}, 0^{pt} \,|H_{pn-el}|\, k\pi^*, 0^{LSP}, 0^{pn}, 0^{pt}\rangle \tag{3.31}$$

$$M_{LSP-el} = \langle k\pi, 1^{LSP}_{\omega'_{LSP},\mathbf{q}'_{LSP}}, 1^{pn}_{\omega_{pn}}, 0^{pt} \,|H_{LSP-el}|\, k\pi^{*\prime}, 0^{LSP}, 1^{pn}_{\omega_{pn}}, 0^{pt}\rangle \tag{3.32}$$

$$M_{pt-LSP} = \langle k\pi, 0^{LSP}, 1^{pn}_{\omega_{pn}}, 1^{pt}_{\omega_s,\mathbf{q}',\alpha'} \,|H_{LSP-el}|\, k\pi, 1^{LSP}_{\omega'_{LSP},\mathbf{q}'_{LSP}}, 1^{pn}_{\omega_{pn}}, 0^{pt}\rangle \tag{3.33}$$

Total transition probability The total transition probability for the relevant scattering processes is described by:

$$T_{i\to f} = \frac{2\pi}{\hbar}\left|\sum_{\mathbf{k}_1} K_{LSP-LSP}(\mathbf{k}_1) + \sum_{\mathbf{k}_2} K_{pn-LSP}(\mathbf{k}_2) + \sum_{\mathbf{k}_3} K_{LSP-pn}(\mathbf{k}_3) + \sum_{\mathbf{k}_4} K_{Raman}(\mathbf{k}_4)\right|^2 \cdot \delta(\hbar\omega_i - \hbar\omega_s - \hbar\omega_{pn}). \tag{3.34}$$

Factoring out the Raman process gives the following expression:

$$T_{i\to f} = \frac{2\pi}{\hbar}\left|\frac{M_{pt-LSP}M_{LSP-el}M_{el-LSP}M_{LSP-pt}/(M_{pn-el}M_{el-pn})}{(\hbar\omega_i - \hbar\omega'_{LSP} - \hbar\omega_{pn} - \mathrm{i}\frac{\gamma'_{LSP}}{2})(\hbar\omega_i - \hbar\omega_{LSP} - \mathrm{i}\frac{\gamma_{LSP}}{2})} + \frac{M_{pt-LSP}M_{LSP-el}/M_{pn-el}}{\hbar\omega_i - \hbar\omega'_{LSP} - \hbar\omega_{pn} - \mathrm{i}\frac{\gamma'_{LSP}}{2}} + \frac{M_{el-LSP}M_{LSP-pt}/M_{el-pt}}{\hbar\omega_i - \hbar\omega_{LSP} - \mathrm{i}\frac{\gamma_{LSP}}{2}} + 1\right|^2 \cdot \sum_{\mathbf{k}}\left|\frac{M_{pt-el}M_{pn-el}M_{el-pt}}{(\hbar\omega_i - \hbar\omega_{pn} - \epsilon^{\pi^{*\prime}} - \mathrm{i}\frac{\gamma'_{el}}{2})(\hbar\omega_i - \epsilon^{\pi*} - \mathrm{i}\frac{\gamma_{el}}{2})}\right|^2 \cdot \delta(\hbar\omega_i - \hbar\omega_s - \hbar\omega_{pn}). \tag{3.35}$$

Interpreting:

$$\tilde{M} = \frac{M_{el-LSP}M_{LSP-pt}}{M_{el-pn}} = \frac{M_{pt-LSP}M_{LSP-el}}{M_{pn-el}} \tag{3.36}$$

as the coupling parameter between the LSP and the analyte. With the assumptions that $\omega'_{LSP} = \omega_{LSP}$ and $\gamma_{LSP} = \gamma'_{LSP}$ it leads to:

$$T_{i\to f} \propto \left| \frac{\tilde{M}^2}{(\hbar\omega_i - \hbar\omega_{LSP} - \hbar\omega_{pn} - \mathrm{i}\frac{\gamma_{LSP}}{2})(\hbar\omega_i - \hbar\omega_{LSP} - \mathrm{i}\frac{\gamma_{LSP}}{2})} + \frac{\tilde{M}}{\hbar\omega_i - \hbar\omega_{LSP} - \hbar\omega_{pn} - \mathrm{i}\frac{\gamma_{LSP}}{2}} - \frac{\tilde{M}}{\hbar\omega_i - \hbar\omega_{LSP} - \mathrm{i}\frac{\gamma_{LSP}}{2}} + 1 \right|^2 . \tag{3.37}$$

Equation (3.37) describes the enhancement behavior of the coupled system. The magnitude and ratio of the incoming to outgoing resonance depend on the coupling strength.

Chemical enhancement

An additional enhancement mechanism beside the EM mechanism, called chemical enhancement, describes the enhancement due to charge transfer states between the metal and the Raman reporter. Chemical enhancement can attribute to the enhancement by a factor of up to 100.[9] The Raman reporter must be adsorbed directly on the metal to enable chemical enhancement. The enhancement mechanism is similar to resonant Raman scattering. The electronic states of the reporter molecule can be shifted or broadened by the interaction with the metal or new states are created by the adsorption and act as real states in resonant Raman scattering.[54] Chemical enhancement is therefore dependent on the reporter and the metal surface.[55]

4 | Carbon nanomaterials

Carbon nanomaterials occur in different forms. In zero dimensions as fullerenes with different numbers of carbon atoms, in one dimension as carbon nanotubes and in two dimensions as graphene. Multiple layers of graphene form the three dimensional crystal graphite. In this chapter, I will discuss various properties of graphene and CNTs, especially their Raman spectra.

4.1 Graphene

Graphene is a two dimensional flat semimetal consisting of a single layer of graphite. Graphene has many interesting properties like very high electron mobility[56], thermal conductivity[57], high inherent strength[58], among others.[59;60] In graphite comparably weak van der Waals forces couple the different layers. The carbon atoms within the plane, in contrast, are bound by covalent forces where three of the carbon electrons form an sp^2 network. The orbital of the fourth electron is a π-orbital perpendicular to the carbon plane forming a delocalized electron band.

Graphene has a hexagonal lattice structure with two carbon atoms per unit cell. The unit cell is described by the lattice vectors $\mathbf{a}_1$ and $\mathbf{a}_2$ as shown in real space in Fig. 4.1 (a). Neighboring carbon atoms have a distance of $d_{C-C} = 0.142$ nm. The lattice basis vectors have a length of $|\mathbf{a}_1| = |\mathbf{a}_1| = 0.264$ nm. Figure 4.1 (b) shows the graphene lattice in reciprocal space with the reciprocal lattice vectors $\mathbf{b}_1$ and $\mathbf{b}_2$. The high symmetry points Γ, K, K$'$, and M are indicated.

To understand the Raman spectrum of graphene it is important to consider the phonon dispersion, see Fig. 4.1 (c). With the two atomic basis graphene exhibits three acoustical (A) and three optical phonon branches (O). The phonons are divided to in-plane longitudinal (L), in-plane transversal (T), and out-of-plane (Z) phonons.

Graphene has a linear electronic dispersion at the Γ and K point. At the K and K$'$ points the valence and conduction bands touch, called Dirac points. For undoped

graphene the valence band is completely filled. The Fermi energy is located at the Dirac points. The K point plays an important role in Raman scattering, because the D and 2D mode are related to the K point, as discussed below when the Raman spectrum of graphene is introduced. The optical phonon at the Γ-point is twofold degenerated.

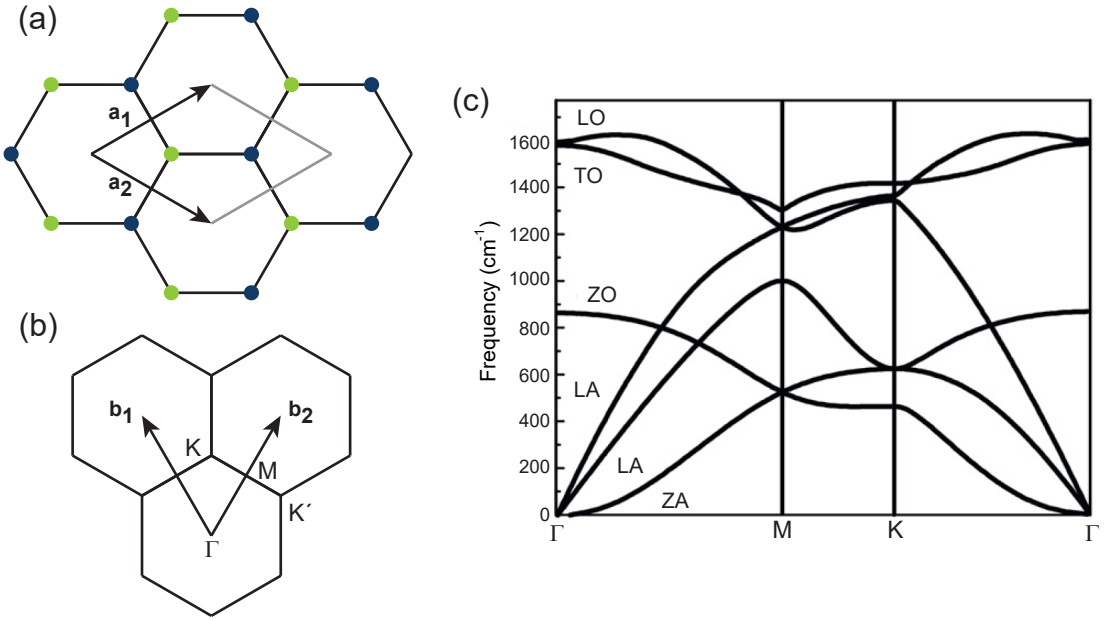

Figure 4.1 **(a)** Hexagonal graphene lattice with lattice vectors $\mathbf{a}_1$ and $\mathbf{a}_2$. **(b)** Graphene lattice in reciprocal space. The reciprocal vectors $\mathbf{b}_1$ and $\mathbf{b}_2$ and the high symmetry points are indicated. **(c)** Phonon dispersion of graphene. The phonon branches are labeled. Figure adapted from Ref. [61]

Many different properties of graphene like layer number, quality, strain, doping, and more can be investigated by Raman spectroscopy.[51] The next part introduces the Raman spectrum of graphene and the influence of strain and doping on the Raman modes.

Raman spectrum of graphene

The Raman modes of graphene are located in the range between 1200 cm^{-1} and 3400 cm^{-1}. Figure 4.2 (a) shows typical Raman spectra of graphene. The top panel shows a Raman spectrum of graphene without defects and the lower panel one of graphene with defects. The G and 2D mode are present in both spectra whereas the D and D′ mode are mainly observed in defective graphene.

The G mode is the only first order scattering mode in graphene. It is located at $\omega_G = 1582$ cm^{-1} and stems from the doubly degenerate E_{2g} optical phonon at the Γ

point. Figure 4.2 (b) shows the scattering path of the G mode. In Fig. 4.2 (b)-(e), the black lines show the electronic dispersion of graphene. The green arrow indicates the incoming light that excites an electron. Dashed lines show the phonon scattering and the red arrows the scattered light. The initial and final state must be the same due to energy and momentum conservation.

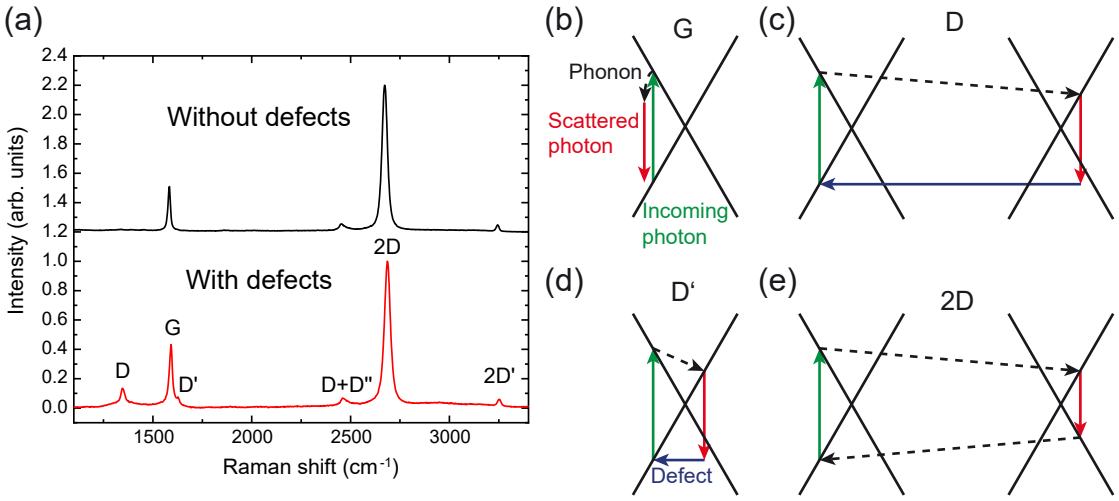

Figure 4.2 **(a)** Typical Raman spectra of graphene without (top) and with (bottom) defects. The different Raman modes are labeled. Raman scattering processes in graphene for the **(b)** G, **(c)** D, **(d)** D′, and **(e)** 2D mode. Black lines are the electron dispersion of graphene, green arrows indicate the incoming light, red arrows the scattered light, dashed lines the phonon scattering and blue arrows defect scattering. Only the most probable scattering processes of the respective modes are shown.

The D and D' mode are defect induced.[62] The D mode is associated to the TO branch at the K point. Figure 4.2 (c) depicts the scattering path of the D mode. The D mode is a second order Raman process involving one phonon. The blue arrow indicates defect scattering. Due to momentum conservation a defect is necessary in the formation of the D mode. The D mode is an intervalley process connecting two Dirac cones. The D mode is located at $\omega_D \approx 1350$ cm^{-1} and shows a dispersive behavior with a slope of of ~ 50 cm^{-1}/eV. The D′ mode is defect induced as well at $\omega_{D'} = 1620$ cm^{-1}. In contrast to the D mode it originates from an intravalley process, see Fig. 4.2 (d).

The 2D mode is a second order Raman process. In contrast to the D and D′ mode no defect is required to activate the 2D mode therefore it is observed in pristine graphene. It stems from the TO branch at the K point as the D mode but involves two phonons and is observed at twice the frequency of the D mode at $\omega_{2D} \approx 2600$ cm^{-1}. It shows a dispersive behavior with a slope of 100 cm^{-1}/eV. There are more combination modes

present in the Raman spectrum of graphene that I will not discuss in this thesis. I refer to Ref. [62] for a deeper understanding of the additional modes.

Due to the linear electronic dispersion and the two-dimensional character of graphene the G mode has a constant Raman cross section in the visible regime, meaning the Raman intensity of the G mode does not change with excitation energy. Figure 4.3 (a) shows the excitation energy dependence of the G and 2D mode in graphene. The G mode is constant over the investigated energy dependence whereas the 2D mode is excitation energy dependent.

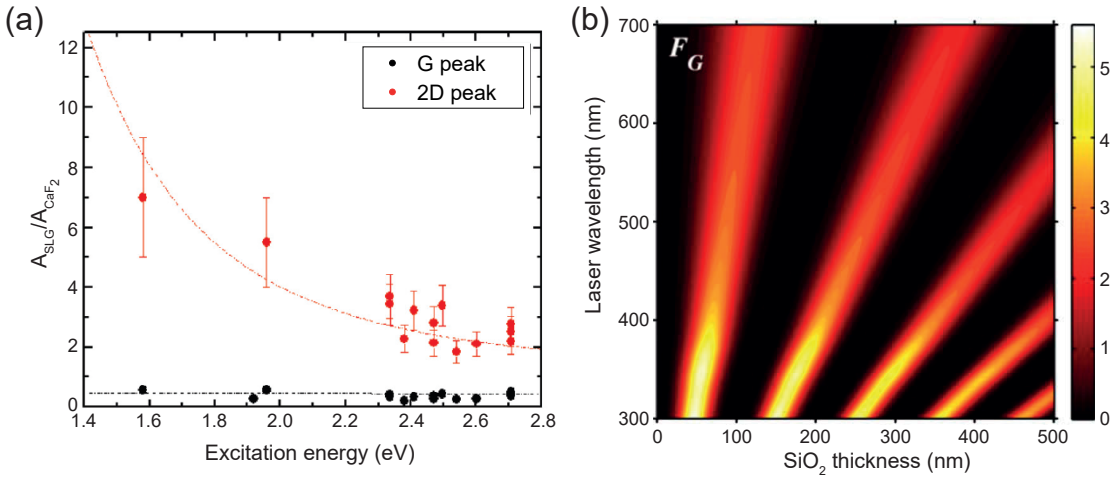

Figure 4.3 **(a)** Excitation energy dependence of the G (black) and 2D (red) mode of graphene. Figure adapted from Ref. [37]. **(b)** Interference effect of graphene suspended on SiO_2. Laser wavelength as function of SiO_2 thickness. The contour is the calculated intensity of the Raman G mode. Figure adapted from Ref. [63].

Even though the Raman cross section of the G mode is constant, changes might be introduced when suspended on a substrate. Figure 4.3 (b) shows the Raman intensity of the G mode as a function of wavelength and SiO_2 thickness which is a common substrate to suspend graphene on. Interference effects at the interface between the graphene and the oxide layer of the substrate and the oxide layer with the silicon lead to wavelength-dependent intensity differences.[63]

Polarization-dependent Raman measurements reveal additional information about the probe. The polarization behavior gives information on the symmetry of the specific Raman mode. Graphene belongs to the D_{6h} point group.[61] The G mode has E_{2g} symmetry

with the following Raman tensors[64]

$$E_{2g}(x) = \begin{pmatrix} 0 & a & 0 \\ a & 0 & 0 \\ 0 & 0 & 0 \end{pmatrix}, \; E_{2g}(y) = \begin{pmatrix} a & 0 & 0 \\ 0 & -a & 0 \\ 0 & 0 & 0 \end{pmatrix}. \tag{4.1}$$

The intensity of the Raman mode depending on the polarization of the incoming and scattered light is given by

$$I \propto \sum |\mathbf{e}_i \cdot R \cdot \mathbf{e}_s|^2, \tag{4.2}$$

where $\mathbf{e}_i$ and $\mathbf{e}_s$ are the incoming and scattered light, respectively, and R the Raman tensor. In the plane of graphene they are described by

$$\mathbf{e}_i = \mathbf{e}_s = \begin{pmatrix} \sin\Theta \\ \cos\Theta \\ 0 \end{pmatrix}, \tag{4.3}$$

where Θ is the polarization angle. Inserting the Raman tensors of the G mode in Eq. (4.2) yields

$$I_G(\Theta) \propto |(\mathbf{e}_i \cdot E_{2g}(x) \cdot \mathbf{e}_s)|^2 + |(\mathbf{e}_i \cdot E_{2g}(y) \cdot \mathbf{e}_s)|^2 = a^2. \tag{4.4}$$

The G mode has constant Raman intensity independent of the polarization angle.

The 2D mode has A_{1G} symmetry with the corresponding Raman tensor

$$A_{1g} = \begin{pmatrix} b & 0 & 0 \\ 0 & b & 0 \\ 0 & 0 & 0 \end{pmatrix}. \tag{4.5}$$

The polarization dependence yields

$$I_{2D}(\Theta) \propto |(\mathbf{e}_i \cdot A_{1g} \cdot \mathbf{e}_s)|^2 = b^2. \tag{4.6}$$

Figure 4.4 shows the measurement of the G and 2D mode depending on the polarization. It confirms the expected behavior of constant Raman intensity.

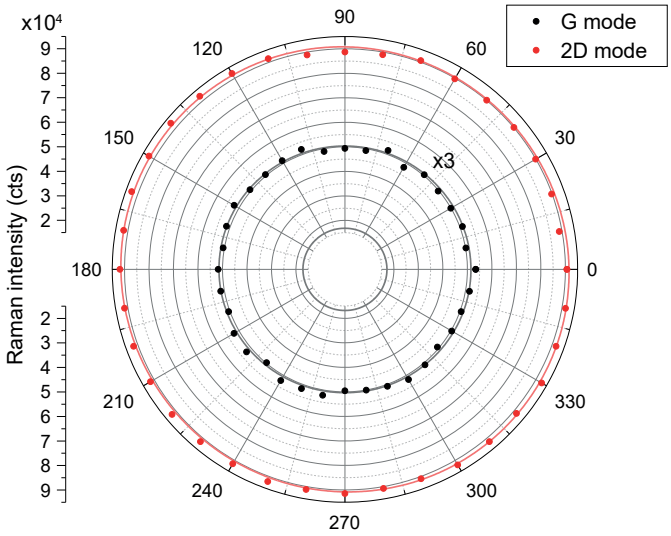

Figure 4.4 Raman intensity as function of polarization angle of the G (black) and 2D (red) mode. Dots are experimental data and solid lines represent the fits. Excitation wavelength $\lambda_l = 532$ nm.

Strain and doping in graphene

Strain and doping modify the properties of graphene and also have a strong influence on the Raman modes due to the distortion of the lattice. By analyzing the position of the G and 2D mode it is possible to determine the strain and doping level for arbitrary configurations.

To analyze the effect of strain on the position of the Raman modes I consider a two dimensional general strain tensor

$$\varepsilon(\mathbf{r}) = \begin{pmatrix} \varepsilon_{xx}(\mathbf{r}) & \varepsilon_{xy}(\mathbf{r}) \\ \varepsilon_{yx}(\mathbf{r}) & \varepsilon_{yy}(\mathbf{r}) \end{pmatrix}, \tag{4.7}$$

with the strain components ε_{ij}. The difference in Raman shift is calculated with [65;66]

$$\Delta\omega_{pn}^{\pm} = -\omega_{pn}^{0}\gamma_{pn}(\varepsilon_{xx} + \varepsilon_{yy}) \pm \frac{1}{2}\omega_{pn}^{0}\beta_{pn}\sqrt{(\varepsilon_{xx} + \varepsilon_{yy})^2 + 4\varepsilon_{xy}^2}, \tag{4.8}$$

where ω_{pn}^{0} is the phonon frequency without strain, γ_{pn} is the Grueneisen parameter, and β_{pn} the shear deformation potential.

In-plane strain in a hexagonal lattice consists of two components: hydrostatic strain and shear strain. Hydrostatic strain describes the isotropic increase or decrease of the graphene lattice resulting in a peak shift. The effect of hydrostatic strain is described

by the Grueneisen parameter. Shear strain characterizes the anisotropic change of the graphene lattice without changing the area of the unit cell; it splits the Raman modes. The shear deformation potential yields the amount of splitting. The mean peak position is unaffected by shear strain and only shifts with hydrostatic strain. The analysis of strain with Eq. (4.8) is only valid for first order Raman scattering. The consequence of peak shifts and splitting due to strain however also applies for the 2D mode.

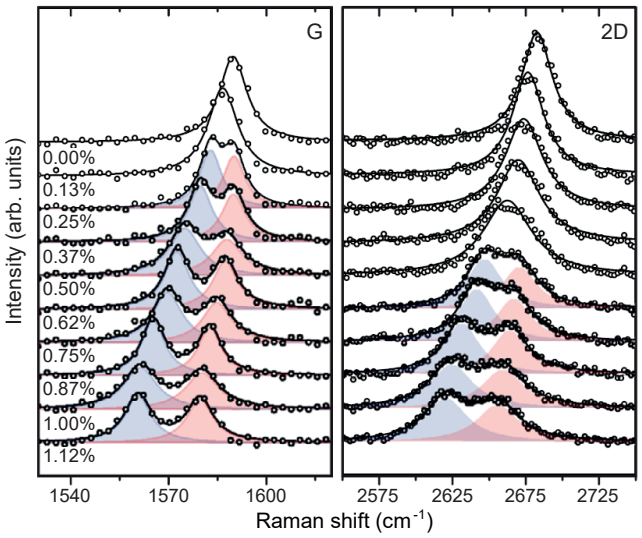

Figure 4.5 Uniaxial strain measurements of graphene with circular corotating polarization at 532 nm excitation wavelength. The strain increases from top to bottom. Figure adapted from Ref. [66]

Figure 4.5 shows the evolution of the Raman spectrum of the G (left) and 2D (right) mode under strain. The uniaxial strain increases from top to bottom and was induced with a two point setup.[66] For small strain only a shift of the respective mode is observed whereas at higher strain an additional splitting becomes visible. Both modes shift to lower wavenumbers with increasing expansive strain.

Doping in graphene also leads to a shift of the Raman modes. n-type doping results in an upshift of the G mode with increasing doping level. The 2D mode slightly increases in position for weak doping; for doping levels over approx. $2 \cdot 10^{13}$ cm^{-2} a strong downshift of the position is observed.[67] p-type doping shows a continuous upshift of either the G and 2D mode with increasing doping level.[67]

With a correlation analysis of the G and 2D mode position, introduced by Lee et al. one can disentangle the strain and doping components.[68] In the correlation plot the position of the 2D mode is plotted over the G mode. First the mean position of the G

and 2D mode is determined to eliminate the influence of shear strain.[66] The influence of hydrostatic strain and doping are separated by comparing the mean values of the two modes to a reference that accounts for the influence of doping. In the last step the shear strain is calculated from the splitting of the G mode.

4.2 Carbon nanotubes

Carbon nanotubes are the one-dimensional allotrope of carbon nanosystems. CNTs are built up of a rolled up sheet of graphene. They appear as single or multiwalled cylinders. I will only investigate single-walled carbon nanotubes (SWCNTs) in this work and therefore only discuss their properties.

CNTs are described by their chirality. The chiral vector $\mathbf{c}$ gives the directions in which the graphene sheet is rolled up. The chirality of the nanotube is defined by the two chiral indices (n_1, n_2) where $n_1 \geq n_2$.

$$\mathbf{c} = n_1\mathbf{a}_1 + n_1\mathbf{a}_2, \tag{4.9}$$

where $\mathbf{a}_1$ and $\mathbf{a}_2$ are the graphene lattice vectors. The diameter d of a specific chirality can be calculated from the chiral indices

$$d = \frac{|\mathbf{c}|}{\pi} = \frac{a_0\sqrt{n_1^2 + n_1n_2 + n_2^2})}{\pi}. \tag{4.10}$$

The chiral angle Θ describes the angle between $\mathbf{a}_1$ and $\mathbf{c}$ and can be calculated with

$$\cos(\Theta) = \frac{\mathbf{a}_1 \cdot \mathbf{c}}{|\mathbf{a}_1| \cdot |\mathbf{c}|} = \frac{n_1 + n_2/2}{\sqrt{n_1^2 + n_1n_2 + n_2^2}}. \tag{4.11}$$

All chiralities can be described by chiral angles between $0° \leq \Theta \leq 30°$. There are three different types of CNTs: zig-zag, armchair and chiral. In Fig. 4.6 (a) the graphene lattice is shown with an example of a chirality for the three different types. Zig-zag nanotubes have a chirality of $(n_1, 0)$. In armchair nanotubes both chiral indices have the same integer and chiral describes the infinite number of other possibilities to roll up the graphene sheet besides the two cases described above. Figure 4.6 (b) shows a zig-zag, armchair, and chiral tube.

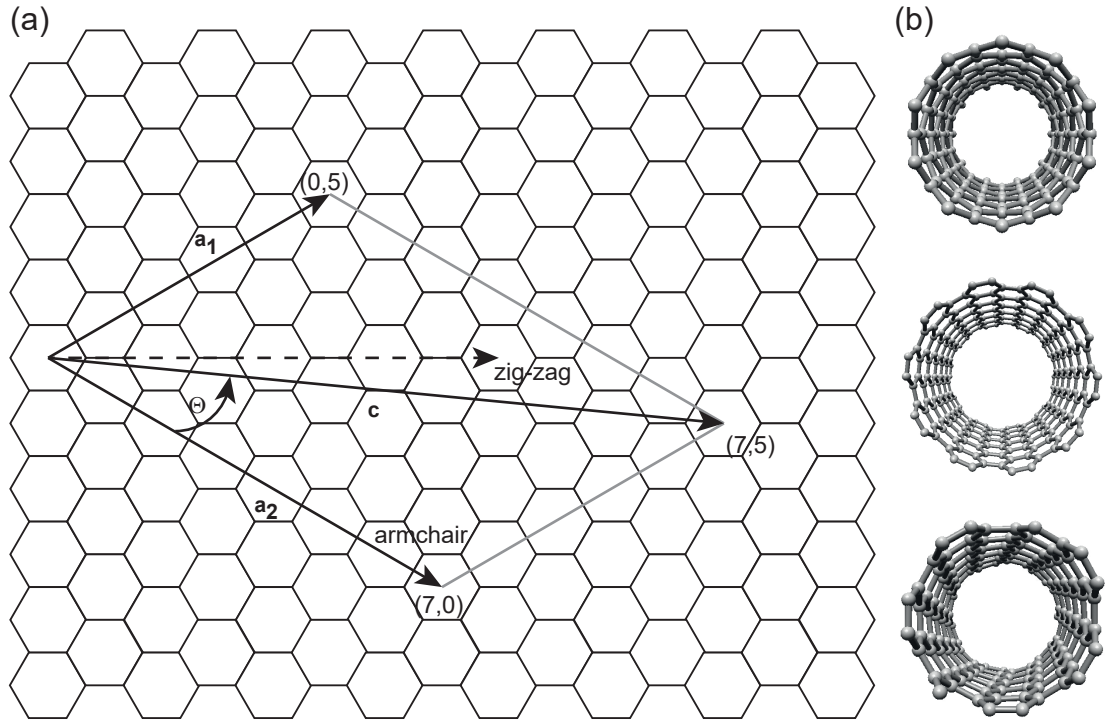

Figure 4.6 **(a)** Example of constructing the chirality of a (7,5) nanotube from the graphene lattice. The zig-zag and armchair direction are indicated. Adopted from Ref. [69]. **(b)** Example for a zig-zag (top), armchair (middle), and chiral tube (bottom).

CNTs exist in semiconducting and metallic form depending on their chirality. Two thirds of the CNTs are semiconducting and one third metallic.[30] Depending on the electronic type of the CNT, they can be used for different applications. In the last years great progress has been made in selecting and purifying single chiralities. In Chapt. 7 I will discuss the plasmonic enhancement of chirality enriched CNTs by a gold dimer. One possibility to enrich single chiralities of CNTs is described in the methods (see Chapt. 5).

With photoluminescence and resonant Raman measurements, it is possible to determine the chirality of a CNT by optical spectroscopy.[70;30] Imaging techniques with atomar resolution like transmission electron microscopy and scanning tunneling microscopy enable the identification of the chirality by the topography. In this work I mainly use Raman spectroscopy to investigate CNTs therefore I will introduce the Raman spectrum of CNTs in the next section.

Raman spectrum of CNTs

The Raman spectrum of CNTs shows similar modes as the spectrum of graphene. The D, G, and 2D modes are present in CNT Raman spectra as well. The spectrum exhibits an additional Raman mode, the so-called radial breathing mode (RBM). Figure 4.7 shows Raman spectra of an ensemble of various CNTs at two excitation wavelengths 532 nm (green) and 638 nm (red). The prominent Raman modes are labeled. At the different excitation energies the Raman spectra exhibit differences due to the different chiralities of nanotubes, especially in the region of the RBMs.

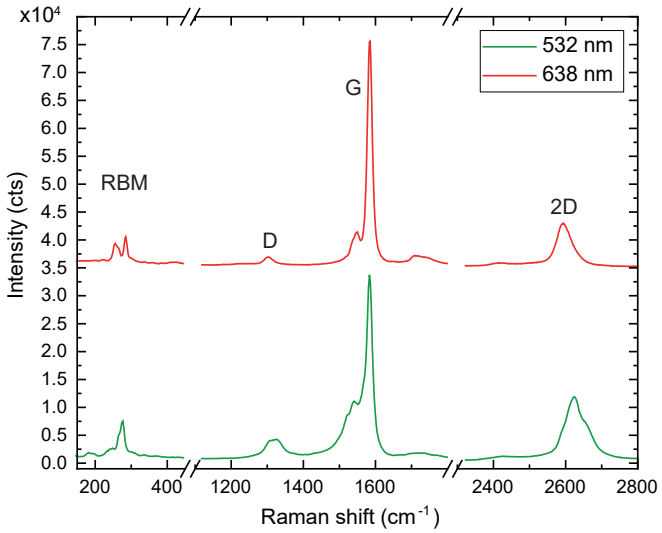

Figure 4.7 Raman spectrum of CNTs of different chiralities at two excitation wavelengths 532 nm (green) and 638 nm (red). The CNT Raman modes: RBM, D, G, and 2D are labeled.

The RBM corresponds to a radial motion of the carbon atoms. RBMs are connected to the diameter of the respective tube. The RBMs are observed in the spectral region between 100 and 400 cm^{-1}. In contrast to graphene, CNTs have intrinsic resonances that can be investigated by Raman spectroscopy. Each chirality can only be observed in a certain spectral range, called resonance window.[71] By applying resonance Raman spectroscopy it is possible to determine the transition energies of the different electronic transitions present in CNTs. H. Kataura proposed a plot where the transition energies of different chiralities are plotted over the RBM frequency or the diameter, see Fig. 4.8.[72] The diameter d is connected to the RBM frequency ω_{RBM} with

$$\omega_{RBM} = \frac{c_1}{d} + c_2, \tag{4.12}$$

where $c_1 = 220$ cm^{-1} and $c_2 = 20$ cm^{-1}.[30] Each point in the Kataura plot represents one chirality of CNTs. Different branches are observed in this representation each corresponding to a different transition number. The first transition of semiconducting nanotubes E_{11} has the lowest transition energy, followed by the second transition of semiconducting tubes E_{22} and the first transition of metallic tubes M_{11}. The Kataura plot is very insightful for identifying nanotube chiralities from a variety of different nanotubes. By knowing the RBM frequency and the resonance energy of the respective transition the chirality is clearly identified.[30]

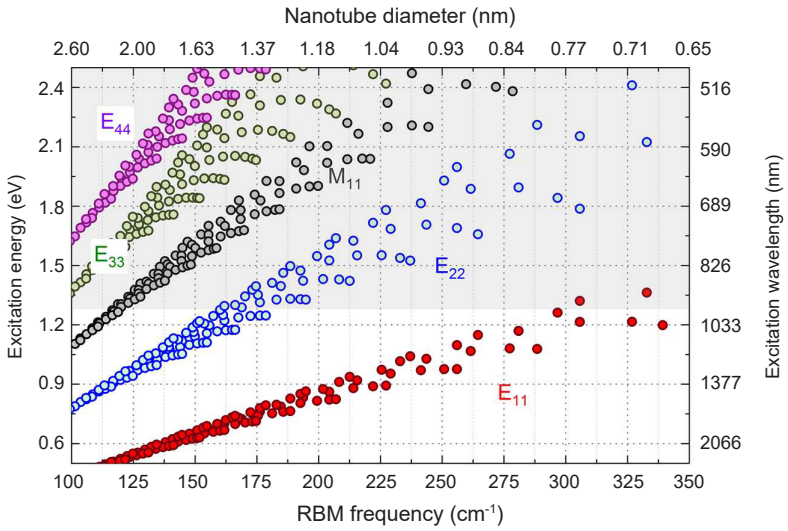

Figure 4.8 Kataura Plot. The excitation energy is plotted over the RBM frequency and the nanotube diameter respectively. The different transition numbers are labeled. Figure adapted from Ref. [73].

The G mode of a SWCNT consists typically of two Raman modes corresponding to a TO and LO phonon, often called G^- and G^+, where the TO is at lower energies than the LO in semiconducting CNTs. Compared to the G mode in graphene the TO will be shifted to lower wavenumbers whereas the LO is found just below 1600 cm^{-1} at higher wavenumbers. It describes a tangential movement of the carbon atoms in the direction of the nanotube axis in case of the TO and along the circumference for the LO. Their relative intensity depends on the chirality. Especially in metallic nanotubes the intensity of the TO changes drastically. In ensemble measurements of multiple chiralities the G mode will be the sum of all contributions of the different CNTs which can result in multiple peaks and an irregular shape, see in Fig. 4.7 (green).

The D and 2D mode have the same origin as in graphene. The D mode is defect

induced whereas the 2D mode is a two phonon process and does not need a defect for momentum conservation.

The polarization dependence of the Raman modes in CNTs is not comparable to the independent polarization behavior of the graphene Raman modes described above. It was shown experimentally that all CNT Raman modes show the same polarization behavior that follows $I_{CNT} = \cos^4(\Theta)$.[74] Highest Raman intensity is observed when the polarization is aligned with the CNT axis and zero intensity when the polarization is perpendicular. This effect is due to depolarization effects in single walled CNTs.[75] The high anisotropy of CNTs makes them absorb light only when polarized along the nanotube axis. Almost no absorption occurs when polarized perpendicular. From the depolarization effect results that only Raman modes with A_{1g} symmetry are observed because they give a contribution in their Raman tensor

$$A_{1g} = \begin{pmatrix} a & 0 & 0 \\ 0 & a & 0 \\ 0 & 0 & b \end{pmatrix}. \tag{4.13}$$

Similar depolarization effects were observed in other highly anisotropic materials like WS_2 nanowires as well.[76]

Endohedral functionalization of CNTs

Functionalization of CNTs is a tool to tailor different properties of the nanotubes. Different functionalization approaches exist. Endohedral and exohedral functionalizations attach the functional moieties inside or outside the nanotube. Figure 4.9 shows an overview over the different possibilites. Exohedral functional groups can be attached to defects (a) or covalently (b) and noncovalently (c,d) to the sidewall. Functionalization can be accomplished by attaching surfactants or wrapping polymers around the CNT circumference. Polymer wrapping is used in the process of chirality enrichment of CNTs, described in Chapt. 5.2. Covalent and noncovalent exohedral functionalizations influence the optical and electronic properties of the CNTs.[77;78] I will focus on the description of molecules functionalized inside the nanotube (e).

Three different mechanisms can be applied to insert the functional moiety inside the CNT: Sublimation, immersion and transport. Typical moieties inserted in nanotubes are metals, metalsalts or small molecules.[79] The incorporated molecules have to be smaller than the diameter of the CNT. Material that can be vaporized will be heated to the sublimation point and then adsorb on the nanotube sidewall. Over defect sides at the

end of the nanotube molecules get encapsulated in the nanotube if an activation barrier is overcome.

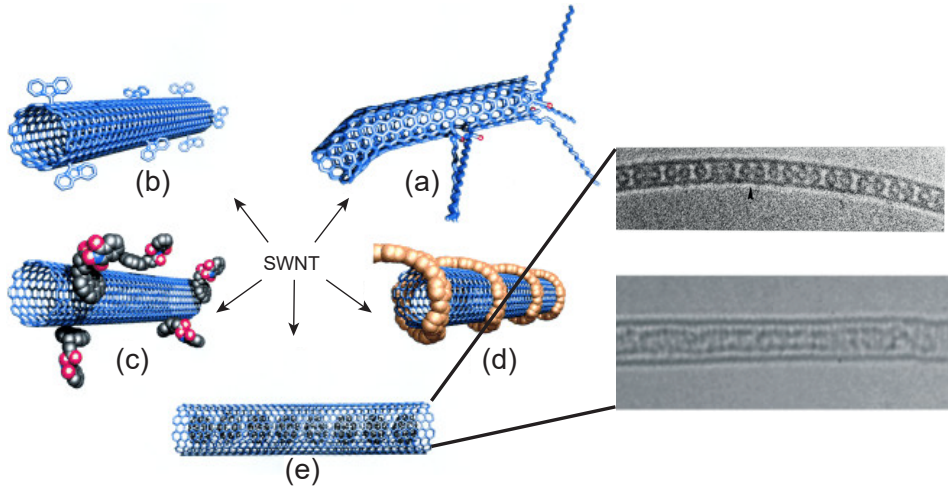

Figure 4.9 Different functionalization possibilities.[79] The insets show two TEM images: One of C_{60} fullerenes encapsulated in CNTs[80] and the other one of α-6T molecules incorporated in CNTs.[81]

Another possibility is to insert the CNTs in a material in liquid form. The tube will fill spontaneously due to capillary effects. If the desired functional moiety cannot be sublimated or melted it is possible to encapsulate it with the help of solvents. The CNTs and the functional molecule are diluted in a solvent. The functional moiety will then enter the CNT. It was impressively shown by incorporating C_{60} fullerenes inside of a CNT, called pea-pods.[80] Subsequently different organic molecules were encapsulated. The molecules are bound inside the tube by van der Waals forces. The encapsulated molecules form chains inside of the tube. For all filling processes it is necessary that the nanotubes have open end caps. They can for example be opened chemically. During the endohedral functionalization the functional moiety is inserted over defects at the end of the nanotube or in the sidewalls. The nanotube protects the encapsulated molecules from environmental influences.

5 | Methods

This chapter introduces the experimental setups and methods used to produce and investigate the different samples.

5.1 Electron beam lithography

Electron beam lithography (EBL) is a commonly used technique to build up metallic nanostructures on a substrate. In the process of writing structures by EBL several steps are necessary. Figure 5.1 shows a sketch of the EBL process.

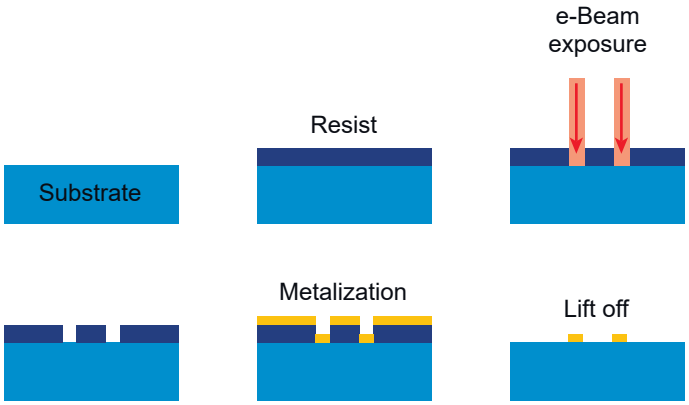

Figure 5.1 Steps within the EBL process.

First, a resist (PMMA) is deposited on the chosen substrate. Here, a silicon substrate is used with a 290 nm SiO_2 layer. Then, the nanostructure design is written by an electron beam. After developing the resist, metal is evaporated on the sample. First an adhesion layer of chromium (5 nm) is deposited followed by gold (45 nm for the graphene samples and 80 nm for the CNT samples). After a liftoff the desired nanostructures can be further prepared with the Raman reporter for SERS measurements. EBL has the advantage over colloidal particles that dimers or geometries of multiple nanoparticles can

be arranged by design and the size and separation of the particles is controllable. The quality of the written structures is confirmed by atomic force microscopy (AFM) and scanning electron microscopy (SEM).

5.2 CNT chirality enrichment

Carbon nanotubes appear in most cases in a large variety of chiralities. However, for various applications it is of great importance to use single chiralities of nanotubes instead of a mixture of different CNTs. Single chirality studies make use of the distinct properties of the chirality, for example the transition energy. Different techniques are used to achieve single chirality CNT samples: Selective growth[82–84], density gradient centrifugation of SWCNTs with surfactants[85;86], or gel filtration.[87–89] In this work I investigated (7,5) nanotubes enriched by Sephacryl gel filtration / size-exclusion chromatography performed by the group of Benjamin Flavel at the Karlsruhe Institute of Technology.

The raw material of CNTs (HiPco) are suspended in water with the surfactant SDS. The suspension was sonicated and centrifuged and removed from the precipitated CNT bundles in the end. The separation of the nanotubes is carried out in a glass column filled with Sephacryl gel filtration medium. After filling the medium the gel is compressed and the nanotube suspension added on top. SDS in water is then pushed through the column by compressed air. Applying more SDS in H_2O eluent removes bundles of CNTs as well as metallic nanotubes. By varying the pH of the eluent it is possible to separate the different chiralities of CNTs which can then be removed from the column. For a more detailed description of the separation method I refer to Ref. [88].

5.3 Dielectrophoretic deposition of CNTs

CNTs are mostly prepared in solution. To measure individual CNTs or use them in devices it is crucial to deposit them on a surface in a controllable way that is ideally scalable.[31] Dielectrophoretic deposition offers these requirements. It uses a pair of metal electrodes that will be gated with one (or multiple) CNT. Figure 5.2 (a) shows a schematic overview of the method. The CNTs are prepared in solution and dropcasted on the metal electrodes. These are contacted with an AC or DC current depending on the solvent in which the CNTs are desolved. The induced dipole moment in the CNT interacts with the electric field of the electrodes and moves along the field gradient towards the electrodes and bridges them.[90] After applying the voltage the leftover CNT solution is rinsed off and the sample is dried. Depending on the concentration of CNTs in the solution and the

applied electrical field it is possible to deposit individual CNTs between the electrodes or multiple ones, see Fig. 5.2 (b). Dielectrophoretic deposition has the advantage that it controls the orientation of the CNTs which is crucial in optical experiments.

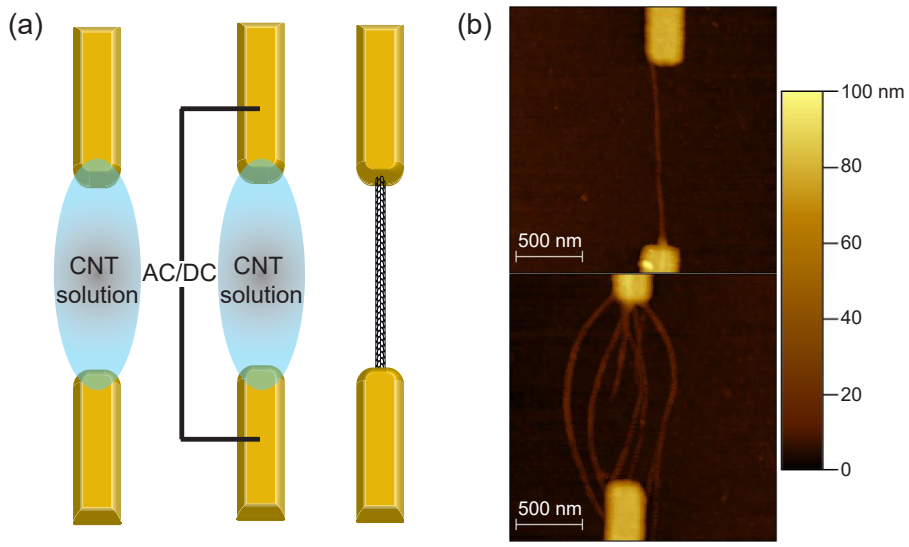

Figure 5.2 **(a)** Mechanism of dielectrophoretic deposition. **(b)** AFM topography images of different electrodes showing one (top) or multiple CNTs (bottom) connecting them.

5.4 CNT functionalization with α-6T molecules[1]

For the experiments described in Chapt. **??** α-6T molecules are encapsulated in CNTs, further named α-6T@CNT. Here, I will briefly describe the encapsulation process. Single walled CNTs with a mean diameter of 1.3 nm are purified and cut in piranha solution. The sexithiophene molecules were diluted in toluene and the CNTs added to them. The solution was refluxed at elevated temperatures overnight. Afterwards the solution was dispersed and filtered several times to remove free molecules. The filling process is described in more detail in Ref. [39]. α-6T molecules are rod-like and form a head-to-tail row inside of the nanotube aligned along the CNT axis as was confirmed by transmission electron microscopy.[40;81] If the diameter of the CNT is larger than 1.1 nm, two rows of molecules form inside of the CNT side-by-side. The interaction between the CNT and the encapsulated molecules is mediated by van der Waals forces.

[1]Parts of this section are taken from Wasserroth et al. *The Journal of Physical Chemistry C, 123(16)*:10578–10585, 2019. The encapsulation was performed by Etienne Gaufrès, Nathalie Y.-W. Tang, and Richard Martel.

5.5 Raman setups

Raman spectroscopy is the main tool I used to investigate the different samples. Raman setups are available in micro and macro configuration. As the names suggest they are used for bulk measurements (macro) or measurements of small volumes (micro). Since I investigate nanosystems I use the micro Raman configuration. A typical micro Raman setup consists of three different pieces: the excitation light source, the microscope, and the spectrometer with detector. Two different Raman setups were used in this work, the T64000 and the XploRA.

T64000

Figure 5.3 shows the T64000 Raman setup. It is suited to perform wavelength- and polarization-dependent measurements.

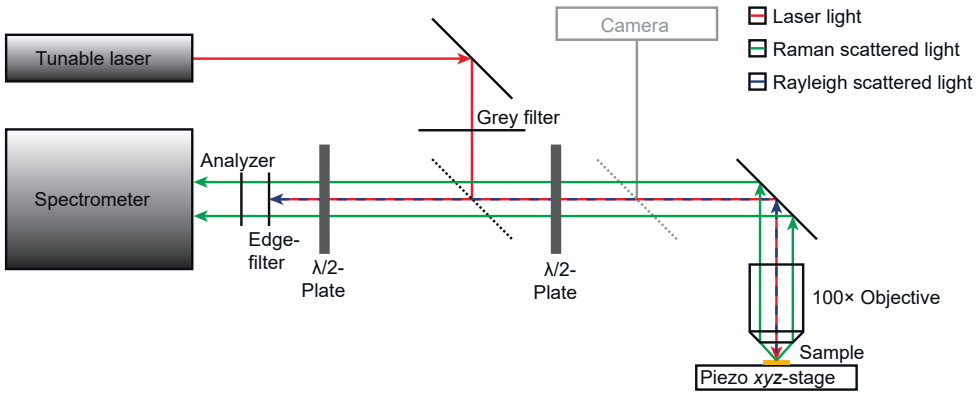

Figure 5.3 Raman setup with a tunable laser source for wavelength-dependent measurements. The $\lambda/2$ plates and the analyzer enable polarization-dependent measurements. The piezo stage is essential for measurements in the nano regime.

Tunable continuous wave lasers are used as excitation source. In the visible a dye laser (Radiant Dyes - Dye Ring) with different dyes for different excitation ranges is used: Rhodamin 6G for the wavelength range 560-615 nm, Sulforhodamin 580-630 nm, and DCM 630-670 nm. For the infrared a titanium sapphire laser (Coherent MBR-110) is used that is tunable in the range of 690-1010 nm. Some single lines are used from an Ar/Kr laser (Coherent Innova 70C Spectrum) in the visible range and a Nd:YAG laser (Coherent Compass 415M-200) for 532 nm.

The laser light is focused on the sample with an Olympus BX41 microscope. All measurements were performed with a 100× objective (NA=0.9). The Rayleigh scattered

light and the reflected laser beam are cut out with an appropriate long-pass edge filter. Grey filters are used to decrease the laser power on the sample. For the plasmonic samples, it is critical to use low power in the region of a few hundred microwatts. Otherwise the plasmonic system can be easily damaged or modified.

A piezo stage (PI E-710) is used for adjusting the laser focus on the desired position on the sample. I investigate various nanostructures, thus precise positioning is crucial. The optimal position is obtained by monitoring the Raman intensity of the mode under investigation and maximizing the intensity by varying the laser focus in steps of 100 nm in x-, y- and z-direction. For polarization-dependent measurements, two $\lambda/2$-plates are used to rotate the polarization of the incoming/outgoing light and an analyzer is placed directly in front of the spectrometer entrance slit.

To observe the signal, a Horiba Jobin-Yvon T64000 spectrometer is used. The T64000 is a triple grating spectrometer. It can be used in two different configurations: direct path mode and triple grating mode. In direct path mode the T64000 acts like a single grating spectrometer. The scattered light enters the entrance slit is dispersed by a single grating and focused on the detector. For measurement in direct path mode, a notch or band pass filter is necessary to cut out the elastically scattered light. In triple grating mode the light enters the spectrometer in a double monochromator setup. It is dispersed and the elastically scattered light is blocked at the intermediate slit. No additional filters are required in this configuration. It is particularly useful for resonant measurements of Raman modes with small Raman shift, like radial breathing modes of carbon nanotubes. Afterwards the light is dispersed in the same spectrometer path as in direct path mode and guided to the detector.

In wavelength-dependent measurements it is critical to calibrate the intensity of the measurements to account for changes in the sensitivity by the optical elements involved. Especially gratings and the detector have a strong wavelength dependence and would distort the results. To calibrate the intensity a Raman probe with a similar phonon energy is used that has a constant Raman scattering cross section in the measured energy range. In particular I will use free standing graphene, diamond, and CaF_2. I will indicate which calibration source was used in the respective chapters. The calibration is carried out by dividing the Raman intensity of the investigated mode by the Raman intensity of the calibration source. To compare Raman measurements at different excitation energies they need to be recorded over the same acquisition time and with the same power on the sample.

Laser spot size

To estimate the enhancement of the plasmonic system, it is necessary to know the focal size of the exciting laser. I spatially scanned over a small CNT bundle and assumed a Gaussian beam profile.

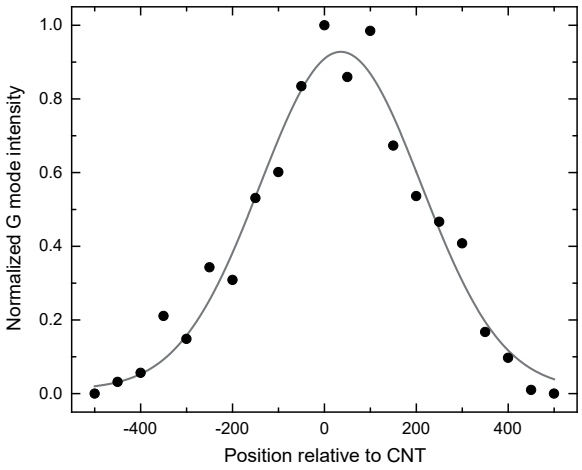

Figure 5.4 Line scan of the CNT G mode Raman intensity as a function of position to determine the laser spot size. The solid line is a Gaussian fit.

Figure 5.4 shows the CNT's G mode normalized intensity in dependence of the spatial position of the laser focus. The solid line is a Gaussian fit with a width of FWHM = 412 nm. The excitation wavelength is $\lambda_l = 600$ nm. The scan was performed in x- and y-direction with equal results to confirm the assumption of a Gaussian beam. The width of the excitation laser is dependent on the wavelength because of the dispersion of light.

XploRA

The XploRA is an integrated Raman microscope. In contrast to the T64000 described previously, the XploRA setup has three fixed wavelengths (532 nm, 638 nm, and 785 nm). All optical components are optimized for measurements in the visible wavelength region. A $\lambda/2$-plate and an analyzer enable horizontal and vertical polarization for the exciting light. The light is focused on the sample with a Olympus BX51 microscope. For the measurements a microscope objective with 100× (NA=0.9) magnification with an NA of 0.9 was used. The XploRA is equipped with a piezo stage (PI E-725) for focusing the laser beam and Raman mapping as well. Compared to the T64000 the XploRA has higher sensitivity but resonant Raman measurements are not possible.

5.6 Dark-field spectroscopy

A dark-field microscope is used to investigate the elastic scattering of plasmonic nanostructures. The dark-field spectrometer setup is depicted in Fig. 5.5.

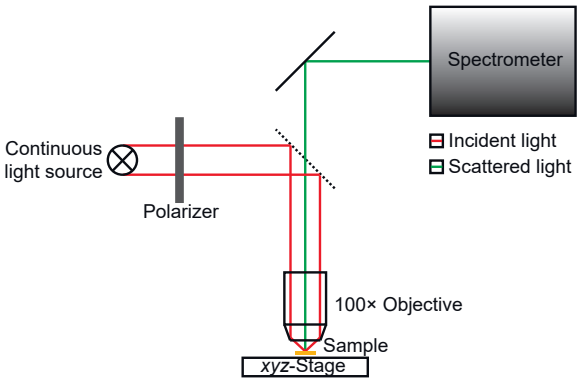

Figure 5.5 Polarization-dependent dark-field spectrometer setup.

A white light lamp (50 W) is used to excite the scattering process. A polarizer is used for polarization-dependent measurements. A microscope (Nikon Eclipse LV100) with a 100× dark-field objective serves to focus on the sample. Dark-field objectives illuminate the investigated sample from the side and the scattered light is collected in the middle of the objective. A fiber guides the scattered light to the spectrometer. By shining through the fiber from the opposite site the gathering area is determined in the microscope image. The scattered light is dispersed in a single-grating spectrometer (Horiba Scientific iHR320) and detected with a liquid nitrogen cooled silicon CCD.

Comparable to the calibration of the wavelength-dependent Raman measurements described above, the dark-field spectra have to be calibrated. In the dark-field spectrum the influence of the white light source has to be considered. The scattering spectrum of the dimer is measured with polarization along the dimer axis. The measured intensity I_{meas} is a convolution of the signal of the nanosystem, which consists of the response of the substrate $I_{substrate}$, the plasmon I_{dimer}, and the influence of the setup I_{spec}. The response of the setup consists of the different parts in the optical path, i.e. the lamp, the detector, the fiber, and the optical elements within the beam path. The response of the different components is obtained by measuring a white light standard. The background signal I_{bg} has to be included in the calculation, which is a convolution of the setup and the substrate ($I_{substrate}$) and measured on the substrate next to the dimer. The plasmon

dark-field spectrum is calibrated by

$$I_{dimer} = \frac{I_{meas} - I_{bg}}{I_{spec}}. \tag{5.1}$$

The acquired spectrum yields the LSPR of plasmonic nanostructures in the far field. In the dark-field scattering setup the entire sample is illuminated but only a small area of the scattered light is collected.

6 | Plasmonic enhancement of graphene[1]

In this chapter I will investigate the influence of a plasmonic near field on graphene. A monolayer of mechanically exfoliated graphene is suspended over a gold nanodimer. The graphene is strained into the interparticle gap and onto the substrate as was shown by Heeg et al.[27;28;66] I will make use of the constant Raman cross section of the G mode of graphene (see Chapt. 4.1) to investigate the plasmonic near field as a function of excitation energy. First, I will introduce the sample geometry. Then I will discuss the local strain and doping in the dimer gap determined by Raman scattering. Spatial Raman measurements will reveal the localization of the plasmonic hotspot. In the end of the chapter I will characterize the polarization and excitation energy dependence of the G and 2D mode of graphene measured in the plasmonic hotspot.

6.1 Experimental section

The sample consists of a field of plasmonic nanodimers that are built of two gold discs on a SiO_2/Si substrate with a 290 nm thick SiO_2 layer, sketch in Fig. 6.1 (a). Gold dimer structures were produced by electron beam lithography, see Chapt. 5.1 for an introduction of the lithography method. A variety of dimer structures with different diameters were exposed by electron-beam lithography in a LEO 1530 Gemini FEG SEM and Raith Elphy Plus Lithography System with laser interferometer stage. 5 nm Cr

[1]Parts of this chapter were published as *Graphene as a local probe to investigate near-field properties of plasmonic nanostructures* in Wasserroth et al. *Physical Review B, 97(15)*:73, 2018, https://doi.org/10.1103/PhysRevB.97.155417. The project was conceived and planned by S. Reich, S. Heeg, and me. The gold dimers were fabricated by R. Gorbachev. The graphene preparation and transfer was carried out by N. Clark and F. Schedin. The wavelength-dependent Raman measurements were performed by T. Bisswanger as part of his Master thesis under my supervision with support by P. Kusch. The remaining measurements were performed by myself. N. S. Mueller and S. Heeg provided support with the HORa theory. I interpreted the data and wrote the manuscript. All authors commented on the manuscript.

and 45 nm Au were evaporated followed by a lift off in an ultrasonic bath. The spatial properties of the system were imaged by SEM (Zeiss ULTRA 55 with 10 kV acceleration voltage), see Fig. 6.1 (b). A statistical evaluation of the SEM images of the investigated dimers yielded diameters between $100 - 110$ nm and a gap of $20 - 30$ nm.

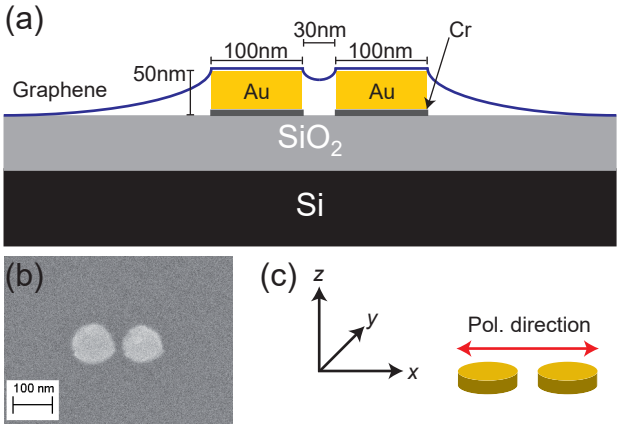

Figure 6.1 **(a)** Sketch of the sample consisting of two gold discs covered by graphene on a SiO_2/Si substrate. The dimensions are indicated. **(b)** SEM image of a gold nanodisc dimer. **(c)** Coordinate system used throughout the chapter. The polarization direction of the incident light was chosen along the dimer axis if not explicitly stated otherwise.

A large flake of graphene was placed over the dimer field covering multiple dimers. The graphene flake was prepared on a p-doped SiO_2/Si substrate with a 90 nm oxide layer by micromechanical cleavage.[91] The flake was precisely transferred on top of the plasmonic structures. For the transfer the graphene was coated with a polymer supporting the so-called "wet" transfer.[92] By optical microscopy and Raman spectroscopy it was confirmed that monolayer graphene is covering the region of the investigated plasmonic dimers.[51] The topography was measured by AFM using a Park Systems XE-150 in non-contact mode.

To access the near-field properties of the plasmonic system I measured the enhancement of the Raman modes of graphene as a function of excitation energy. The Raman spectra were recorded with a Horiba T64000 spectrometer, as described in Chapt. 5.5, in backscattering configuration at room temperature. The positioning of the laser on the plasmonic hotspot is crucial, as small changes lead to a dramatic decrease or increase in intensity. To get maximum enhancement and comparable results in the excitation energy dependent measurements the laser focus was centered on the dimer with a piezo stage (PI E-710, step size 100 nm) for every measurement. The polarization of the laser was chosen to be parallel to the dimer axis unless specified otherwise, see Fig. 6.1 (c). The laser power

on the sample was kept constant at 300 µW. Calibration spectra of free-standing graphene were recorded for every wavelength to account for changes in the optical response of the setup. The enhanced intensity of the graphene modes in the excitation energy dependent measurements (see Chapt. 6.6) was divided by the intensity of the G and 2D mode of the calibration spectra of suspended graphene. Additionally, reference spectra of graphene were recorded on the substrate (without plasmonic nanostructure) 2 μm beside the dimer for every wavelength. The intensity of the Raman modes in the reference spectra was subtracted from the enhanced measurements to remove interference effects between the substrate and graphene ensuring that I investigate the plasmonic enhanced intensity.[63]

In Chapt. 6.7 additional excitation energy dependent results of three dimers are presented that have the same dimensions as described above. As calibration sources free standing graphene, diamond, and the graphene on the substrate beside the dimer are used, as indicated in the respective figure.

The far-field resonance of the dimers was investigated by dark-field spectroscopy. The dark-field setup is described in Chapt. 5.6.

6.2 Raman spectrum of graphene in the gold dimer gap

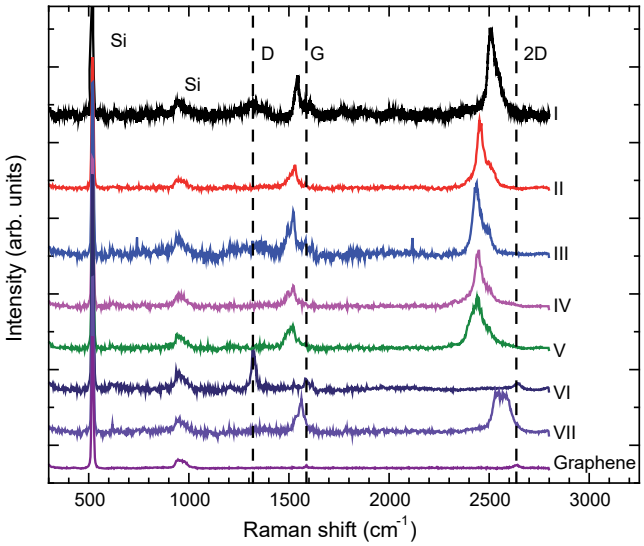

Figure 6.2 Raman spectra of seven different dimers (I-VII) showing plasmonic enhancement of the graphene G and 2D mode. It is compared to the bare graphene spectrum (purple). The silicon modes of the substrate are also observed. Spectra recorded at 633 nm and offset for clarity.

I investigated the plasmon-enhanced Raman modes of graphene that is suspended on

different dimers. Figure 6.2 shows that the transfer of graphene on top of the plasmonic nanodimers yields a reproducible plasmonic enhancement at 633 nm excitation wavelength for most of dimers.

Dimer VI shows no enhancement of the G and 2D mode but a strong D mode is present; the graphene on top of this dimer is torn in the gap yielding no enhancement but defects. First I discuss Dimer I in Fig. 6.2 and characterize it in detail later I will discuss wavelength dependent Raman measurements of three more dimers.

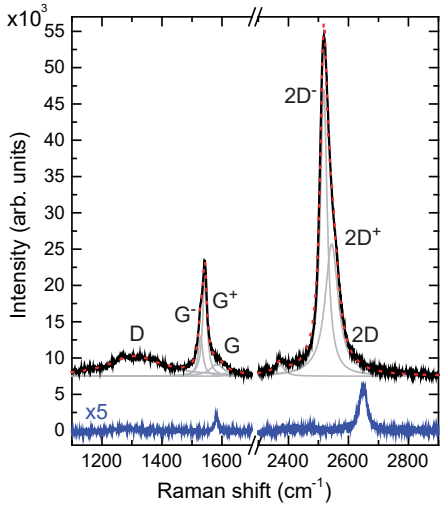

Figure 6.3 Plasmon-enhanced Raman spectrum (black) when focusing on the nanodimer and a reference spectrum collected on the substrate (blue). The fitted peaks are shown in grey and the prominent Raman modes of graphene are labeled. Excitation wavelength $\lambda_l = 605$ nm. Spectra offset for clarity.

In Fig. 6.3 I show an exemplary plasmon-enhanced Raman spectrum of graphene in greater detail. One spectrum was recorded at 605 nm excitation wavelength when focusing on Dimer I of Fig. 6.2 (black line in Fig. 6.3) and a reference spectrum was recorded next to the dimer on the substrate (blue). I labeled the prominent D, G and 2D modes in graphene and their strain components G^+, G^-, $2D^+$, and $2D^-$.[51;93] The reference spectrum shows only the unstrained G and 2D modes. I observe an increase in the integrated scattering intensity by a factor of 90 for the G and 55 for the 2D mode. The enhanced spectrum in Fig. 6.3 shows a shift and splitting of the G and the 2D modes with respect to the modes of the reference spectrum, which indicates that hydrostatic and shear strain as well as doping are present in the graphene sample (see Chapt. 6.3).[66] In addition to the enhanced and shifted modes the unstrained G and 2D peaks remain present as shoulders in the plasmon-enhanced Raman spectrum. These features originate

from the graphene surrounding the dimer because the laser focus (diameter 410 nm) is much larger than the size of the plasmonic hotspot located in the gap of 30 nm size. The presence of the defect modes in the plasmonic enhanced Raman spectra will be discussed in Chapt. 6.8.

6.3 Local strain and doping

The plasmonic enhancement of the graphene Raman modes allows to detect local properties of graphene in the hotspot with nanoscale resolution.[27] First I evaluate the strain configuration and doping level for the graphene suspended over the gold nanodimer. Tensile hydrostatic strain leads to a shift of the G and 2D mode to lower wavenumbers. Shear strain induces a splitting of both modes, see Chapt. 4.1.[93] Doping results in a shift of the G and 2D mode as well, due to the singular electron-phonon interaction for electrons at the Fermi surface (Kohn anomaly).[94] Depending on the type of doping the modes shift to higher or lower wavenumbers. For graphene in contact with gold nanoparticles n-type doping is characteristic.[95;96] It yields an upshift of the G mode frequency, while the 2D line is almost constant in frequency for small doping levels followed by a down shift at higher doping.[67]

The strain and doping level were determined with the correlation analysis of the G and 2D mode for arbitrary strain configurations.[66] For each Raman mode, I calculate the mean value of the two strain components $\overline{\omega_{\mathtt{G}}} = 1534$ cm^{-1} and $\overline{\omega_{\mathtt{2D}}} = 2512$ cm^{-1} and obtain a hydrostatic strain of 2.1%. This caused a 59 cm^{-1} frequency shift of the G line. The shear strain amounts to 1.1% calculated from the G^+ and G^- splitting of 7 cm^{-1}. I find an n-type doping level of 10^{13} cm^{-2} corresponding to a shift of the G mode by 10 cm^{-1}. These values report the local strain and doping of the graphene in the dimer gap. According to the calculated near-field distribution of a dimer, see Chapt. 2, the strongest plasmonic enhancement emerges in the dimer gap leading to the conclusion that the SERS signal is dominated by contributions from the hotspot. The relative Raman intensities of the G^+ and G^- components allow evaluating the lattice orientation of the graphene flake with respect to the dimer axis. The zig-zag direction in the lattice of the graphene flake that covers the dimer is tilted by an angle of 9° towards the dimer axis.

AFM measurements show the expected topography of graphene for local strain inside the dimer gap and around the dimer.

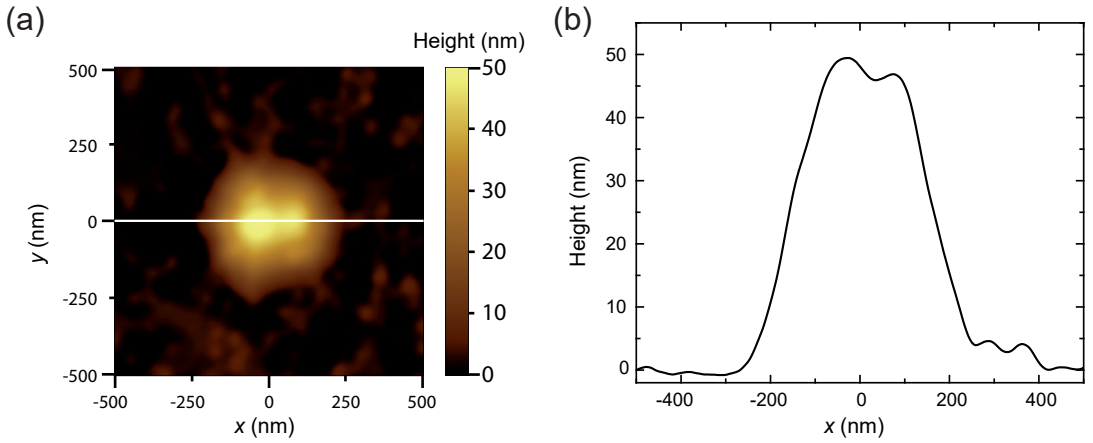

Figure 6.4 **(a)** AFM topography image of the investigated dimer. **(b)** Height profile of the dimer at the position indicated by the grey horizontal line in **(a)**.

The AFM topography image in Fig. 6.4 (a) clearly shows the two gold discs and the graphene extending over the dimer. The graphene is pulled down towards the substrate due to adhesion forces straining the graphene in the gap between the discs, as can be seen in the height profile through the dimer center in Fig. 6.4 (b). A detailed discussion of the strain configuration can be found in Refs. [27;28;66].

6.4 Localization of the near-field enhancement

Plasmonic near fields localize light to length scales on the order of 10 nm.[97] The near fields are challenging to visualize, because most measurements operate with far-field detection techniques. The typical laser spot sizes in a Raman experiment are several hundred nanometers in diameter. A combined scattering near field optical microscope (SNOM) and Raman setup was introduced that measured a SERS hotspot of 75 nm in diameter (lateral size perpendicular to dimer axis) for gold dimers similar to the ones studied here.[25] As an alternative approach, I obtain an upper limit for the SERS hotspot by spatially mapping the Raman response of graphene on the dimer in real space.

I scanned an area of 1 μm^2 around the dimer taking Raman spectra every 100 nm. The normalized G mode intensity is plotted in Fig. 6.5 (a) as a function of (x,y) position where the dimer is indicated by black circles. This Raman intensity map highlights the localization and spherical shape of the SERS hotspot. Already a shift of 100 nm results in a decrease in signal intensity of about 10%, 200 nm from the center the intensity dropped to 50%. In Fig. 6.5 (b) I plot the intensity of the G line through the center across the x-

and y- direction. With Gaussian fits I find a FWHM of 440 ± 20 nm in both directions. The behavior reflects a convolution of a localized scatterer with a much more extended laser focus. The laser spot has a FWHM of 410 ± 30 nm, see Chapt. 5.5. Comparing the width of the Raman map [see Fig. 6.5 (b)] and the diameter of the laser spot I get a width of 160 ± 95 nm for the plasmonic hotspot. The width resembles the size of the dimer system. This appears reasonable, because the SERS response accessed by us is dominated by the far-field excitation and detection of the nanodimer. The SNOM-based approach directly excites and detects the near field of the nanodimer resulting in the nominally smaller spot size.

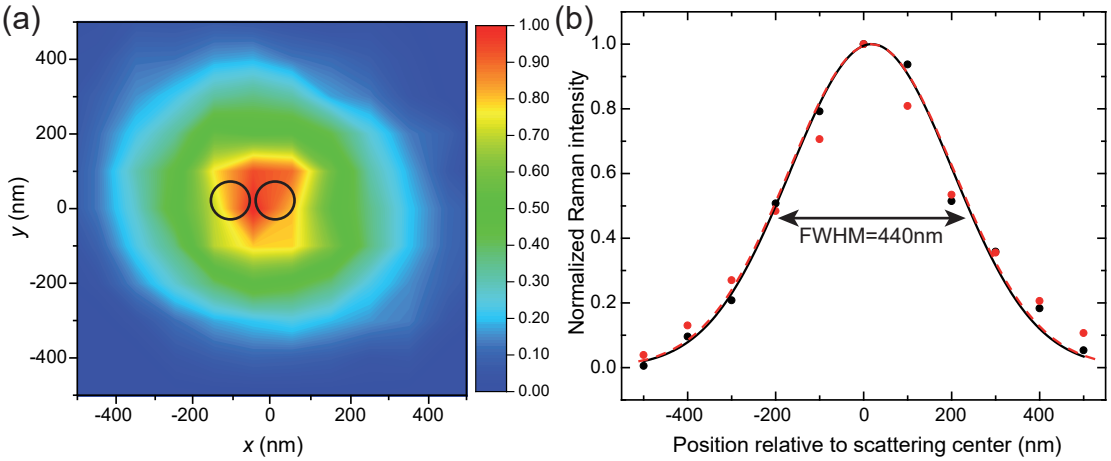

Figure 6.5 **(a)** Raman intensity map of the G mode recorded for 602 nm excitation wavelength. The dimer is indicated by two black circles. **(b)** Intensity measured along the x-direction at $y = 0$ (black dots) and along the y-direction at $x = 0$ (red dots). The lines are the corresponding fits with a Gaussian intensity profile. The extracted FWHM is 440 ± 20 nm.

The localization of the enhanced signal is also evident in z-dependent scans when focusing on the dimer along the z-axis, as shown in Fig. 6.6. Each data point represents the Raman intensity of the 2D mode as a function of the distance between laser focus and probe. The black dots show the normalized signal when focusing on graphene coupled to the dimer whereas the red dots represent the normalized Raman intensity of graphene on the silicon substrate. The trend of both measurements differs strongly. The intensity of the graphene signal on the substrate decreases slowly, whereas the z-dependence of the Raman signal on the dimer shows a trend that is expected for a localized scatterer.

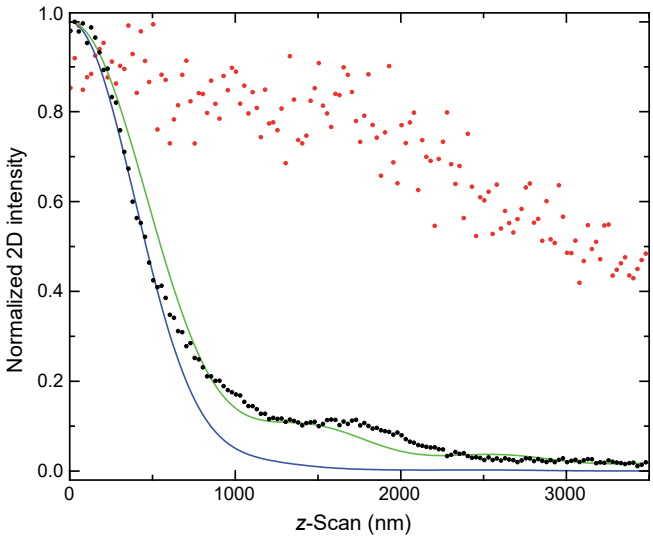

Figure 6.6 z-Dependency of the 2D mode intensity of graphene with the laser centered on the dimer (black dots) and on the substrate (red dots). The z-scan was recorded at 605 nm laser wavelength. The solid lines are the calculated detector signal of a point like scattering center using geometrical optics and assuming confocal detection (blue) or non-confocal detection (green) using Eq. (6.1) and (6.2).

The experimental intensities on the dimer should correspond to the point-spread function s in the image plane of the detector which is calculated with geometric optics.[97] I calculate the point-spread function of a point like scattering center that is illuminated by a Gaussian laser beam at 605 nm excitation wavelength focused through a 100× objective with numerical aperture NA=0.9. The signal for confocal microscopes (blue line) including both the incident and detecting pathway is defined as $s_{confocal} \propto \left| I_{00}(\omega_l)\tilde{I}_{00}(\omega_l + \omega_{pn2D}) \right|^2$, where ω_l is the laser energy and $\omega_{pn2D} = 0.3$ eV the phonon energy of the measured 2D mode. I_{00} describes the excitation path, see Eq. (6.1), whereas $\tilde{I}_{00}$ describes the detection, Eq. (6.2). For non-confocal microscopes (green line) the point spread function is $s_{non-confocal} \propto |I_{00}(\omega_l)|^2$.

$$I_{00} \propto \int_0^{\Theta_{Max}} f_w(\Theta)(\cos\Theta)^{1/2} \sin\Theta(1+\cos\Theta) e^{ik_l z\cos\Theta} d\Theta \tag{6.1}$$

$$\tilde{I}_{00} \propto \int_0^{\Theta_{Max}} (\cos\Theta)^{1/2} \sin\Theta(1+\cos\Theta) e^{ik_{l+pn} z\cos\Theta} d\Theta, \tag{6.2}$$

with $\Theta_{Max} = \arcsin(\mathrm{NA})$ is the maximum collection angle of the objective. $f_w = \exp(-1/f_0^2 \mathrm{NA}^2)\sin^2\Theta$, where $f_0 = 0.8$ is the filling factor of the back aperture of the microscope objective. k is defined as $k = 2\pi/\lambda$, for incident light k_l and scattered light

k_{l+pn}. The point-spread function was normalized to displacement along $z = 0$. The confocal calculation (blue line) resembles very well the measured data until $z = 500$ nm. The non-confocal calculation, in contrast, fits better the second maximum at around $z \approx 1700$ nm. I conclude that the experimental data represent a combination of confocal detection at closer distances z and non-confocal detection, when the focus is more distant from the scattering center. I attribute further differences to the simplified model used in the calculation. From the z-dependent measurement and the comparison of the laser focus and the Raman map I conclude that the localization is in the order of the size of the plasmonic system.

6.5 Polarization dependence of the near-field enhancement

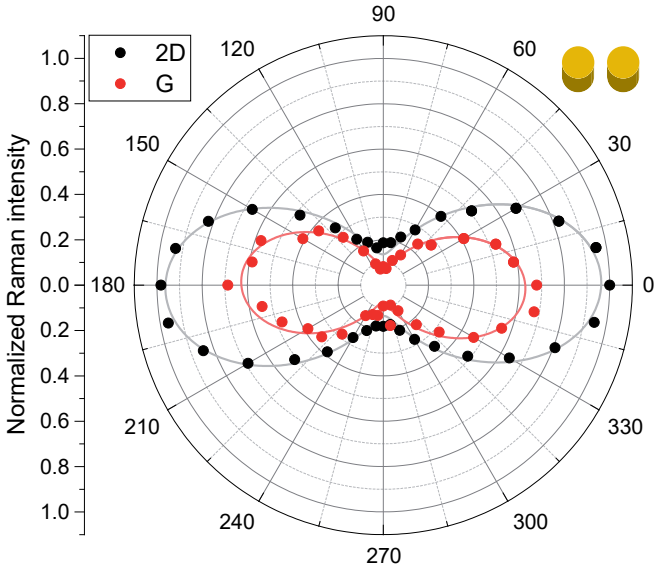

Figure 6.7 Polarization-dependent measurements of the G (red) and 2D (black) mode at an excitation wavelength of $\lambda_l = 602$ nm when the laser is centered on the plasmonic dimer covered with graphene. The dimer is oriented along the $0° - 180°$ axis as indicated in the inset. The solid lines represent the fits according to Eq. (6.3).

The Raman intensity of graphene coupled to the plasmonic dimer shows a strong polarization dependence. This was originally demonstrated for two perpendicular polarizations as a proof of the plasmonic enhancement in the dimer-graphene system.[27] Due to the specific design of the canonical SERS system I can switch the plasmonic coupling of the dimer by rotating the incoming polarization, see Chapt. 2. In Fig. 6.7 I show polarization-dependent measurements of the G and 2D mode. A strong enhancement is

observed when the incoming and outgoing polarizations are parallel to the dimer axis. If the polarization is perpendicular to the dimer axis, the Raman intensity decreases by a factor of 10 for the G mode and 6 for the 2D mode. In perpendicular polarization the particles are decoupled and act as single particles yielding weaker enhancement.[27]

As discussed in Chapt. 4.1, the Raman intensity of the G and 2D mode is independent of the polarization of the exciting light. In case of the plasmonic enhanced system the difference in the polarization-dependent measurements is explained by the strong anisotropy of the plasmonic near field of the dimer. To describe the experimental results it is sufficient to consider the system to be two dimensional, because of the nature of graphene, giving a Raman tensor $R = \left(\begin{smallmatrix} a & 0 \\ 0 & b \end{smallmatrix}\right)$. Due to the local near-field configuration of the dimer the components in the x- and y- direction have to be considered. From the Raman tensor I calculate the Raman intensity as function of polarization angle

$$I(\Theta) = [a \sin^2(\Theta) + b \cos^2(\Theta)]^2, \tag{6.3}$$

which is used to fit the experimental data in Fig. 6.7 with $a_G = 0.79$ and $b_G = 0.28$ for the G mode and $a_{2D} = 0.98$ and $b_{2D} = 0.37$ for the 2D mode, yielding a similar ratio a/b for both the G and 2D mode. This is reasonable, because the scattering intensity is dominated by the properties of the nanodimer, which is identical for both modes.

6.6 Excitation-energy dependence

To investigate and identify the position and width of the plasmonic resonance I measured both graphene Raman modes as a function of excitation energy in the near field and a dark-field spectrum in the far field. Since pristine graphene has a constant Raman cross section in the visible and near-infrared energy range (see Chapt. 4.1), changes in the Raman intensity as a function of excitation energy are attributed to the plasmonic near field. The experiment directly probes the near-field enhancement of the plasmonic system. Figure 6.8 shows the enhanced Raman spectra at 488 nm (blue), 605 nm (black), and 665 nm (red), normalized by free-standing graphene (see Chapt. 6.1). In the spectrum at 605 nm a strong enhancement and strain of the graphene modes is observed as discussed above. At 488 nm and 665 nm the enhancement decreased; the D mode is no longer observed.

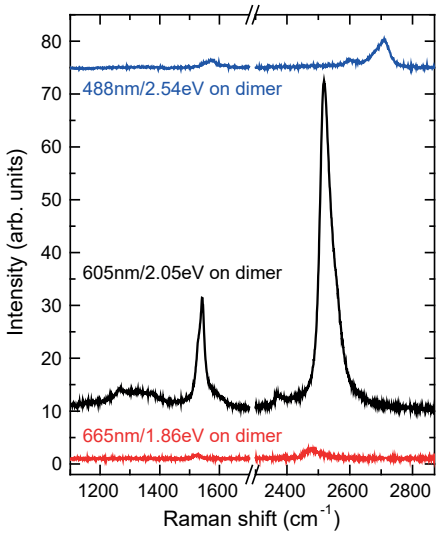

Figure 6.8 Spectra of the G and 2D mode on the dimer at different wavelengths: 488 nm (blue), 605 nm (black), and 665 nm (red). Spectra offset for clarity.

In the following I present the energy dependence of the near-field enhancement at the plasmonic hotspot. The near-field enhancement was measured at 30 different excitation wavelengths. It is shown in Fig. 6.9 for the G (a) and 2D mode (b). Each point represents the integrated area of all enhanced components of both modes. The intensity of the energy dependent measurements were normalized to the G or 2D mode of free standing graphene directly giving access to the local near-field enhancement as described in Chapt. 6.1. There is a clear maximum in enhancement visible at approximately 2.05 eV for both the G and 2D mode. Almost no enhancement is observed at green excitation (532 nm/2.33 eV).

To quantify the energy of the plasmonic resonance from the Raman data I adopt the HORa description of plasmon-enhanced Raman scattering, see Chapt. 2.[21] It gives the following expression for the enhancement factor $Enh(\omega_l)$ that I use to fit to the experimental enhancement of the G and 2D mode in Fig. 6.9

$$Enh(\omega_l) = \left[\frac{M^2}{(\hbar\omega_l - \hbar\omega_{pl} - \hbar\omega_{pn} - i\gamma_{pl})(\hbar\omega_l - \hbar\omega_{pl} - i\gamma_{pl})} + \frac{M}{\hbar\omega_l - \hbar\omega_{pl} - \hbar\omega_{pn} - i\gamma_{pl}} + \frac{M}{\hbar\omega_l - \hbar\omega_{pl} - i\gamma_{pl}} + 1\right]^2, \tag{6.4}$$

where M is a combined matrix element. The matrix element describes the coupling between the plasmon and the Raman probe.[21] ω_l and ω_{pl} are the laser and plasmon frequency, and ω_{pn} the phonon frequency. I use $\omega_{pnG} = 0.19$ eV for the strained G mode

and $\omega_{pn2D} \approx 0.3$ eV for the dispersive 2D mode. $\gamma_{pl} = \hbar/\tau_{pl}$ is the inverse plasmon lifetime τ_{pl} taken to be 0.15 eV which is a common width for a plasmonic system of the dimensions used in this work. Equation (6.4) describes the interference of four scattering pathways, similar to resonant Raman scattering incorporating the plasmonic coupling. The first term yields the scattering amplitude where the incoming and scattered light interact with the plasmon. The second and third term give the scattering amplitude when either incoming or scattered light interact with the plasmon. The last contribution is given by the standard Raman scattering where no interaction with the plasmon occurs. Since I calculate the enhancement and calibrated on suspended graphene this contribution only gives a constant.[21]

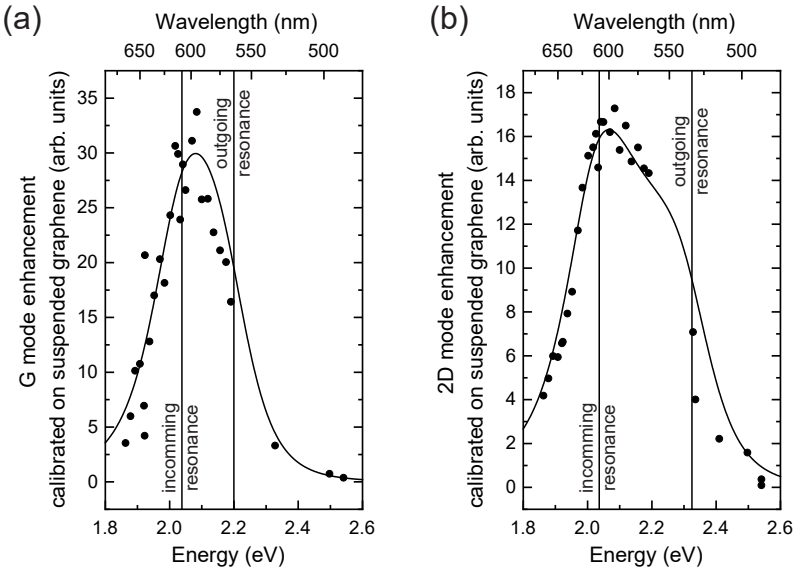

Figure 6.9 Energy dependent measurements of the G **(a)** and 2D **(b)** mode. The solid lines show the fit with HORa theory by Eq. (6.4). The vertical lines indicate the positions of the incoming and outgoing resonances. The Raman intensity of the G and 2D mode is normalized by suspended graphene as described in the experimental section.

The fit of the Raman resonance profile yields a plasmon energy of $\omega_{pl} = 2.01$ eV. The excitation energy for maximum enhancement does not correspond to the incoming resonance since the overlap of incoming and outgoing resonance shifts the maximum to higher energies.[4] The predicted enhancement profile of the 2D mode in Fig. 6.9 (b) was obtained from Eq. (6.4) using the parameters of the G mode fit, but different coupling parameter M. I obtain good agreement with the experimental data demonstrating the applicability of the HORa approach. The difference in enhancement for the G and 2D mode is attributed to the different scattering processes of the modes.[98] The energies of the

incoming resonances in Fig. 6.9 are determined by the local near-field resonance, therefore they are identical for the G and 2D mode. The outgoing resonance, in contrast, originates from the inelastically-scattered light and depends on the phonon energy. The asymmetry of the resonance profiles in Fig. 6.9 results from quantum interference between different scattering processes, which is determined by the sign and magnitude of the combined matrix element M. A stronger coupling (described by the M) implies a smaller ratio between incoming and outgoing resonance approaching unity if the first term in Eq. (6.4) dominates.[21] Unfortunately I was not able to measure the outgoing resonance of the G or 2D mode in greater detail due to a lack of tunable laser excitation in the energy range. I stress once more that the observed resonances originate from the localized near-field enhancement and not from intrinsic resonances of the Raman probe, since graphene has a constant Raman cross section. This emphasizes the suitability of graphene as a probe to investigate the local near field in plasmonic systems.

The Raman measurements are sensitive to the near-field resonance of the plasmonic system. The far-field response, in contrast, is measured by polarized dark-field spectroscopy. To characterize the plasmon response I obtained a dark-field spectrum of the dimer with the incoming light polarized parallel to the dimer axis, Fig. 6.10. The dark-field spectrum has a maximum at 2.18 eV and a FWHM of 0.33 eV.

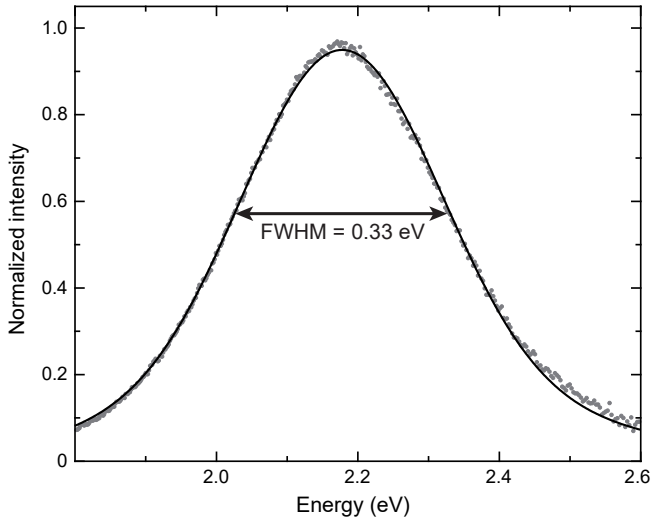

Figure 6.10 Normalized dark-field scattering spectrum of the gold dimer with polarization parallel to the dimer axis. The solid line shows a Gaussian fit of the experimental data (grey points).

The maximum of the experimental SERS enhancement occurs at lower energies than the maximum in the dark-field spectrum by 0.17 eV. Differences between elastic scattering

(dark-field spectrum) and SERS enhancement are frequently observed in SERS.[99] They are often attributed to (i) an energy difference between the far-field and near-field resonance and (ii) a distribution in size and shape of plasmonic hotspots in colloidal samples that differs for elastic and inelastic plasmon-enhanced scattering.[100] Since the system contains only a single plasmonic hotspot, explanation (ii) does not apply. I now examine explanation (i): Plasmon-enhanced Raman scattering yielded a near-field resonance of $\omega_{pl} = 2.01 \pm 0.02$ eV, Fig. 6.9, whereas the far-field resonance occurred at 2.18 ± 0.01 eV. Following Ref. [99] I calculated an expected shift between far- and near field 0.04 eV using the model of a damped oscillator and the geometry of the nanodimer. The predicted shift is much smaller than measured experimentally (0.17 eV). I could not identify the origin of this surprisingly large shift, which will be investigated in more detail in the future. One contribution may arise from the substrate and the varying dielectric environment or the strongly damping adhesion layer between the substrate and the gold.

6.7 Narrow plasmonic near-field resonances

After the extensive characterization of the influence of the plasmonic near field to graphene on *Dimer I* I will present the excitation energy dependence for three more dimers in the near and far field that show additional results in the excitation energy dependence. As shown in Fig. 6.2 the enhancement of graphene in the dimer gap is very reproducible.

In Fig. 6.11 wavelength-dependent Raman measurements are compared with the respective dark-field spectra. *Dimer a* and *Dimer b* have the same properties whereas the substrate of *Dimer c* was etched changing the dielectric environment of the dimer.

The wavelength-dependent measurements show the G and 2D enhancement. *Dimer a* and *c* were calibrated on suspended graphene. The G mode of *Dimer b* was calibrated on diamond and the 2D mode on graphene on SiO_2. Because of the different calibration sources it is difficult to compare the enhancement of the different dimers but the position and width of the plasmonic resonances may very well be compared. In the wavelength profiles distinct resonances were observed for all three dimers in contrast to the measurements discussed above. The position of the incoming resonances of the G and 2D mode are at the same energy. For *Dimer a* and *b* it was possible to measure the outgoing resonance of the G mode as well. The outgoing resonances of the 2D mode of all dimers and of the G mode of *Dimer c* were outside of the wavelength range of the excitation laser (see Chapt. 5). Sharp resonances are superimposed on a broad background fitted by a Gaussian.

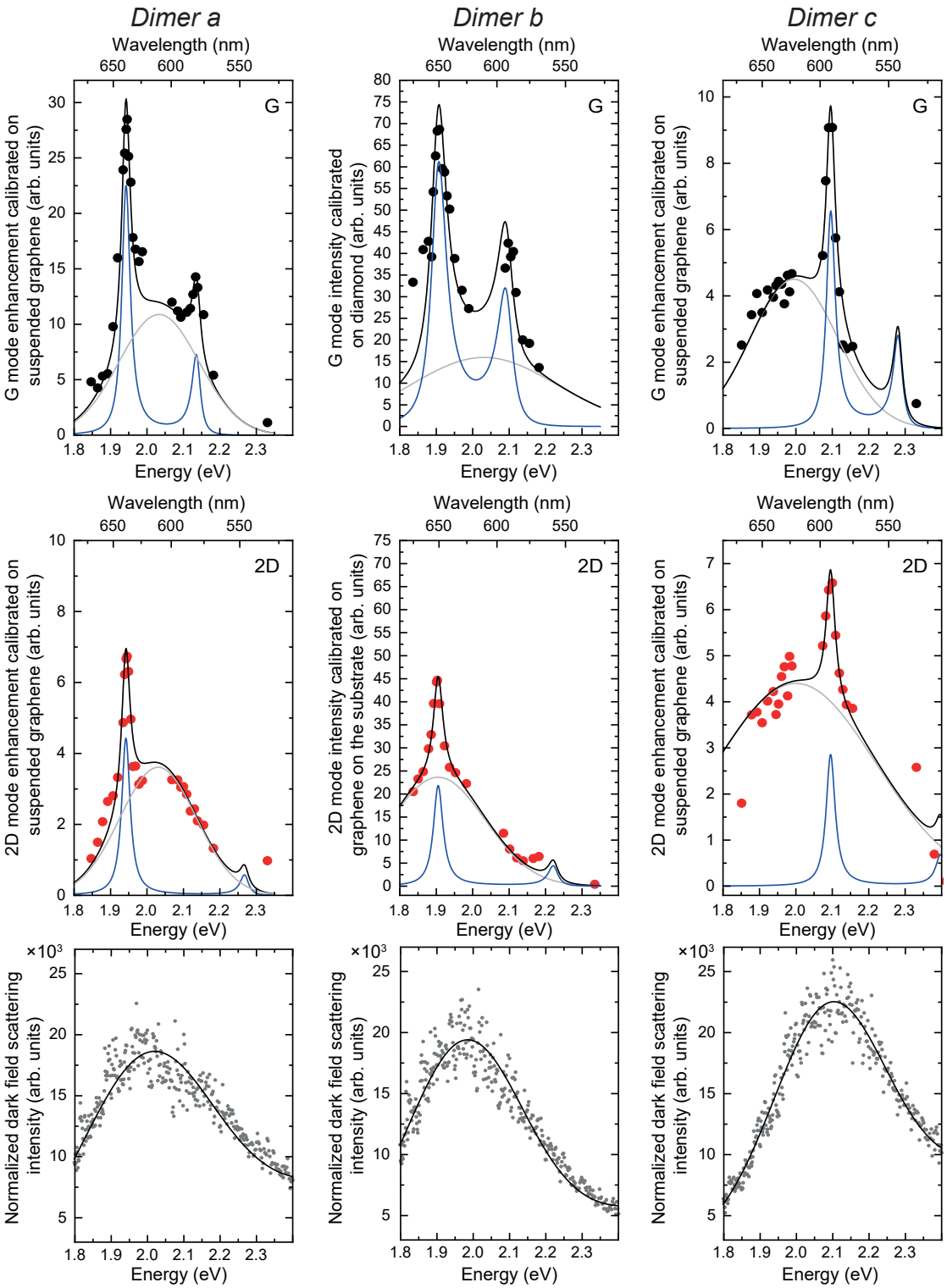

Figure 6.11 Wavelength-dependent Raman measurements of the G (black) and 2D (red) mode of three additional dimers fitted by the HORa theory with a Gaussian background. In the bottom panels the corresponding dark-field spectra. The dots are experimental data and the solid lines are the Gaussian fits.

The dark-field spectra show a broad maximum as was observed above (see Chapt. 6.6 and were fitted by Gaussian fits. All the fitting parameters of the wavelength-dependent Raman measurements (narrow resonances) and the dark-field scattering spectra are listed in Tab. 6.1.

Table 6.1 Fitting parameters of the wavelength-dependent Raman measurements (narrow resonances) and dark-field scattering spectra.

		Dimer a	*Dimer b*	*Dimer c*
Raman	ω_{pl} (eV)	1.942	1.905	2.095
	γ_{pl} (eV)	0.014	0.025	0.015
Dark field	ω_{pl} (eV)	2.002	1.977	2.092
	γ_{pl} (eV)	0.177	0.158	0.152

A blue shift of the resonance of *Dimer 3* is clearly visible. It is attributed to the etching of the substrate for *Dimer 3*. The width of the plasmonic resonances in the near field (Raman) are one order of magnitude smaller than the resonance of *Dimer I*. As observed for the dimer discussed above a redshift of the near-field resonance compared to the far-field resonance is observed. The smallest difference is measured for *Dimer 3* where both measurements are in good agreement.

6.8 Plasmonically activated D mode

For all dimers investigated above, a D mode was observed when in resonance with the plasmon whereas no indication of defect modes was visible when measuring out of resonance or with polarization perpendicular to the dimer axis, as expected for high quality mechanically exfoliated graphene. A plasmonically activated D mode was reported previously.[101] The very strong confinement of the plasmonic near field in the dimer gap enables a direct activation of the D mode without a defect necessary for momentum conservation. This mechanism also applies for the D′ mode. Figure 6.12 (a) shows the defect activated process of both modes (as introduced in Chapt. 4.1) and (b) the plasmonic activated process.

In the Raman spectra it is possible to find evidence for the plasmon activated mechanism. In Fig. 6.12 (c) different Raman spectra of the D mode region are shown, for two excitation wavelengths. In the lower part of the panel the D mode is observed at 638 nm when the polarization is along the dimer axis (red spectrum) activating the plasmonic hotspot in the dimer gap. Turning the polarization perpendicular to the dimer (orange spectrum) the D mode vanishes. There is, likewise, zero D mode intensity if a spectrum is measured next

to the dimer (light red), as expected for exfoliated graphene. Comparing the spectrum next to the dimer and perpendicular to the dimer axis, there is a small broadening in the G mode in the latter one which might origin from the plasmonic near field of the single gold particles. Comparing the Raman spectra on the dimer (green) and next to the dimer (ligth green) at 532 nm excitation there is no indication of the D mode as well.

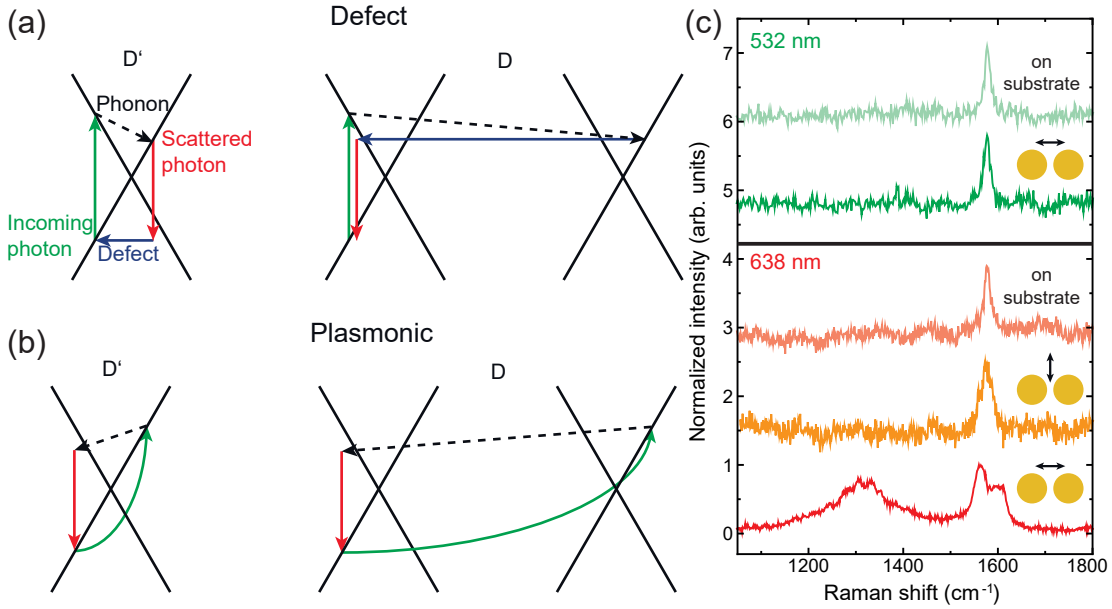

Figure 6.12 D and D′ mode activation **(a)** with defect for momentum conservation. **(b)** Strong confinement of the plasmonic near field allows for non vertical activation. **(c)** Raman spectra of the D and G mode region at 638 nm on the dimer with polarization along the dimer axis (red), perpendicular to the dimer axis (orange) and recorded next to the dimer (light red). On the dimer at 532 nm (green) and next to the dimer (light green). The spectra are offset for clarity and normalized to the G mode.

Alternatively, the defect modes may originate from point defects in the cavity that are only visible when plasmonically enhanced. The broad shape of the D mode is rather unusual for a defect induced mode, consolidating the assumption of a plasmon-induced process.

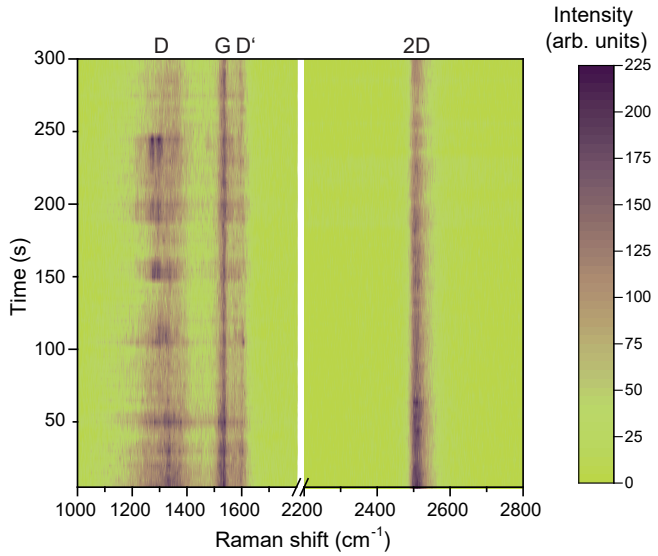

Figure 6.13 The Raman signal of the G and 2D mode recorded on the dimer over time. Each line shows the Raman intensity measured for 5 s. The measurement was performed at 602 nm laser wavelength.

A phenomenon often observed in SERS is the so-called blinking of Raman modes.[102] It describes the sudden change in intensity of Raman modes over time. Figure 6.13 shows a series of Raman spectra of the G and 2D mode as a function of time. There is a small overall loss in intensity with time, presumably due to a shift in the sample position (defocusing). Neglecting this change, the intensities of G and 2D mode remain constant, making them perfect candidates to evaluate the integrated local field of the plasmonic system. In contrast, blinking occurs in the region of the D and D′ mode. These modes most likely depend on highly mobile and extremely localized features in graphene and/or in the plasmonic nanodimer such as mobile defects in graphene or mobile gold atoms.[102] The different behavior of the graphene Raman modes makes graphene an excellent material to test and compare plasmonic systems. The constant G and 2D modes allow the investigation of the plasmonic resonance whereas the blinking defect modes can give more information about the confinement of the plasmonic near field and is another indicator that the D mode is plasmon activated. It will be topic of future investigations.

6.9 Summary

In this chapter I discussed the effect of the plasmonic near field of gold nanodimers on the Raman enhancement of graphene. Mechanically exfoliated graphene was suspended

over the dimer. Due to adhesion forces, the graphene is pulled to the substrate and into the dimer gap and therefore in the plasmonic hotspot. Analyzing the Raman spectrum when focusing on the dimer hotspot gives access to the local strain and doping of the graphene in the dimer gap. Polarization-dependent Raman measurements showed the influence of the plasmonic near field to the Raman intensity. Instead of an independent polarization behavior, I observed maximum Raman intensity when the polarization was aligned with the dimer axis. Graphene was chosen as the Raman reporter because of its constant Raman cross section. All changes in the Raman spectrum depending on excitation wavelength can therefore be attributed to the plasmonic near field. I was able to determine the plasmonic near- (Raman scattering) and far-field (dark-field scattering) resonance of different dimers. A red shift of the near-field resonances compared to the far-field measurements is observed. When excited at the plasmon resonance energy indications of a plasmonic activated defect mode are evident.

7 | Plasmonic enhancement of (7,5) CNTs

In this chapter I will switch from the non-resonant Raman reporter graphene, discussed in the previous chapter, to carbon nanotubes placed inside the gold dimer gap and exposed to the plasmonic near field. CNTs have some similar properties to graphene but also major differences, for example, their polarization dependence and their intrinsic resonances as decribed in Chapt. 4. I focus on chirality enriched (7,5) CNTs. This chirality was chosen because its intrinsic resonane (E_{22}) is located at $E_{(7,5)} = 1.915$ eV which is at a similar energy as the plasmon resonance of the dimer.[30]

I will first describe the investigated system in detail. I will follow it up with polarization-dependent Raman measurements of the CNTs in the dimer gap and close this chapter with wavelength-dependent Raman measurements to investigate the interplay of the plasmonic resonance with the intrinsic resonance of the CNT. To investigate both resonances separately I performed wavelength-dependent measurements in two polarization configurations. First, the polarization was chosen along the dimer axis, activating its plasmonic near field and a coupling between the dimer and the CNT. Second, the polarization was along the tube axis, where the plasmonic hotspot in the dimer gap is not excited and only the Raman process in the CNT is activated.

7.1 Sample geometry

In this section I introduce the investigated system. A large field of gold dimers and electrodes were prepared by e-beam lithography (see Chapt. 5.1). The dimers consist of two gold half ellipsoids with a diameter of 100 nm and a height of 80 nm. An adhesion layer of 5 nm chromium was deposited between the substrate and the gold. The shape of the dimer (half ellipsoids compared to cylinders) is favorable for the CNT going into the gap of the two gold particles putting them into the plasmonic hotspot. The gold

electrodes are used for the dielectrophoretic deposition of the dimers and do not influence the plasmonic near field of the dimer.[32]

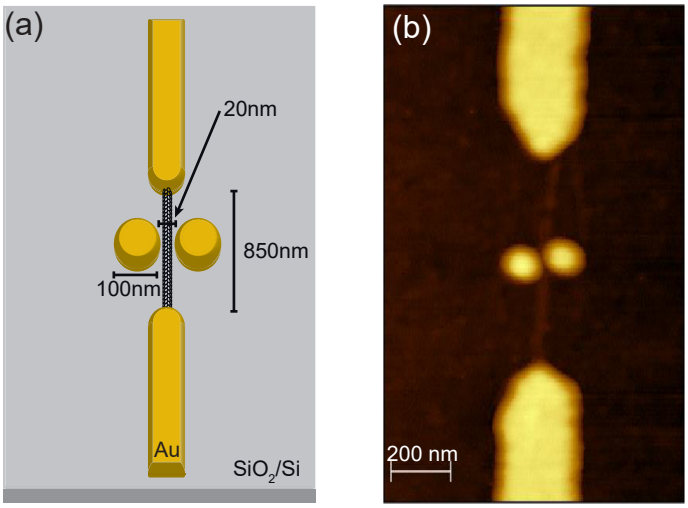

Figure 7.1 **(a)** Sample geometry of the investigated system. Enriched (7,5) nanotubes are deposited in the middle of a gold nanodimer consisting of half spheroids with a height of 80 nm. **(b)** AFM topography of a CNT going through the dimer gap.

In Fig. 7.1 a sketch with the dimensions of the system is shown. The dimers are rotated by an angle of 90° degree compared to the electrode axis. This configuration facilitates the deposition of the CNTs inside of the dimer gap.

The Raman spectra in Fig. 7.2 show a comparison of a raw CNT sample consisting of multiple chiralities (bottom) and of a single CNT chirality (top). In the single chirality spectrum only a single RBM was measured corresponding to the (7,5) species at $\omega_{RBM}^{(7,5)} = 283$ cm^{-1}. In the raw CNT material multiple RBMs are observed.

The polarization and wavelength dependent Raman measurements were performed at the T64000 setup, see Chapt. 5.5. The wavelength-dependent Raman measurements of the RBM were calibrated on CaF_2.

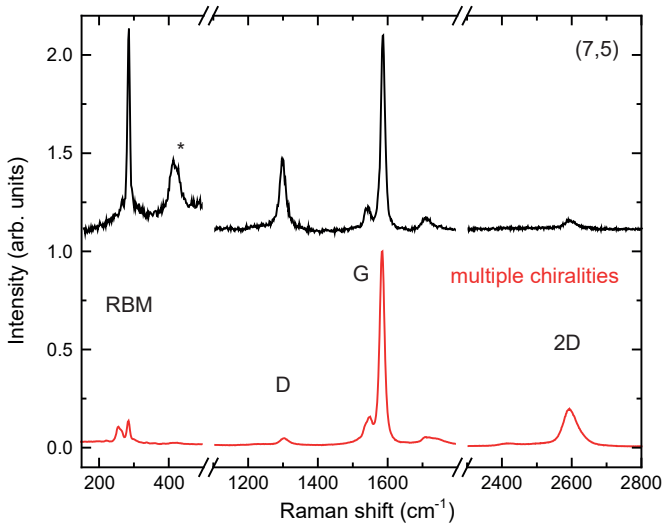

Figure 7.2 Raman spectra of a raw CNT sample with multiple chiralities (bottom) and of enriched (7,5) nanotubes (top). The characteristic Raman modes are labeled ($*$ intermediate mode). The intensities are normalized to the G mode. The excitation wavelength is $\lambda_l = 638$ nm.

7.2 Polarization-dependent measurements

The influence of the plasmonic near field to a highly anisotropic Raman reporter like CNTs is investigated by polarization-dependent Raman measurements. The Raman intensity of the G mode and RBM were measured as a function of polarization angle. I will show the polarization dependence of two nanotubes deposited in the plasmonic hotspot of a gold dimer in Fig. 7.3.

The dimer is oriented perpendicular to the nanotube axis. For both bundles different symmetry directions with local maximum intensity are visible. The stronger maximum is observed along the dimer axis and a weaker maximum along the CNT axis. Two competing processes are observed. When polarized along the dimer axis the plasmonic near field enhances the Raman scattering. As described in Chapt. 4 no Raman intensity is observed when polarized perpendicular to the nanotube axis. The near field is projected on the CNT axis to enable the Raman scattering process. Even though the dimer is oriented perpendicular under experimental conditions the near field of the dimer will experimentally not completely perpendicular to the nanotube. The second maximum in Raman intensity is observed when polarized along the nanotube axis, as expected for CNTs. When polarized along the nanotube no plasmonic enhancement is expected because the two particles of the dimer act as single particles and the near field does not

extend to the CNT. The polarization-dependent measurements are fitted by the two contributions

$$I_{pol}(\Theta) = I_{SERS} + I_{CNT} = a^2 \sin(\Theta)^4 + b^2 \cos(\Theta)^4. \tag{7.1}$$

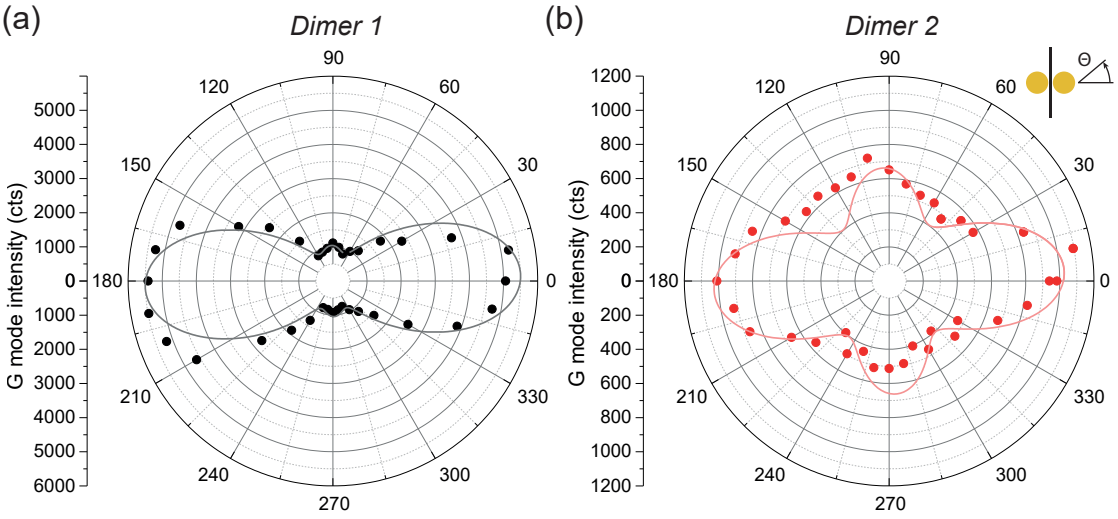

Figure 7.3 Polarization-dependent Raman measurements of the G mode of (7,5) CNTs in a dimer gap of two different dimers at **(a)** $\lambda_l = 648$ nm and **(b)** $\lambda_l = 633$ nm excitation wavelength. The inset in **(b)** shows the measurement configuration.

As I observe two separate maxima I have to consider each single contribution. The total intensity is described as the sum of the intensity of the plasmonic near field and the CNT. This suggests that the different scattering paths do not interfere. The fitting parameters are listed in Tab. 7.1. The fits agree well with the measured profile.

Table 7.1 Fitting parameters of the polarization-dependent measurements according to Eq. (7.1).

	a	b
Dimer 1	74.2	32.3
Dimer 2	32.0	25.7

While both polarization profiles show maxima in the direction of the CNT axis and the dimer axis, the ratio between the fitting parameters a and b is very different. I attribute the difference to the placement of the nanotube in the dimer gap. A tilt of the CNT or a misplacement compared to the middle of the dimer leads to a better projection of the

plasmonic near field to the nanotube and therefore higher Raman intensity along the dimer axis, as in Fig. 7.3 (a).

7.3 Wavelength-dependent measurements

In this section I will show wavelength-dependent Raman measurements of (7,5) CNTs deposited in a gold dimer gap. I will compare two cases: i) polarization along the nanotube axis, ii) polarization along the dimer axis. The dimer is oriented perpendicular to the nanotube axis, see Fig. 7.1. As discussed in the previous section, turning the polarization of the exciting light gives two scattering configurations. If the light is along the nanotube axis, only conventional Raman scattering, i.e. resonant Raman scattering will be observed. In Fig. 7.4 I compare the Raman spectra of the different polarization configurations. If polarized along the dimer axis the CNT Raman modes are stronger than when polarized along the nanotube axis. If the dimer is excited a plasmonic hotspot will form in the gap between the two gold discs enhancing the Raman intensity of the CNT, i.e. SERS. If the dimer is excited perpendicular to the nanotube axis two LSPs will form and both discs will act as single plasmonic particles. I assume that the plasmonic near field does not influence the CNT in that case because of the small extension of the plasmonic near field in the CNT direction and the one dimensional nature of CNTs.

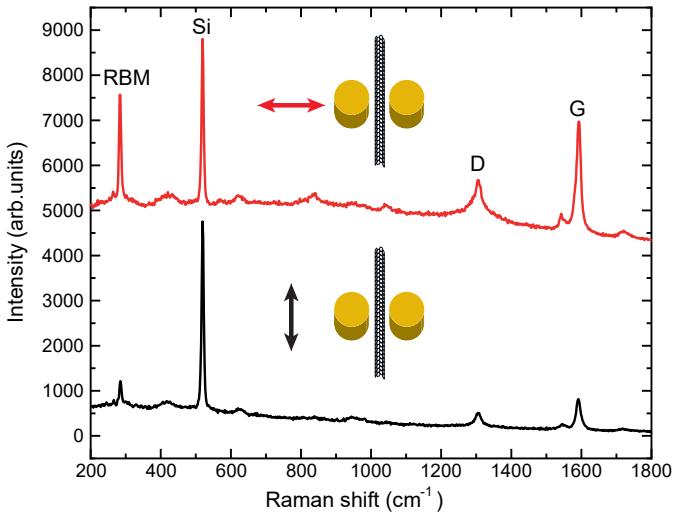

Figure 7.4 Raman spectra of a CNT bundle inside of the gold dimer gap with polarization along the dimer axis (red) and perpendicular to the dimer axis (black). The excitation wavelength is $\lambda_l = 638$ nm.

To investigate the influence of the plasmonic near field on the Raman intensity I tuned the excitation energy E_l and acquired Raman spectra in both polarization configurations as described above. First, I will discuss the polarization along the nanotube axis where no plasmonic enhancement is present, see Fig. 7.5 (a).

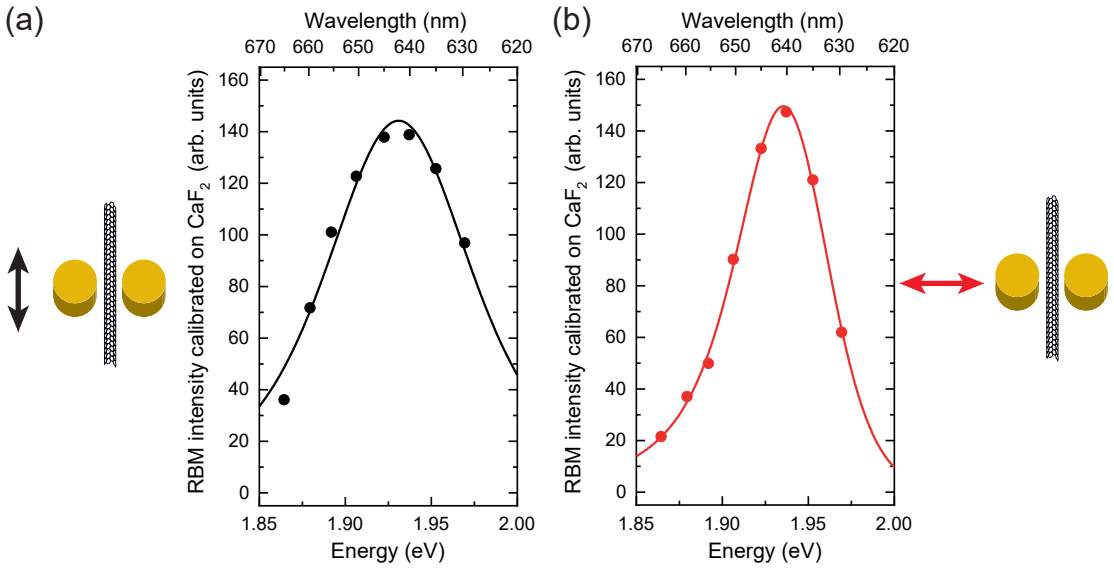

Figure 7.5 Wavelength-dependent Raman measurements of (7,5) nanotubes inside of the dimer gap. Polarization along the nanotube axis (black), polarization parallel to the dimer axis (red). The intensity of the RBM is plotted over the excitation energy. Dots are the experimental data and solid lines are the fits.

The Raman intensity of the RBM shows a maximum at 1.93 eV. To fit the experimental data I use the following expression that is used to fit resonant Raman scattering, see Chapt. 3.

$$I_{(7,5)}(E_l) = \left| \frac{M_{(7,5)}}{(E_l - E_{(7,5)} - \hbar\omega^{7,5}_{RBM} - i\gamma_{(7,5)})(E_l - E_{(7,5)} - i\gamma_{(7,5)})} \right|^2 , \tag{7.2}$$

where $M_{(7,5)}$ is the matrix element, $E_{(7,5)}$ the resonance energy of the measured (7,5) nanotube, $\omega^{7,5}_{RBM}$ the phonon frequency of the (7,5) RBM, and $\gamma_{(7,5)}$ the width of the resonance. The fit yields $E_{(7,5)} = 1.92$ eV with a width of $\gamma_{(7,5)} = 0.08$ eV. In resonant Raman scattering of semiconductors an incoming and outgoing resonance is observed. Because of the small Raman frequency of the RBM both resonances overlap and are not resolved individually resulting in one broad resonance.[30] The resonance energy is in excellent agreement with values reported in the literature.[30]

In Fig. 7.5 (b) the plasmon enhanced Raman intensity of the RBM (polarization along the dimer axis) is plotted over the excitation energy. To fit the SERS intensity I use the HORa theory, introduced in Chapt. 3. The theory incorporates the plasmon in the Raman process in a quantum mechanical treatment in perturbation theory.

$$I_{SERS}(E_l) = \left| \frac{M_{pl} M_{(7,5)}}{(E_l - \hbar\omega_{(7,5)} - E_{pl} - i\gamma_{pl})(E_l - E_{(7,5)} - \hbar\omega_{(7,5)} - i\gamma_{(7,5)})} \right. \\ \left. \frac{1}{(E_l - E_{(7,5)} - \hbar\omega_{(7,5)} - i\gamma_{(7,5)})(E_l - E_{pl} - i\gamma_{pl})} \right|^2 , \tag{7.3}$$

where E_{pl} is the plasmon energy and γ_{pl} its width. With the parameters of the resonant Raman fit inserted in Eq. (7.3) the HORa fit yields $E_{pl} = 1.91$ eV with a width of $\gamma_{pl} = 0.08$ eV. Comparing the two wavelength-dependent profiles the plasmon enhanced profile is narrower due to the additional contribution of the plasmon.

For the measured dimer it was not possible to compare the near-field resonance obtained by Raman scattering with the far-field response measured by dark-field scattering, as discussed for graphene in Chapt. 6, because the electrodes used for the dielectrophoretic deposition influence the dark-field spectrum. Compared to the Raman measurements the gathering area in the dark-field measurements is larger and more sensitive to the environment of the dimer. In the dark-field measurements the whole sample is illuminated and only the scattered light of a certain area collected.

A downside in the experiments performed on the (7,5) nanotubes was that the Raman scattering intensity was not long term stable and went down after a series of measurements was performed. It was most likely due to the strong enhancement in the hotspot even though very small excitation power of only a few microwatts was used. In the process of chirality enrichment the nanotubes are wrapped with a polymer that might play a role in the stability of the nanotubes when deposited on a substrate.

7.4 Summary

In this chapter I showed that with dielectrophoretic deposition it is possible to precisely place CNTs in the gold dimer gap leading to enhancement of the Raman modes. Polarization-dependent measurements show that both the plasmonic resonance as well as the intrinsic resonance lead to maxima. The relative strength most likely depends on the position of the CNT in the dimer gap and therefore the projection of the plasmonic near field on the CNT. Wavelength-dependent measurements showed that the resonance of the investigated (7,5) nanotubes and the used gold dimer match very well. By turning

the polarization it was possible to measure only the intrinsic nanotube resonance and the combination of plasmonic and CNT resonance. The plasmonic near field leads to a more narrow resonance compared to the intrinsic resonance.

8 | Plasmonic enhancement of α-6T@CNT[1]

[1]The content of this chapter was published as *Resonant, Plasmonic Raman Enhancement of α-6T Molecules Encapsulated in Carbon Nanotubes* in Wasserroth et al. *The Journal of Physical Chemistry C, 123(16)*:10578–10585, 2019, https://doi.org/10.1021/acs.jpcc.9b01600. S. Reich and I planned and conceived the experiments. The encapsulation of the molecules in the CNT was performed by E. Gaufres, N. Y.-W. Tang, and R. Martel. The gold structures were fabricated by U. Hübner. S. Heeg and A. Vijayaraghavan deposited the filled nanotubes. I performed the Raman measurements and AFM characterization. P. Kusch provided support with the Raman measurements. N. Mueller gave input to the HORa theory. I interpreted the data and wrote the manuscript. All authors commented on the manuscript.

9 | SERS using an LED as excitation source

So far I have shown SERS measurements on dimer structures that were designed as a model system to investigate the fundamental properties of the SERS process. In this chapter I will use a commercially available SERS substrate with a high enhancement factor to show a potential application of SERS. I combine the SERS substrate with a light emitting diode (LED) excitation for Raman spectroscopy. I show the feasibility of this approach with four different Raman reporters and compare the LED excitation with laser excitation at the same wavelength.

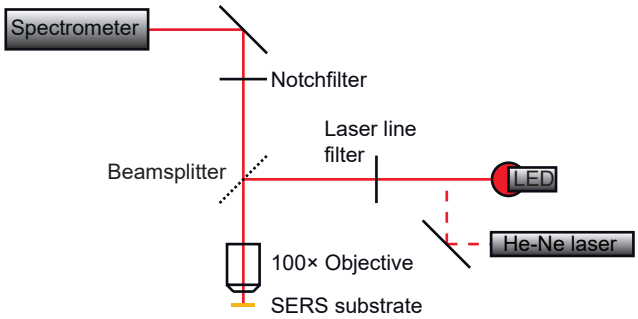

Figure 9.1 Sketch of the used experimental setup. The different samples were deposited on a commercial SERS substrate and measured with a He-Ne laser and an LED.

A micro Raman setup is used in this experiment where different light sources can be easily coupled in. Figure 9.1 shows a sketch of the experimental setup. As excitation sources an LED (Thorlabs M625L3 700 mW with collimator) and a He-Ne laser (Coherent) are used. The Raman spectra measured with the LED were acquired with 2 µW power on the sample and 30 s acquisition time, whereas the laser provided 14 µW power on the sample with 10 s acquisition time. In both cases the light passed through a bandpass filter (632.1 nm; FWHM=(1±0.2) nm) and was focused through a 100× objective (NA=0.9) on

the sample. The setup was used in backscattering configuration. The elastically scattered light was removed by a notch filter. The inelastically scattered light was dispersed in a Horiba T64000 Jobin Yvon spectrometer (single grating configuration) and detected with a silicon charge coupled device.

For SERS, I used the commercially available Silmeco SERS substrate. It is made of nanostructured silicon covered with gold. I acquired Raman spectra of 5,5-dithio-bis-(2-nitrobenzoic acid) (DTNB), Rhodamine 6G (R6G), 4-nitrothiophenol (p-NTP), and carbon nanotubes (CNTs). DTNB is an organic molecule that inhibits two Raman modes with the same origin as in p-NTP but in a different chemical environment. Both can be distinguished by Raman spectroscopy. One mode originates from the C-C stretch vibration and the second one from the NO_2 group present in both molecules. p-NTP is a designer molecule used in SERS to investigate the plasmonic enhancement of SERS substrates.[106] It is often chosen in SERS experiments because it easily functionalizes gold particles through its thiolgroup and therefore reports the SERS enhancement.[106] As a third reporter I chose Rhodamine 6G which is often used in SERS experiments to investigate different chemical reactions and as a biomarker. As an example of a solid state one dimensional system, I performed SERS measurements on carbon nanotubes (CNTs). The different probes were prepared in solution and drop cast on the SERS substrate. The concentration of DTNB was $c_{DTNB} = 100$ µM, for R6G 0.66 g/L, and for p-NTP $c_{p-NTP} = 10$ mM. The concentration of the CNTs (ComoCat) is 0.1 g/L. They were debundled and centrifuged before deposition.

Figure 9.2 shows the Raman spectra of the different reporters where both excitation sources are compared. In all four Raman spectra I was able to unambiguously identify the respective Raman reporter. The characteristic Raman modes were clearly visible in the different spectra. The dashed lines in Fig. 9.2 indicate the Raman peaks whose fit parameters are listed in Tab. 9.1. The Raman peaks were fitted by Lorentzians.

First, I discuss the peak position of the Raman reporters. All peaks are at the same position within the resolution of the measurement ($\Delta\omega_{pos} = 2$ cm^{-1}) with two exceptions: The N-O mode of DTNB and the C-S mode of p-NTP. Looking at the spectral range of these two peaks it is noticeable that multiple peaks are observed near the modes (especially in the spectra recorded with the laser) that might lead to a shift between the modes originating in the fitting process. I was able to distinguish the N-O mode of DTNB and p-NTP despite them having the same origin and only differing in Raman spectroscopy because of the different chemical environment of each mode influencing the Raman shift. The least separation of 41 cm^{-1} when excited with the LED of two Raman peaks observed in the set of Raman reporters is between the CNT G^- and G^+ mode.

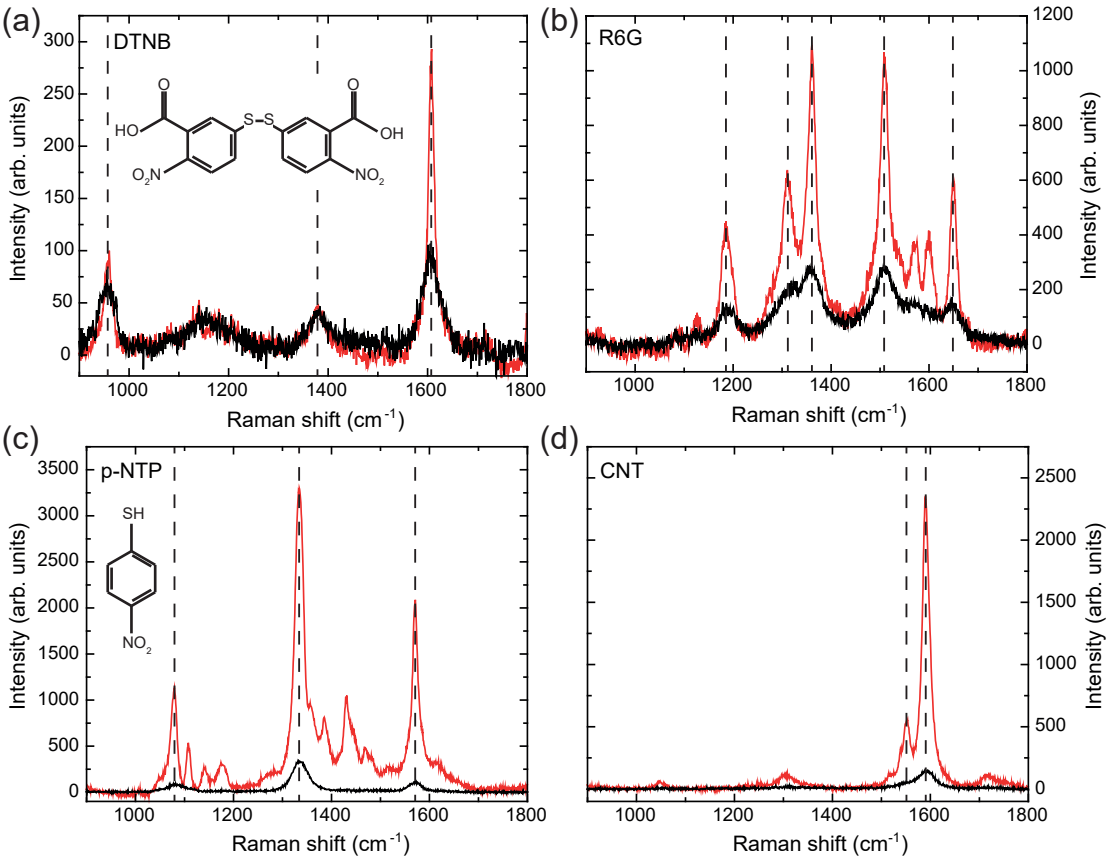

Figure 9.2 Raman spectra of the **(a)** DTNB, **(b)** R6G, **(c)** p-NTP, and **(d)** CNT reporter measured with the He-Ne laser (red) and with the LED (black). The dashed lines indicate the discussed Raman modes in Tab. 9.1. The insets in **(a)** and **(c)** show the chemical structure of p-NTP and DTNB, respectively.

The second parameter of the fitting I discuss is the FWHM. A broader FWHM is observed when the reporters are excited with the LED. The FWHM is larger by a factor between 1.7 (R6G C-C mode at 1309 cm^{-1}) and 3.1 (p-NTP C-S mode). The width of the peaks is determined by the width of the excitation source. In case of the LED it is limited by the bandpass filter (FWHM=1 nm), whereas for the laser it is limited by the laser bandwidth itself.

Finally I compare the intensity of the different Raman peaks. In general there are two noticeable observations. The intensity of the Raman spectra measured with the LED are all in the same order of magnitude whereas there are large differences in the laser excitation (one order of magnitude difference between DTNB and p-NTP). A possible explanation to the relatively large difference between laser and LED excitation

is the lower power density in case of LED excitation. The bandpass filter and beam path from the LED to the sample cuts away a large part of the emitted power of the LED. Combined with a possibly larger focus size this leads to smaller Raman intensities. The overall similar Raman intensities in case of LED excitation might be an indicator that mostly plasmonic-enhanced Raman scattering is observed while in case of laser excitation additional conventional Raman scattering is observed leading to generally higher intensities.

In conclusion, I was able to proof the concept of LED Raman excitation with a SERS substrate. A very simple setup consisting of the excitation source, a microscope, and a spectrometer was able to unambiguously determine four different Raman reporters. Broader Raman peaks were observed where the FWHM is limited by the bandpass filter. By increasing the light power on the sample it will be possible to increase the overall Raman intensity. I envision the combination of LED excitation with SERS substrates for low-budget Raman sensors and handheld devices.

Table 9.1 Comparison of the Lorentzian fitting parameters of the DTNB, R6G, p-NTP and CNT Raman spectra measured with the LED and the laser shown in Fig. 9.2.

	peak		position (cm^{-1})	FWHM (cm^{-1})	Intensity (cts)
DTNB	C-N	LED	956	38	66
		laser	958	18	89
	N-O	LED	1385	70	34
		laser	1379	35	41
	C-C	LED	1606	43	93
		laser	1608	16	277
R6G	C-C	LED	1188	45	112
		laser	1186	22	427
	C-C	LED	1309	61	133
		laser	1311	36	530
	C-C	LED	1360	55	220
		laser	1361	23	958
	C-C	LED	1508	58	235
		laser	1509	28	932
	C-C	LED	1648	36	108
		laser	1650	15	580
p-NTP	C-S	LED	1083	44	82
		laser	1078	14	1119
	N-O	LED	1336	36	346
		laser	1336	20	3360
	C-C	LED	1570	33	104
		laser	1571	12	1757
CNT	G^-	LED	1551	48	28
		laser	1550	18	439
	G^+	LED	1592	37	140
		laser	1591	17	2327

10 | Summary and outlook

The goal of the thesis was to investigate the fundamental scattering mechanism behind surface-enhanced Raman scattering. A well defined plasmonic system consisting of two gold discs forming a dimer was used. The dimer system has many advantages. The plasmonic hotspot in the gap between the discs can be activated by changing the polarization of the exciting light. A dimer is a very good model system in the sense that the plasmonic near field can easily be simulated. The gold dimers investigated in this thesis were produced by e-beam lithography and can reliably be reproduced in disc and gap size. To probe the plasmonic near field I measured different Raman reporters in the hot spot. The first reporter I chose was graphene. Because of the constant Raman cross section of graphene in the visible regime all changes in the Raman intensity are attributed to the plasmonic near field. To learn about the interplay of intrinsic resonances that are present in most Raman reporters, investigated in SERS, I use chirality enriched (7,5) carbon nanotubes and α-6T molecules encapsulated in CNTs. With wavelength-dependent Raman measurements I studied the influence of the plasmonic near field on the different Raman reporters. In the last part I showed a proof of concept of LED excited Raman scattering combined with a SERS substrate for potential low-budget Raman sensors and handheld devices.

After introducing the fundamentals necessary to understand the experiments, I presented an extensive characterization of gold nanodimers covered with graphene. The dimer consists of two gold discs with a diameter of 100 nm, a height of 45 nm and an approximate gap size of 20 nm. The localized surface plasmon resonance is located in the visible around 650 nm. Mechanically exfoliated graphene was suspended over the dimer. It was shown that adhesive forces pull the graphene to the substrate and in the gap between the discs and is therefore exposed to the plasmonic hotspot of the dimer.[27;28;66] The strain of the graphene in the hotspot is visible in the Raman spectra. Strain leads to a shift and splitting of the graphene G and 2D mode. With spatial Raman measurements in the plane of the dimer I was able to measure the strong confinement of the plasmonic

near field. The spatial size of the enhanced Raman intensity corresponded to the laser focus size confirming the point like character of the plasmonic hotspot. In z-dependent scans the strong localization of the hotspot is evident as well. The Raman intensity of the 2D mode differs strongly if the light is focused on the plasmonic hotspot or the graphene on the substrate. The measured intensity is in good agreement with the calculated point spread function of a point like scattering center. The strong influence of the plasmonic near field on the Raman intensity is visible in polarization-dependent Raman measurements. If the incoming light is polarized along the dimer axis the plasmonic hotspot is active and strong enhancement is observed. If polarized perpendicular, only the normal Raman process and small enhancement from the two individual plasmonic particles are observed. With wavelength-dependent measurements I was able to determine the plasmon resonance since graphene has a constant Raman cross section. The incoming resonance was found at $E_{pl}^{Raman} = 2.01$ eV with a width of FWHM = 0.33 eV for the G and 2D mode with the outgoing resonance separated by the phonon energy. I used the HORa theory to fit the experimental data. I compared the resonance energy measured by the Raman measurements with dark-field spectroscopy. With this method the elastic light scattering is probed and the scattered light is measured in the far field with a resonance energy of $E_{pl}^{darkfield} = 2.18$ eV whereas Raman scattering measures the near-field resonance. I measured a difference of 0.17 eV between the near-field (Raman) and far-field (dark-field) resonance. A difference between near- and far-field resonance was observed before, but the proposed mechanism failed to explain the relatively strong difference that I measured. To learn more about this energy difference a new experiment is planned. With a scattering type scanning near-field optical microscope (s-SNOM) it is possible to visualize plasmonic near fields. The s-SNOM measures elastic scattering in the near field. Figure 10.1 shows preliminary results of a near-field image of a gold dimer in amplitude and phase. The near-field distribution with a strong hotspot is observed. The phase jump in the middle of each disk is observed. By changing the excitation wavelength and collecting the near-field intensity in the s-SNOM setup it might be possible to disentangle where the difference in energy between the Raman and dark-field scattering arises from.

After the extensive characterization of the first dimer, I showed wavelength-dependent measurements of three more dimers covered with graphene. In contrast to the first dimer, they show very narrow resonances (FWHM 0.014-0.025 eV) superimposed on a broad background. I was able to observe an incoming and outgoing resonance in the G mode. For the 2D mode the outgoing resonance could not be observed due to a lack of laser excitation. For one dimer the SiO_2 layer of the substrate was edged leading to a shift of the incoming resonance due to a change of the dielectric environment of the dimer. The

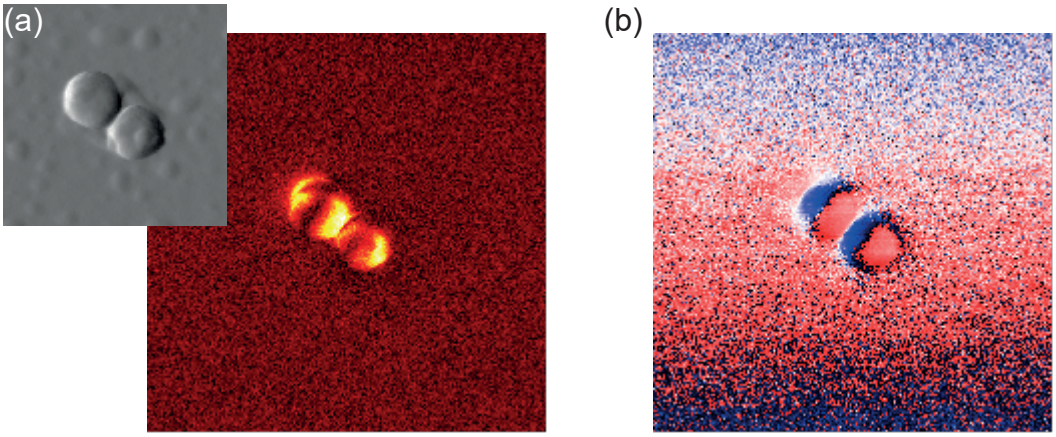

Figure 10.1 s-SNOM image recorded with a NeaSnom. **(a)** Near-field image O_{4A} of a gold dimer with AFM topography in the inset. **(b)** Near-field phase image O_{4P}.

very narrow width of the resonances will be subject of future investigations. A first idea was that so-called dark plasmon modes are responsible for the narrow resonances.[107] Dark modes are plasmon modes that cannot be excited by linear polarized light but for example by different laser modes. The dark modes have a longer lifetime than bright modes resulting in narrower resonances. But even the dark modes do not lead to such narrow resonances. The origin of the long lifetimes measured at theses dimers will be part of future projects. For SERS measurements it would be an interesting route to exploit these narrow resonances if it is possible to reproducible tune them to a specific energy fitting to the excitation wavelength used. The narrow resonances are able to yield strong enhancement at the respective energy.

In all investigated dimers I observed a D mode when strong plasmonic enhancement was present. An activation of a plasmonically activated D mode was reported before.[101] The strong confinement of the plasmonic hotspot enables a new scattering path for the D mode without defect scattering for momentum conservation.

Graphene is an excellent candidate to study the plasmonic properties of SERS substrates but most Raman reporters investigated in SERS measurements have an intrinsic resonance therefore it is important to understand the interplay of the intrinsic resonance of the reporter with the external influence of the plasmonic near field. A natural choice coming from graphene are carbon nanotubes, the one-dimensional carbon allotrope. CNTs inhibit intrinsic resonances that depend on the chirality of the nanotube. I studied single chirality (7,5) nanotubes that were placed precisely in the dimer gap by dielectrophoretic deposition. (7,5) CNTs have their resonance at $\sim$ 650 nm which coincides with the plasmonic resonance. For the (7,5) CNT measurements I chose a configuration where

the CNT is aligned perpendicular to the dimer axis. Polarization-dependent Raman measurements revealed two maxima: One in the dimer axis and one on the nanotube axis. If the polarization is chosen along the dimer axis plasmonic enhancement is present. If the incoming light is polarized along the CNT axis there is no plasmonic near field extending to the nanotube and only the normal Raman scattering process is observed. In wavelength-dependent Raman measurements in both polarization directions the matching resonances of the (7,5) chirality with the plasmonic resonance is confirmed. In case of the SERS measurement a narrowing of the resonance is observed compared to the resonant Raman measurements without plasmonic enhancement with polarization along the nanotube axis. CNTs are a good Raman reporter to study the influence of the plasmonic near field to intrinsic Raman resonances by changing the tube chirality and therefore tune the energy difference between intrinsic and plasmonic resonance. In the future it would be interesting to investigate different chiralities as well.

CNTs provided a good environment to probe the plasmonic near field with a resonant anisotropical reporter. By functionalizing CNTs it is possible to place molecules in the plasmonic hotspot with known position and orientation. Endohedral functionalization excludes chemical enhancement because the encapsulated molecules are protected from the environment by the CNT.[32] α-6T molecules were encapsulated in CNTs and deposited by dielectrophoretic deposition. The molecules align within the CNT in a head-to-tail structure parallel to the CNT axis.[40;39] I compared two filled tube bundles: One is deposited in a gold dimer gap and the other one on the substrate without plasmonic system. First, I showed a resonant Raman measurements on the reference without plasmonic enhancement. I determined the resonance energy of the encapsulated molecules at $E_{\alpha-6\mathrm{T}} = 2.35$ eV. Polarization-dependent Raman measurements confirmed the alignment of the molecules with the nanotube axis. The results found in the resonant Raman measurements on the reference were used to find the plasmonic resonance of the tube bundle deposited in the dimer gap. The plasmon resonance was found with the HORa theory at $E_{pl} = 1.95$ eV. I observed maximum enhancement between both resonance at $E_{pl} = 2.10$ eV with an enhancement factor of $EF \approx 10^5$.

In the last chapter I showed a possible application of SERS. I combined LED excitation with the strong enhancement of a SERS substrate. I coupled the LED into a micro Raman setup and collected the scattered light in the spectrometer. The used setup was simplistic suited to show a proof of concept. I compared the LED excitation with laser excitation at the same wavelength. Four different Raman reporters were unambiguously detected. The FWHM of the Raman peaks acquired with LED excitation was broader than with laser excitation. The width of the LED peaks was limited by the bandpass

filter in front of the LED. The combination of LED excitation and high enhancement SERS surfaces is a good candidate for low-budget Raman sensors and handheld devices. In summary, I investigated the influence of plasmonic near fields on different Raman reporters. I showed that Graphene is an excellent candidate to study SERS substrates and investigate the plasmonic properties. I was able to show the strong localization of the plasmonic near field of a gold dimer by Raman measurements and determined the plasmonic resonance. With (7,5) carbon nanotubes and α-6T molecules encapsulated in CNTs I studied the interplay between the plasmonic and intrinsic resonance. In the end I showed a proof of concept of an application of SERS using light excitation of an LED with the high enhancement of a SERS substrate for possible low-budget Raman systems.

Acknowledgements

I would like to take advantage of the opportunity and thank all the people that supported me and make this work possible.

First, I want to thank Stephanie Reich for giving me the opportunity to work in her group in the field of SERS. It all started with a seminar about plasmonics. After writing my master thesis about one of the papers we heavily discussed in the seminar, I was very happy to stay for my PHD. Thank you for always have an open door to discuss problems, results, and new ideas. I enjoyed the time in your group very much.

Additionally I would like to thank...

... Martin Wolf for being my second supervisor. Thank you for taking the time and interest in my work.

... Georgy for being my office buddy and sharing the interest in Raman scattering and always helping me out with technical and scientific questions.

... Patryk for all the good talks we had. Thanks for introducing me to the different setups and discussing about crazy experiments we were thinking of.

... Sebastian for giving me insight in his work resulting in this thesis. Thanks for providing the samples and all the discussions about the topic. It was always a good time meeting you at conferences and in Berlin.

... Niclas for discussing the theoretical background of the work and sharing the interest in SERS.

... Timo and Elena for trusting me to supervise them over their thesis.

... the whole AG Reich for being a wonderful work group. I always enjoyed coming to work and have fun with you during a cake break or a barbecue.

... the Manchester crew Nick, Fredrik, Aravind, and Roman for providing gold nanostructures and graphene that started up my work in the field.

... Uwe for providing the nanostructures used in the work with nanotubes.

... Ben, Wenshan, and Ralph for providing the enriched CNTs and offering me the opportunity to visit the KIT and learn about the dielectrophoretic deposition.

... Etienne, Nathalie, and Richard for providing the filled nanotubes.

... Sabrina, Patryk, Georgy, Chris, and Simon for proofreading.

... my family for support throughout my whole studies and taking interest in the work I do.

... my wonderful girlfriend Sabrina for all the beautiful hours outside of work and having the patience with me while I wrote my thesis.

Publications

1. S. Wasserroth, S. Heeg, N. S. Mueller, P. Kusch, U. Hübner, E. Gaufrès, N. Y.-W. Tang, R. Martel, A. Vijayaraghavan, and S. Reich. Resonant, Plasmonic Raman Enhancement of α-6T Molecules Encapsulated in Carbon Nanotubes. *The Journal of Physical Chemistry C* **123**, 10578 (2019)

2. S. Wasserroth, T. Bisswanger, N. S. Mueller, P. Kusch, S. Heeg, N. Clark, F. Schedin, R. Gorbachev, and S. Reich. Graphene as a local probe to investigate near-field properties of plasmonic nanostructures. *Physical Review B* **97**, 155417 (2018)

3. N. S. Mueller, S. Heeg, M. P. Alvarez, P. Kusch, S. Wasserroth, N. Clark, F. Schedin, J. Parthenios, K. Papagelis, C. Galiotis, M. Kalbáč, A. Vijayaraghavan, U. Huebner, R. Gorbachev, O. Frank, and S. Reich. Evaluating arbitrary strain configurations and doping in graphene with Raman spectroscopy. *2D Materials* **5**, 015016 (2018)

4. L.Shi, P. Rohringer, M. Wanko, A. Rubio, S. Wasserroth, S. Reich, S. Cambré, W. Wenseleers, P. Ayala, and T. Pichler. Electronic band gaps of confined linear carbon chains ranging from polyyne to carbyne. *Physical Review Materials* **1**, 075601 (2017)

5. H. Li, G. Gordeev, S. Wasserroth, V. S. K. Chakravadhanula, S. K. C. Neelakandhan, F. Hennrich, A. Jorio, S. Reich, R. Krupke, and B. S. Flavel. Inner- and outer-wall sorting of double-walled carbon nanotubes. *Nature Nanotechnology* **12**, 1176–1182 (2017)

Bibliography

[1] C. V. Raman and K. S. Krishnan. A New Type of Secondary Radiation. *Nature*, **121**, 501 (1928).

[2] W. R. Fenner, H. A. Hyatt, J. M. Kellam, and S. P. S. Porto. Raman cross section of some simple gases. *Journal of the Optical Society of America*, **63**, 73 (1973).

[3] P. L. Stiles, J. A. Dieringer, N. C. Shah, and R. P. Van Duyne. Surface-Enhanced Raman Spectroscopy. *Annual Review of Analytical Chemistry*, **1**, 601–626 (2008).

[4] M. Cardona, R. K. Chang, G. Güntherodt, M. B. Long, and H. Vogt. *Light Scattering in Solids II*. Springer-Verlag Berlin Heidelberg (1982).

[5] A. D. McFarland, M. A. Young, J. A. Dieringer, and R. P. van Duyne. Wavelength-scanned surface-enhanced raman excitation spectroscopy. *The journal of physical chemistry. B*, **109**, 11279–11285 (2005).

[6] G. McNay, D. Eustace, W. E. Smith, K. Faulds, and D. Graham. Surface-enhanced raman scattering (sers) and surface-enhanced resonance raman scattering (serrs): a review of applications. *Applied spectroscopy*, **65**, 825–837 (2011).

[7] M. Fleischmann, P. J. Hendra, and A. J. McQuillan. Raman spectra of pyridine adsorbed at a silver electrode. *Chemical Physics Letters*, **26**, 163–166 (1974).

[8] D. L. Jeanmaire and R. P. Van Duyne. Surface raman spectroelectrochemistry. *Journal of Electroanalytical Chemistry and Interfacial Electrochemistry*, **84**, 1–20 (1977).

[9] C. L. Haynes, A. D. McFarland, and R. P. van Duyne. Surface-enhanced raman spectroscopy. *Analytical Chemistry*, **77**, 338 A–346 A (2005).

[10] G. Haran and L. Chuntonov. Artificial plasmonic molecules and their interaction with real molecules. *Chemical reviews*, **118**, 5539–5580 (2018).

[11] S.-Y. Ding, J. Yi, J.-F. Li, B. Ren, D.-Y. Wu, R. Panneerselvam, and Z.-Q. Tian. Nanostructure-based plasmon-enhanced raman spectroscopy for surface analysis of materials. *Nature Reviews Materials*, **1**, 942 (2016).

[12] E. C. Le Ru and P. G. Etchegoin. Single-Molecule Surface-Enhanced Raman Spectroscopy. *Annual Review of Physical Chemistry*, **63**, 65–87 (2012).

[13] H. Xu, J. Aizpurua, M. Käll, and P. Apell. Electromagnetic contributions to single-molecule sensitivity in surface-enhanced Raman scattering. *Physical Review E*, **62**, 4318–4324 (2000).

[14] S. L. Kleinman, E. Ringe, N. Valley, K. L. Wustholz, E. Phillips, K. A. Scheidt, G. C. Schatz, and R. P. Van Duyne. Single-Molecule Surface-Enhanced Raman Spectroscopy of Crystal Violet Isotopologues: Theory and Experiment. *Journal of the American Chemical Society*, **133**, 4115–4122 (2011).

[15] Q.-l. Li, B.-w. Li, and Y.-q. Wang. Surface-enhanced Raman scattering microfluidic sensor. *RSC Advances*, **3**, 13015–13026 (2013).

[16] E. Petryayeva and U. J. Krull. Localized surface plasmon resonance: Nanostructures, bioassays and biosensing - a review. *Analytica Chimica Acta*, **706**, 8–24 (2011).

[17] M. Moskovits. Persistent misconceptions regarding sers. *Physical chemistry chemical physics : PCCP*, **15**, 5301–5311 (2013).

[18] G. C. Schatz and R. P. Van Duyne. Electromagnetic Mechanism of Surface-Enhanced Spectroscopy. *Handbook of vibrational spectroscopy* (2002).

[19] G. C. Schatz, M. A. Young, and R. P. Van Duyne. Electromagnetic mechanism of SERS. *Surface-enhanced Raman scattering*. Springer (2006).

[20] E. Ru and P. Etchegoin. *Principles of Surface-Enhanced Raman Spectroscopy and Related Plasmonic Effects*. Elsevier Science (2008).

[21] N. S. Mueller, S. Heeg, and S. Reich. Surface-enhanced Raman scattering as a higher-order Raman process. *Physical Review A*, **94** (2016).

[22] P. Roelli, C. Galland, N. Piro, and T. J. Kippenberg. Molecular cavity optomechanics as a theory of plasmon-enhanced Raman scattering. *Nature Nanotechnology*, **11**, 164–169 (2015).

[23] R. Esteban, R. Vogelgesang, J. Dorfmüller, A. Dmitriev, C. Rockstuhl, C. Etrich, and K. Kern. Direct Near-Field Optical Imaging of Higher Order Plasmonic Resonances. *Nano Letters*, **8**, 3155–3159 (2008).

[24] R. Hillenbrand, F. Keilmann, P. Hanarp, D. S. Sutherland, and J. Aizpurua. Coherent imaging of nanoscale plasmon patterns with a carbon nanotube optical probe. *Applied Physics Letters*, **83**, 368–370 (2003).

[25] P. Kusch, S. Mastel, N. S. Mueller, N. Morquillas Azpiazu, S. Heeg, R. Gorbachev, F. Schedin, U. Hübner, J. I. Pascual, S. Reich, and R. Hillenbrand. Dual-Scattering Near-Field Microscope for Correlative Nanoimaging of SERS and Electromagnetic Hotspots. *Nano Letters*, **17**, 2667–2673 (2017).

[26] N. Mirsaleh-Kohan, V. Iberi, P. D. Simmons, N. W. Bigelow, A. Vaschillo, M. M. Rowland, M. D. Best, S. J. Pennycook, D. J. Masiello, B. S. Guiton, and J. P. Camden. Single-Molecule Surface-Enhanced Raman Scattering: Can STEM/EELS Image Electromagnetic Hot Spots? *The Journal of Physical Chemistry Letters*, **3**, 2303–2309 (2012).

[27] S. Heeg, R. Fernandez-Garcia, A. Oikonomou, F. Schedin, R. Narula, S. A. Maier, A. Vijayaraghavan, and S. Reich. Polarized Plasmonic Enhancement by Au Nanostructures Probed through Raman Scattering of Suspended Graphene. *Nano Letters*, **13**, 301–308 (2013).

[28] S. Heeg, A. Oikonomou, R. F. Garcia, S. A. Maier, A. Vijayaraghavan, and S. Reich. Strained graphene as a local probe for plasmon-enhanced raman scattering by gold nanostructures. *Physica Status Solidi-Rapid Research Letters*, **7**, 1067–1070 (2013).

[29] S. Wasserroth, T. Bisswanger, N. S. Mueller, P. Kusch, S. Heeg, N. Clark, F. Schedin, R. Gorbachev, and S. Reich. Graphene as a local probe to investigate near-field properties of plasmonic nanostructures. *Physical Review B*, **97**, 73 (2018).

[30] J. Maultzsch, H. Telg, S. Reich, and C. Thomsen. Radial breathing mode of single-walled carbon nanotubes: Optical transition energies and chiral-index assignment. *Physical Review B*, **72**, 4077 (2005).

[31] A. Vijayaraghavan, S. Blatt, D. Weissenberger, M. Oron-Carl, F. Hennrich, D. Gerthsen, H. Hahn, and R. Krupke. Ultra-large-scale directed assembly of single-walled carbon nanotube devices. *Nano letters*, **7**, 1556–1560 (2007).

[32] N. S. Mueller, S. Heeg, P. Kusch, E. Gaufrès, N. Y.-W. Tang, U. Hübner, R. Martel, A. Vijayaraghavan, and S. Reich. Plasmonic enhancement of sers measured on molecules in carbon nanotubes. *Faraday discussions*, **205**, 85–103 (2017).

[33] S. Maier. *Plasmonics: Fundamentals and Applications*. Springer US (2010).

[34] J. J. Mock, M. Barbic, D. R. Smith, D. A. Schultz, and S. Schultz. Shape effects in plasmon resonance of individual colloidal silver nanoparticles. *The Journal of Chemical Physics*, **116**, 6755 (2002).

[35] B. Sharma, R. R. Frontiera, A.-I. Henry, E. Ringe, and R. P. Van Duyne. SERS: materials, applications, and the future. *Materials today*, **15**, 16–25 (2012).

[36] P. K. Jain and M. A. El-Sayed. Plasmonic coupling in noble metal nanostructures. *Chemical Physics Letters*, **487**, 153 (2010).

[37] P. Klar, E. Lidorikis, A. Eckmann, I. A. Verzhbitskiy, A. C. Ferrari, and C. Casiraghi. Raman scattering efficiency of graphene. *Physical Review B*, **87** (2013).

[38] S. Wasserroth, S. Heeg, N. S. Mueller, P. Kusch, U. Hübner, E. Gaufrès, N. Y.-W. Tang, R. Martel, A. Vijayaraghavan, and S. Reich. Resonant, plasmonic raman enhancement of α-6t molecules encapsulated in carbon nanotubes. *The Journal of Physical Chemistry C*, **123**, 10578–10585 (2019).

[39] E. Gaufrès, N. Y.-W. Tang, F. Lapointe, J. Cabana, M.-A. Nadon, N. Cottenye, F. Raymond, T. Szkopek, and R. Martel. Giant raman scattering from j-aggregated dyes inside carbon nanotubes for multispectral imaging. *Nature Photonics*, **8**, 72–78 (2014).

[40] E. Gaufrès, N. Y.-W. Tang, A. Favron, C. Allard, F. Lapointe, V. Jourdain, S. Tahir, C.-N. Brosseau, R. Leonelli, and R. Martel. Aggregation control of a-sexithiophene via isothermal encapsulation inside single-walled carbon nanotubes. *ACS nano*, **10**, 10220–10226 (2016).

[41] J. S. Greer, G. I. Petrov, and V. V. Yakovlev. Raman spectroscopy with led excitation source. *Journal of Raman Spectroscopy*, **44**, 1058–1059 (2013).

[42] M. A. Schmidt and J. Kiefer. Polarization-resolved high-resolution raman spectroscopy with a light-emitting diode. *Journal of Raman Spectroscopy*, **44**, 1625–1627 (2013).

[43] N. Ashcroft and N. Mermin. *Solid State Physics*. HRW international editions. Holt, Rinehart and Winston (1976).

[44] J. D. Jackson. *Classical electrodynamics*. Wiley, New York, NY, 3rd ed. edn. (1999).

[45] P. Johnson and R. Christy. Optical Constants of the Noble Metals. *Physical Review B*, **6**, 4370 (1972).

[46] G. Mie. Beiträge zur optik trüber medien, speziell kolloidaler metallösungen. *Annalen der Physik*, **330**, 377 (1908).

[47] E. Prodan, C. Radloff, N. J. Halas, and P. Nordlander. A hybridization model for the plasmon response of complex nanostructures. *Science (New York, N.Y.)*, **302**, 419–422 (2003).

[48] J. B. Lassiter, J. Aizpurua, L. I. Hernandez, D. W. Brandl, I. Romero, S. Lal, J. H. Hafner, P. Nordlander, and N. J. Halas. Close Encounters between Two Nanoshells. *Nano Letters*, **8**, 1212 (2008).

[49] W. Rechberger, A. Hohenau, A. Leitner, J. R. Krenn, B. Lamprecht, and F. R. Aussenegg. Optical properties of two interacting gold nanoparticles. *Optics Communications*, **220**, 137–141 (2003).

[50] P. Yu and M. Cardona. *Fundamentals of Semiconductors: Physics and Materials Properties*. Graduate Texts in Physics. Springer Berlin Heidelberg (2010).

[51] A. C. Ferrari and D. M. Basko. Raman spectroscopy as a versatile tool for studying the properties of graphene. *Nature Nanotechnology*, **8**, 235 (2013).

[52] M. G. Albrecht and J. A. Creighton. Anomalously intense raman spectra of pyridine at a silver electrode. *Journal of the American Chemical Society*, **99**, 5215–5217 (1977).

[53] R. L. McCreery. *Raman spectroscopy for chemical analysis*, vol. v. 157 of *Chemical analysis*. John Wiley & Sons, New York (2000).

[54] A. Campion and P. Kambhampati. Surface-enhanced raman scattering. *Chemical Society Reviews*, **27**, 241 (1998).

[55] L. Jensen, C. M. Aikens, and G. C. Schatz. Electronic structure methods for studying surface-enhanced raman scattering. *Chemical Society Reviews*, **37**, 1061–1073 (2008).

[56] S. Morozov, K. Novoselov, M. Katsnelson, F. Schedin, D. Elias, J. Jaszczak, and A. Geim. Giant Intrinsic Carrier Mobilities in Graphene and Its Bilayer. *Physical Review Letters*, **100**, 016602 (2008).

[57] A. A. Balandin, S. Ghosh, W. Bao, I. Calizo, D. Teweldebrhan, F. Miao, and C. N. Lau. Superior Thermal Conductivity of Single-Layer Graphene. *Nano Letters*, **8**, 902 (2008).

[58] C. Lee, X. Wei, J. W. Kysar, and J. Hone. Measurement of the Elastic Properties and Intrinsic Strength of Monolayer Graphene. *Science*, **321**, 385–388 (2008).

[59] P. Avouris. Graphene: Electronic and Photonic Properties and Devices. *Nano Letters*, **10**, 4285–4294 (2010).

[60] F. Bonaccorso, Z. Sun, T. Hasan, and A. C. Ferrari. Graphene photonics and optoelectronics. *Nature Photonics*, **4**, 611–622 (2010).

[61] L. M. Malard, M. A. Pimenta, G. Dresselhaus, and M. S. Dresselhaus. Raman spectroscopy in graphene. *Physics Reports*, **473**, 51–87 (2009).

[62] F. Banhart, J. Kotakoski, and A. V. Krasheninnikov. Structural Defects in Graphene. *ACS Nano*, **5**, 26–41 (2011).

[63] D. Yoon, H. Moon, Y.-W. Son, J. S. Choi, B. H. Park, Y. H. Cha, Y. D. Kim, and H. Cheong. Interference effect on Raman spectrum of graphene on SiO2/Si. *Physical Review B*, **80**, 125422 (2009).

[64] M. Cardona and G. Güntherodt, eds. *Light Scattering in Solids II: Basic Concepts and Instrumentation*, vol. 50 of *Topics in Applied Physics*. Springer Berlin, Berlin, softcover reprint of the original 1st ed. 1982 edn. (2014).

[65] M. Huang, H. Yan, C. Chen, D. Song, T. F. Heinz, and J. Hone. Phonon softening and crystallographic orientation of strained graphene studied by raman spectroscopy. *Proceedings of the National Academy of Sciences of the United States of America*, **106**, 7304–7308 (2009).

[66] N. S. Mueller, S. Heeg, M. P. Alvarez, P. Kusch, S. Wasserroth, N. Clark, F. Schedin, J. Parthenios, K. Papagelis, C. Galiotis, M. Kalbac, A. Vijayaraghavan, U. Huebner, R. Gorbachev, O. Frank, and S. Reich. Evaluating arbitrary strain configurations and doping in graphene with Raman spectroscopy. *2D Materials*, **5** (2017).

[67] A. Das, S. Pisana, B. Chakraborty, S. Piscanec, S. K. Saha, U. V. Waghmare, K. S. Novoselov, H. Krishnamurthy, A. K. Geim, A. C. Ferrari, and A. K. Sood. Monitoring dopants by raman scattering in an electrochemically top-gated graphene transistor. *Nature Nanotechnology*, **3**, 210–215 (2008).

[68] J. E. Lee, G. Ahn, J. Shim, Y. S. Lee, and S. Ryu. Optical separation of mechanical strain from charge doping in graphene. *Nature communications*, **3**, 1024 (2012).

[69] S. Reich, C. Thomsen, and J. Maultzsch. *Carbon nanotubes: basic concepts and physical properties*. John Wiley & Sons (2008).

[70] P. Avouris, M. Freitag, and V. Perebeinos. Carbon-nanotube photonics and optoelectronics. *Nature Photonics*, **2**, 341 EP – (2008).

[71] J. S. Park, Y. Oyama, R. Saito, W. Izumida, J. Jiang, K. Sato, C. Fantini, A. Jorio, G. Dresselhaus, and M. S. Dresselhaus. Raman resonance window of single-wall carbon nanotubes. *Physical Review B*, **74**, 286 (2006).

[72] H. Kataura, Y. Kumazawa, Y. Maniwa, I. Umezu, S. Suzuki, Y. Ohtsuka, and Y. Achiba. Optical properties of single-wall carbon nanotubes. *Synthetic Metals*, **103**, 2555–2558 (1999).

[73] G. Gordeev. Elementary exciton mediated raman scattering mechanisms in pristine and functionalized single walled carbon nanotubes. Ph.D. thesis, Freie Universitaet Berlin (2019).

[74] G. S. Duesberg, I. Loa, M. Burghard, K. Syassen, and S. Roth. Polarized raman spectroscopy on isolated single-wall carbon nanotubes. *Physical review letters*, **85**, 5436–5439 (2000).

[75] M. Cardona and R. Merlin. *Light Scattering in Solid IX*, vol. 108 of *Topics in Applied Physics*. Springer-Verlag Berlin/Heidelberg, Berlin, Heidelberg (2007).

[76] P. M. Rafailov, C. Thomsen, K. Gartsman, I. Kaplan-Ashiri, and R. Tenne. Orientation dependence of the polarizability of an individual ws2 nanotube by resonant raman spectroscopy. *Japanese Journal of Applied Physics*, **72**, 107 (2005).

[77] L. Cognet, D. A. Tsyboulski, J.-D. R. Rocha, C. D. Doyle, J. M. Tour, and R. B. Weisman. Stepwise quenching of exciton fluorescence in carbon nanotubes by single-molecule reactions. *Science (New York, N.Y.)*, **316**, 1465–1468 (2007).

[78] A. Setaro, M. Adeli, M. Glaeske, D. Przyrembel, T. Bisswanger, G. Gordeev, F. Maschietto, A. Faghani, B. Paulus, M. Weinelt, R. Arenal, R. Haag, and S. Reich. Preserving π-conjugation in covalently functionalized carbon nanotubes for optoelectronic applications. *Nature communications*, **8**, 14281 EP – (2017).

[79] A. Hirsch. Functionalization of single-walled carbon nanotubes. *Angewandte Chemie International Edition*, **41**, 1853 (2002).

[80] B. W. Smith, M. Monthioux, and D. E. Luzzi. Carbon nanotube encapsulated fullerenes: a unique class of hybrid materials. *Chemical Physics Letters*, **315**, 31–36 (1999).

[81] M. A. Loi, J. Gao, F. Cordella, P. Blondeau, E. Menna, B. Bártová, C. Hébert, S. Lazar, G. A. Botton, M. Milko, and C. Ambrosch-Draxl. Encapsulation of conjugated oligomers in single-walled carbon nanotubes: towards nanohybrids for photonic devices. *Advanced materials*, **22**, 1635–1639 (2010).

[82] S. M. Bachilo, L. Balzano, J. E. Herrera, F. Pompeo, D. E. Resasco, and R. B. Weisman. Narrow (n,m)-distribution of single-walled carbon nanotubes grown using a solid supported catalyst. *Journal of the American Chemical Society*, **125**, 11186–11187 (2003).

[83] H. Wang, B. Wang, X.-Y. Quek, L. Wei, J. Zhao, L.-J. Li, M. B. Chan-Park, Y. Yang, and Y. Chen. Selective synthesis of (9,8) single walled carbon nanotubes on cobalt incorporated tud-1 catalysts. *Journal of the American Chemical Society*, **132**, 16747–16749 (2010).

[84] J. Liu, C. Wang, X. Tu, B. Liu, L. Chen, M. Zheng, and C. Zhou. Chirality-controlled synthesis of single-wall carbon nanotubes using vapour-phase epitaxy. *Nature communications*, **3**, 1199 EP – (2012).

[85] M. S. Arnold, S. I. Stupp, and M. C. Hersam. Enrichment of single-walled carbon nanotubes by diameter in density gradients. *Nano Letters*, **5**, 713–718 (2005).

[86] S. Ghosh, S. M. Bachilo, and R. B. Weisman. Advanced sorting of single-walled carbon nanotubes by nonlinear density-gradient ultracentrifugation. *Nature nanotechnology*, **5**, 443 EP – (2010).

[87] K. Moshammer, F. Hennrich, and M. M. Kappes. Selective suspension in aqueous sodium dodecyl sulfate according to electronic structure type allows simple

separation of metallic from semiconducting single-walled carbon nanotubes. *Nano Research*, **2**, 599–606 (2009).

[88] B. S. Flavel, M. M. Kappes, R. Krupke, and F. Hennrich. Separation of single-walled carbon nanotubes by 1-dodecanol-mediated size-exclusion chromatography. *ACS nano*, **7**, 3557–3564 (2013).

[89] B. S. Flavel, K. E. Moore, M. Pfohl, M. M. Kappes, and F. Hennrich. Separation of single-walled carbon nanotubes with a gel permeation chromatography system. *ACS nano*, **8**, 1817–1826 (2014).

[90] R. Krupke, F. Hennrich, H. B. Weber, M. M. Kappes, and H. v. Löhneysen. Simultaneous deposition of metallic bundles of single-walled carbon nanotubes using ac-dielectrophoresis. *Nano Letters*, **3**, 1019–1023 (2003).

[91] K. S. Novoselov, A. K. Geim, S. V. Morozov, D. Jiang, Y. Zhang, S. Dubonos, I. V. Grigorieva, and A. A. Firsov. Electric field effect in atomically thin carbon films. *Science*, **306**, 666–669 (2004).

[92] A. Reina, H. Son, L. Jiao, B. Fan, M. Dresselhaus, Z. Liu, and J. Kong. Transferring and identification of single- and few-layer graphene on arbitrary substrates. *J. Phys. Chem. C.*, **112**, 17741–17744 (2008).

[93] T. M. G. Mohiuddin, A. Lombardo, R. R. Nair, A. Bonetti, G. Savini, R. Jalil, N. Bonini, D. M. Basko, C. Galiotis, N. Marzari, K. S. Novoselov, A. K. Geim, and A. C. Ferrari. Uniaxial strain in graphene by Raman spectroscopy: G peak splitting, Grüneisen parameters, and sample orientation. *Physical Review B*, **79**, 205433 (2009).

[94] M. Lazzeri and F. Mauri. Nonadiabatic kohn anomaly in a doped graphene monolayer. *Phys. Rev. Lett.*, **97**, 266407 (2006).

[95] S. Huh, J. Park, K. S. Kim, B. H. Hong, and S. B. Kim. Selective n-Type Doping of Graphene by Photo-patterned Gold Nanoparticles. *ACS Nano*, **5**, 3639–3644 (2011).

[96] Z. Fang, Y. Wang, Z. Liu, A. Schlather, P. M. Ajayan, F. H. L. Koppens, P. Nordlander, and N. J. Halas. Plasmon-Induced Doping of Graphene. *ACS Nano*, **6**, 10222–10228 (2012).

[97] L. Novotny and B. Hecht. *Principles of Nano-Optics*. Cambridge University Press (2006).

[98] C. Thomsen and S. Reich. Double resonant raman scattering in graphite. *Phys. Rev. Lett.*, **85**, 5214 (2000).

[99] J. Zuloaga and P. Nordlander. On the Energy Shift between Near-Field and Far-Field Peak Intensities in Localized Plasmon Systems. *Nano Letters*, **11**, 1280–1283 (2011).

[100] K. L. Kelly, E. Coronado, L. L. Zhao, and G. C. Schatz. The optical properties of metal nanoparticles: The influence of size, shape, and dielectric environment. *The Journal of Physical Chemistry B*, **107**, 668–677 (2003).

[101] K. Ikeda, M. Takase, N. Hayazawa, S. Kawata, K. Murakoshi, and K. Uosaki. Plasmonically Nanoconfined Light Probing Invisible Phonon Modes in Defect-Free Graphene. *Journal of the American Chemical Society*, **135**, 11489–11492 (2013).

[102] F. Benz, M. K. Schmidt, A. Dreismann, R. Chikkaraddy, Y. Zhang, A. Demetriadou, C. Carnegie, H. Ohadi, B. d. Nijs, R. Esteban, J. Aizpurua, and J. J. Baumberg. Single-molecule optomechanics in picocavities. *Science*, **354**, 726–729 (2016).

[103] S. Heeg, N. Clark, A. Oikonomou, A. Vijayaraghavan, and S. Reich. Plasmon-enhanced raman scattering by suspended carbon nanotubes. *physica status solidi (RRL) - Rapid Research Letters*, **08**, 785–789 (2014).

[104] H. Kuzmany. The particle in the box model for resonance raman scattering in polyacetylene. *Pure and Applied Chemistry*, **57** (1985).

[105] K. Q. Le, A. Alù, and J. Bai. Multiple fano interferences in a plasmonic meta-molecule consisting of asymmetric metallic nanodimers. *Journal of Applied Physics*, **117**, 023118 (2015).

[106] H. Tang, C. Zhu, G. Meng, and N. Wu. Review—surface-enhanced raman scattering sensors for food safety and environmental monitoring. *Journal of The Electrochemical Society*, **165**, B3098–B3118 (2018).

[107] D. E. Gómez, Z. Q. Teo, M. Altissimo, T. J. Davis, S. Earl, and A. Roberts. The dark side of plasmonics. *Nano letters*, **13**, 3722–3728 (2013).